



UNIVERSITÉ PARIS-SUD

ÉCOLE DOCTORAL 517 : PARTICULES, NOYAUX ET COSMOS

Laboratoire de l'Accélérateur Linéaire (LAL)

Organisation Européenne pour la Recherche Nucléaire (CERN)

THÈSE DE DOCTORAT

Discipline : Physique

par

Oscar Roberto BLANCO GARCÍA

Dynamique du faisceau dans la section finale de focalisation du futur collisionneur linéaire

Date de soutenance : 03/07/2015

Composition du jury :

Directeur de thèse	Philip BAMBADE	Directeur de Recherche
Co-encadrant	Rogelio TOMÁS	Physicien au CERN
Examinateur	Achille STOCCHI	Professeur
Rapporteur	Jean-Marie DE CONTO	Professeur
Rapporteur	Nobuhiro TERUNUMA	Professeur Associé
Examinateur	Toshiaki TAUCHI	Professeur Associé



Thèse préparée au
Laboratoire de L'accélérateur Linéaire (LAL)
Le Centre Scientifique d'Orsay, Bâtiment 200 BP 34
91 898 Orsay CEDEX, France

financé par,



Centre National de la Recherche Scientifique (CNRS)
Organisation Européenne pour la Recherche Nucléaire (CERN)

Abstract

Oide and RAD ???

Including radiation effects during lattice design optimization is crucial in high energy accelerators. Oide effect and radiation in bending magnets are reviewed aiming to include them in the optical design process to minimize the IP beam size. The Oide double integral is expressed in simpler terms in order to speed up calculations, concluding in how longer quadrupoles with lower gradients may help reducing the Oide effect. Radiation in bending magnets is reviewed for linear lattices, generalizing to the case when the final dispersion is different from zero and making comparisons with theoretical results and particle tracking. An agreement between the theory, the implemented approximation included in MAPCLASS2 and the six-dimensional tracking in PLACET has been found. [english]

Keywords: Some keywords.

Abstract

Resume fr

Keywords: Some keywords.

Remerciements

I would like to thank my two directors Philip Bambade and Rogelio Tomas for their continuous encouragement to pursue the exploration of new ideas for linear colliders.

I would like also to thank the ATF staff, KNU and Oxford colleagues for their clear disposition and the exchange of ideas inside and outside the control room.

Finally, I would like to thank the LAL and CERN people I met or came across during the last three years. I've been always looking forward to exchange some words to do life simpler.

Contents

Introduction	17
Circular and linear colliders	18
I The Linear Colliders	21
1 Purpose of a linear collider	23
2 Linear Collider Concepts	25
2.1 Luminosity	25
2.2 Beam Delivery System (BDS)	25
2.3 Final Focus Sections (FFS)	25
2.4 Overview of FFS effects	26
2.4.1 Beamstrahlung	26
2.4.2 Hourglass effect	26
2.4.3 Crossing angle	26
2.4.4 Chromaticity	26
2.4.5 Tuning	28
3 Current Linear Collider Projects	29
3.1 International Linear Collider (ILC)	29
3.1.1 Beam Parameters	29
3.2 Compact Linear Collider (CLIC)	30
II Final focus design for small beam size	32
4 Chromaticity in the FFS	33
4.1 Chromaticity minimization in the Final Doublet (FD)	33
4.2 The non-interleaved lattice	38

4.2.1	Introduction	38
4.2.2	Geometric Terms Cancellation	38
4.2.3	The Lattice	39
4.2.4	Conclusion	41
5	Radiation in Bending Magnets	43
5.1	Theoretical approximation	43
5.1.1	Generalization of the optimization process	44
5.1.2	One dipole and one dipole with a drift	45
5.2	Comparison of theory and tracking results	45
5.3	Model limitations	48
5.4	Validity for the FFS	48
6	Oide effect	51
6.1	Beam size limit	51
6.2	Oide Double Integral Solution	52
6.3	Mitigating the impact on the beam size	53
6.3.1	QD0 length	53
6.3.2	Correctors	54
6.3.3	Conclusions	57
III	BPMs at the ATF2 Interaction Point (IPBPMs)	59
7	Relevance of ATF/ATF2	61
7.1	Facility purpose	61
7.2	Beam line Description	62
7.2.1	The RF Gun and Linac	63
7.2.2	The Damping Ring	63
7.2.3	The extraction line	63
7.2.4	The extraction diagnostic section	64
7.2.5	The ATF2 lattice	64
7.2.6	The IP Region	64
7.3	Beam Size Measurement at the IP	66
7.4	Beam stabilization	67
7.4.1	Tuning	67
7.4.2	Feedback	67

7.5	Recent achievements and current work	68
7.6	Position Measurement Requirements	68
8	BPMs System description	71
8.1	The system	71
8.1.1	The cavities	72
8.1.2	The processing electronics	75
8.1.3	Feedback system	77
8.1.4	The acquisition system	77
8.2	BPM Analysis Method	78
8.2.1	Waveform analysis	78
8.2.2	Position scans	78
8.2.3	Angle scans	79
8.2.4	Jitter acquisitions	79
9	System characterization and Preliminary Results	83
9.1	Calibration	83
9.1.1	Movers' Calibrations C_m	83
9.1.2	Cavity response calibration C_c	87
9.2	Dynamic Range	88
9.2.1	Acquisition System	88
9.2.2	Processing electronics and cavity sensitivity	88
9.3	Resolution	89
9.3.1	Acquisition System	89
9.3.2	Noise floor and cavity sensitivity	89
9.3.3	Resolution by trajectory reconstruction	90
9.4	Feedback	93
9.5	Present Status and Prospects	93
IV	Conclusions, Results and Perspectives	96
A	The primitive \mathcal{F}	99
B	IPBPMs Movers	103
B.1	System Description	103
B.1.1	The Piezo Movers	103

B.1.2	Electrical connections	104
B.1.3	The PLC	105
B.1.4	The PC	106
B.2	The BPMs	108
B.2.1	Coordinate system	108
B.2.2	Alignment adjustment	110
B.3	Alignment	110
B.3.1	Vacuum chamber	110
B.3.2	Effect of alignment on dynamic range	110
B.3.3	Effect of cavity alignment on calibration	111
B.3.4	Mechanical BPM alignment	112
Bibliography		114

List of Figures

1	The electromagnetic and electro-weak forces unify at the Terascale.	17
2.1	Chromaticity. Particles with off-momentum energy are focused at different longitudinal locations increasing the beam size.	26
2.2	Non-local chromaticity correction.	28
2.3	Local chromaticity correction.	28
3.1	CLIC non-local 3 TeV.	29
3.2	CLIC non-local 3 TeV.	30
4.1	FD with focal points IM and IP at different distances.	33
4.2	Normalized transversal functions (4.2a) β_{x1}/β_{x0} , (4.2b) β_{y1}/β_{y0} , (4.2c) Ξ_x , (4.2d) Ξ_y	35
4.3	CLIC 3TeV (4.3a) $\Xi(\beta_x^*/\beta_y^*, r, r_{im})$, (4.3b) β_{x1}/β_{y0} , (4.3c) β_{x1}/β_{y1}	36
4.4	CLIC 500GeV (4.3a) $\Xi(\beta_x^*/\beta_y^*, r, r_{im})$, (4.4b) β_{x1}/β_{y0} , (4.4c) β_{x1}/β_{y1}	37
4.5	Non-interleaved chromaticity correction.	38
4.6	Sextupoles joined by the transport matrix T_{12}	39
4.7	Phase advance in the non-interleaved lattice design.	39
4.8	Non-interleaved lattice design for CLIC 500 GeV. Dipoles in blue, horizontally focusing quadrupoles in red and above the axis, vertically focusing quadrupoles in red and below the axis, and sextupoles in black.	40
4.9	Beam size at the IP of the CLIC 500 GeV non-interleaved design as a function of transfer map order obtained with MAD-X PTC.	40
4.10	CLIC 500 GeV non-interleaved lattice. The second order dispersion from the T_{166} map component is not zero at the sextupole in the FD.	41
5.1	Beam size increase due to radiation normalized to closed expression assuming negligible energy loss. (Left) ‘Default’ radiation option, (Right) ‘Six_dim’ option in PLACET 0.99.01. Plots (a) and (b) correspond to $L = 10$ m for a dipole only. Plots (c) and (d) correspond to $\theta = 10^{-4}$ rad for a dipole only. Plots (e) and (f) correspond to $L = 10$ m and $\theta = 10^{-4}$ rad while varying the drift length. Beam energy is 1500 GeV in all cases.	47

5.2	Result from tracking, closed expression with the mean number of photons emitted by particle superimposed. Magnetic field is fixed at 5×10^{-3} T and $E = 1500$ GeV.	48
6.1	Design particle trajectory in blue and the trajectory of a particle due to radiation in the quadrupole in red.	51
6.2	Oide effect beam size contribution for CLIC 3 TeV design parameters. (a) σ_{oide}^2 normalized to designed linear beam size as a function of quad length for the minimum focusing k (when $\alpha_y = 0$ at the quadrupole opposite side to the IP), for k calculated as thin lens ($k = \frac{1}{Ll^*}$) and the current QD0. (b) k in the three previous cases for comparison.	54
6.3	Oide effect beam size contribution for CLIC 500 GeV design parameters. (a) σ_{oide}^2 normalized to designed linear beam size as a function of quad length for the minimum focusing k (when $\alpha_y = 0$ at the quadrupole opposite side to the IP), for k calculated as thin lens ($k = \frac{1}{Ll^*}$) and the current QD0. (b) k in the three previous cases for comparison.	54
6.4	CLIC 3 TeV beam at the IP after tracking through QD0 with and without radiation.	55
6.5	Correlation between the phase space coordinates $\Delta y, y'$ for CLIC 3 TeV from particle tracking and theoretical expression in Eq. (6.9).	55
6.6	For the nominal trajectory in blue, the kick in C1 must cancel the kick in C0. For all particles that radiate in red, the difference in kicks should cancel Δy	56
6.7	β functions and β_y/β_x ratio for CLIC 3 TeV FD, QF1 and QD0 in red on top. The dark area is occupied by QD0 and the IP is at $s = 0$	56
7.1	Diagrams containing the ATF composition and a zoom on the ATF2 section.	62
7.2	Optical functions in the Final Focus Section at ATF2. On top is the ATF2 lattice: dipoles in blue, quadrupoles in red and sextupoles in black.	65
7.3	Vertical and horizontal beam sizes for 1BY, 1000BY, and 0.5BY in the vertical plane, and 1BX, 10BX and 100BX in the horizontal plane.	66
7.4	IPBSM schematic design. The particle beams cross the interference pattern generated by a perpendicular laser beam. The number of electron-photon interactions varies with the fringe size and the particle beam size.	66
7.5	(Right) IPBSM laser path over the optical table perpendicular to the beam propagation. (Left) Beam size resolution for the angle modes : 2 \sim 8 $^\circ$ in green, 30 $^\circ$ in blue and 174 $^\circ$ in red.	67
8.2	Dipolar and monopolar mode in rectangular cavities.	72
8.3	Monopolar mode in cylindrical cavities.	72
8.4	Coupling to the dipole mode of the cavity.	73
8.5	Processing electronics per BPM per plane.	76
8.6	Limiter detector.	77
8.7	IQ rotation. The blue dots represent the systematic change in position.	78
9.1	Movers calibration test setup for the vertical plane.	84

9.2	Block AB movers, linearity test over four cycles.	85
9.3	Block AB movers minimum step and stability.	85
9.4	Horizontal to vertical coupling of movers motion.	85
9.5	Block C movers, linearity test over four cycles.	86
9.6	Stability at fixed voltage setting.	86
9.7	Horizontal to vertical movers coupling.	87
9.8	Calibrations as a function of attenuation.	87
9.9	Effect of attenuation in Q' signals from calibrations. Error bars are RMS.	88
9.10	IPBy Calibration versus charge normalized to the calibration at minimum charge.	89
9.11	Jitter measurement for the 3 BPMs.	90
9.12	Three BPM resolution. The position measurement at IPA and IPB are used to extrapolate to IPC. The residual from subtraction of the measured and extrapolated position at IPC is used to estimate the system resolution.	91
9.13	Correlation of the three BPMs measurements and predictions.	92
B.1	Piezo mover system connection diagram.	104
B.2	Control system per mover.	105
B.3	BPM coordinate system centered electrically. Beam in red, BPMs in green.	108
B.4	Reference system for the 3 BPMs.	109
B.5	Set of movers: M_{01234} in Block IPAB and M_{BCDE} in Block IPC.	109
B.6	Longitudinal position of the movers.	109
B.8	γ angle rotation over the BPM. The only effect on distance measured is to add γ to β .	112

List of Tables

1	Luminosity and beamstrahlung for the three current linear collider projects. LHC luminosity is added to compare the beam size and repetition rate from circular to linear colliders.	18
2	Approximative vertical chromaticity for the three current linear collider projects. LHC is added for comparison.	19
4.1	Approximative vertical chromaticity for the three current linear collider projects.	38
4.2	CLIC 500 GeV parameters used for the non-interleaved lattice design.	39
5.1	Bending angles in CLIC 3 TeV.	49
5.2	Bending angles in CLIC 500 GeV.	49
6.1	Vertical beam size and radiation beam size contribution for three lattices. ϵ_N is the normalized emittance, $\epsilon_N = \gamma\epsilon$	52
6.2	Effect of octupolar correctors on the beam size, total luminosity and peak luminosity.	57
7.1	Design parameters of ILC and ATF2 Final Focus. †The ILC lattice has two detector options: SiD and ILD.	61
7.2	Basic design parameters of the ATF injector linac.	63
7.3	ATF DR main parameters.	63
7.4	Vertical beam size at the cavities positions and the IP with the 1000BY optics.	69
7.5	Vertical beam size at the cavities positions and the IP with the 1BY optics.	69
8.1	Measured decay time for the three cavities before installation.	75
8.2	Resonant dipole frequency measurement at KEK before installation.	75
8.3	Jitter at beam waist with 1BX1BY optics.	80
8.4	Jitter at beam waist with 10BX1BY optics.	81
8.5	Jitter at IP with 1BX1BY optics.	81
8.6	Jitter at IPA with 10BX1BY optics.	81
9.1	Results from trajectory reconstruction.	93
9.2	IPBPMs status.	94

B.1	$M_{0123,BCDE} \in [-1, 1], \Delta M_{0123,BCDE} \geq 1.25 \times 10^{-2}$	110
B.2	Alignment measurement using $I' = 0$	111
B.3	Alignment measurement using $I' = 0$ and $Q' = 0$ for previous BPMs.	111
B.4	Position mechanical precision	112

Introduction

The triumph of the 20th century particle physics was the development of the Standard Model. Experiments determined the particle constituents of ordinary matter, and identified four forces binding matter and transforming it from one form to another. This success leads particle physicist to address even more fundamental questions, and explore deeper mysteries in science.

The Standard Model includes a third component beyond particles and forces, the Higgs mechanism. The Higgs mechanism permeates the universe, giving mass to the particles, and breaking the electro-weak force in two, the electromagnetic and the weak forces.

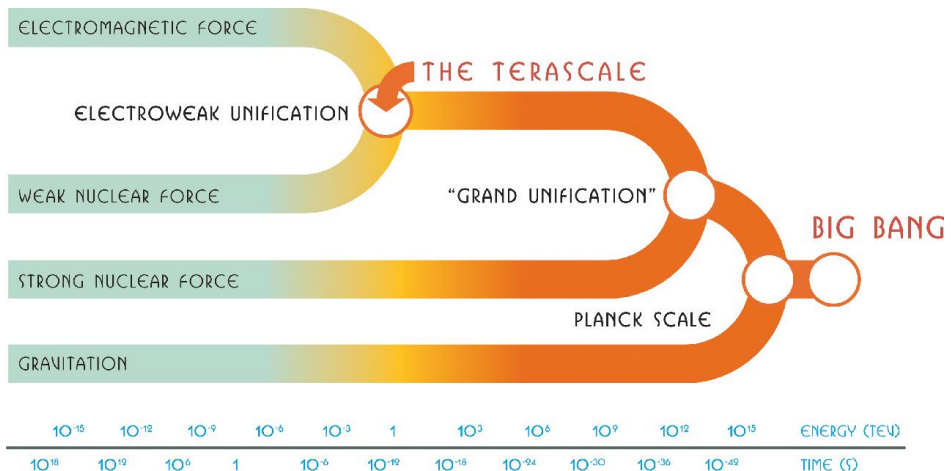


Figure 1 – The electromagnetic and electro-weak forces unify at the Terascale.

Experiments in the Terascale could test the idea that fundamental forces originate from a single unified force, see Fig. 1, and search for evidence of a related unified origin of matter involving supersymmetry. They could distinguish among patterns of phenomena to judge different unification models, providing a telescopic view of the ultimate unification.

There are two ways to explore the subatomic world, the first is to go to higher energy to discover new particles and measure their properties, the second is to increase the precision of the measurements to detect rare processes and make detailed studies.

The LHC allows the exploration of the electroweak symmetry breaking mechanism and other physical phenomena at the TeV scale, like the CP violation problem, the quark gluon plasma at the search of new physics beyond the Standard Model such as supersymmetry (SUSY) among others. The future linear collider beam energy will be determined by the LHC discoveries.

Higgs searches: The 4th of July of 2012, in a seminar held at CERN, the collaborations of the Experiments CMS and ATLAS presented an update of the Higgs of the Higgs searches status. At a confidence level of 4.9σ for CMS [1], and 5.1σ for ATLAS [2] from the Higgsless Standard Model, signals of a boson with a mass around $m_h = 125$ GeV were found with a strong spin-0

indication and coupling parameters consistent with the properties of the Standard Model Higgs Particle. First results on various rare production decay modes have been obtained but more data is needed to observe these models. Many analyses are ongoing and more updates are constantly presented.

Heavy Flavour and CP Violation: The experiments of the LHC, led by the LHCb, have carried out several important findings and measurements in the heavy flavour sector. New previously unobserved states have been observed for the very first time during the last years like the states X_b , Ξ_a and Λ_s^0 . Also the measurement of the quantum numbers of the states $X(3872)$ with $J^{PC} = 1^{++}$, have been determined to the 8σ level. The CP violation of the oscillation in D and B mesons have been measured to the 9.1σ confidence level discovering the same violation in B_s systems. The CP angle γ is known with a precision without precedents ($\gamma = (67 \pm 12)^\circ$). Finally, some very rare decays like $B_s \rightarrow \mu^+ \mu^-$, $B^0 \rightarrow K^* \mu^+ \mu^-$ and $D_s^+ \rightarrow \pi^+ \mu^+ \mu^-$ have been observed, with possible implications on the analysis of new physics.

Quark-gluon Plasma:

Circular and linear colliders

Higher energies have been usually explored with hadron colliders and the precision measurements has been done afterwards by lepton colliders. Lepton circular colliders are limited by the synchrotron radiation. Particles traversings magnetic fields will emmit photons and this photons make the beam loose energy per turn given by

$$\Delta E_{turn} = \frac{E^4}{3\rho m_0^4 c^8} \quad (1)$$

where m_0 is the rest mass of the particle, c is the speed of light, ρ is the curvature radius and E is the beam energy. The highest energy lepton collision, 209 GeV, have been reached with electron and positron coliding beams in LEP at CERN. In spite of the 27 km circumference of LEP the beam energy was limited by synchrotron radiation losses, just compensated by a powerfull superconducting RF system providing up to 3640 MV per revolution [3].

In the Final Focus the goal is to minimize the beam size to recover the luminosity L of a circular collider, limiting the energy loss due to beamstrahlung δ_{BS} . Equation 2 highlights the dependence with beam size in the tranversal planes.

$$L \propto \frac{f_{rep} n_b^2}{\sigma_x \sigma_y} \quad \delta_{BS} \propto \frac{n_b^2 E}{(\sigma_x + \sigma_y)^2} \quad (2)$$

Table (2) shows how the beam size is decreased in all linear collider projects to compensate lower repetition rate and charges. In addition, horizontal beam size is larger than vertical beam size to preserve luminosity while reducing the beam strahlung effect.

Parameter	Symbol	LHC	ILC	CLIC 500 GeV	CLIC 3 TeV
Energy/z (TeV)	E	7	0.250	0.250	1.500
Bunch population	n_b	1.15×10^{11}	2×10^{10}	6.8×10^9	3.72×10^9
Repetition rate [Hz]	f_{rep}	11.1×10^3	5	50	50
H/V. IP beam size [nm]	σ_x / σ_y	16.6×10^3	474/5.9	202/2.3	40/1
E loss (Beamstrahlung) [$\Delta E/E$]	δ_{BS}	-???	0.07	0.07	0.28
Luminosity	L	10^{34}	1.57×10^{34}	2.3×10^{34}	5.9×10^{34}

Table 1 – Luminosity and beamstrahlung for the three current linear collider projects. LHC luminosity is added to compare the beam size and repetition rate from circular to linear colliders.

Parameter	Symbol	LHC	ILC	CLIC 500 GeV	CLIC 3 TeV
Distance from IP to QD0 [m]	L^*	23	3.5/4.5	4.3	3.5
Vertical β at the IP [mm]	β_y^*	500	0.48	0.1	0.07
Energy Spread [10^{-3}]	δ	0.13	3	3	3
Vertical Chromaticity	$\xi_y \approx L^*/\beta^*$	46	7300/9400	43000	50000

Table 2 – Approximative vertical chromaticity for the three current linear collider projects. LHC is added for comparison.

Part I

The Linear Colliders

Chapter 1

Purpose of a linear collider

In order to achieve higher luminosity, it is necessary to reduce the beam size to compensate the lower frequency collisions in linear accelerators compared with storage and collider rings [4], and radiation effects should not be disregarded during the design stage of lattices.

Chapter 2

Linear Collider Concepts

2.1 Luminosity

Luminosity, L , is proportional to the number of collisions that are produced when two beams cross each other. The expression that relates luminosity, cross section σ and the number of events produced R is given by,

$$R = L\sigma \quad (2.1)$$

Luminosity will depend on the bunch population N (assuming an equal number of particles for both beams) and their density distribution within the bunches

2.2 Beam Delivery System (BDS)

After the acceleration, in the Beam Delivery System (BDS) the beam needs to be focused and higher order aberrations must be compensated to obtain nanometer beam size.

2.3 Final Focus Sections (FFS)

In the Final Focus Section (FFS) the goal is to minimize the beam size. If the lattice is conceived as a telescope where the matrix elements are as in Eq. (2.3), being M_x, M_y the magnifications in horizontal and vertical planes, then, beam size to the first order does not depends on the energy spread δ . Considering the second and third order components in the transfer map, as in Eq. (2.4), then, the telescope properties show that the main contribution to beam size is chromaticity ξ_y given by the elements T_{126} , and T_{346} [8], identified in [6] as

$$\xi_x = \frac{1}{\beta_x^*} \left(T_{116}^2 \beta_{x0} + T_{126}^2 \frac{1}{\beta_{x0}} \right) \quad \xi_y = \frac{1}{\beta_y^*} \left(T_{336}^2 \beta_{y0} + T_{346}^2 \frac{1}{\beta_{y0}} \right) \quad (2.2)$$

being the 0-index the values at the input and *-index the values at the output. For this reason, the FFS has been conceived as a telescope to demagnify the beam size with minimum effect of energy spread, where the main issue is the large chromaticity generated at the Final Doublet (FD), the last pair of quadrupoles which focus the beam at the Interaction Point (IP).

$$R = \begin{pmatrix} M_x & 0 & 0 & 0 \\ 0 & 1/M_x & 0 & 0 \\ 0 & 0 & M_y & 0 \\ 0 & 0 & 0 & 1/M_y \end{pmatrix} \quad (2.3)$$

$$x_i = \sum_{j=1}^6 R_{ij} x_j + \sum_{j,k=1}^6 T_{ijk} x_j x_k + \sum_{j,k,l=1}^6 U_{ijkl} x_j x_k x_l + \dots \quad x_i \in x, x', y, y', \tau, \delta \quad (2.4)$$

2.4 Overview of FFS effects

2.4.1 Beamstrahlung

2.4.2 Hourglass effect

Since the β -functions have their minimum at the IP and increase with the longitudinal distance, to consider the beam size constant along the whole collision length is some cases is not a good approximation. In a low- β region

2.4.3 Crossing angle

2.4.4 Chromaticity

As in the case of light beams through lenses, the longitudinal focal point location depends on the beam energy spread. This effect is called chromaticity. Figure 2.1 represents schematically the focusing effect of a magnet as a lens. A particle with the design momentum crossing the lens at a distance y_0 from the center will be focused at l^* . Off-momentum particles with higher or lower momentum will be under-focused or over-focused, respectively. This produces a variation in the transverse position at the focal distance l^* increasing the beam size.

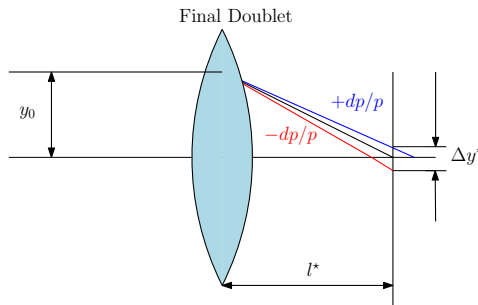


Figure 2.1 – Chromaticity. Particles with off-momentum energy are focused at different longitudinal locations increasing the beam size.

The effect on the beam size is commonly estimated as

$$\frac{\Delta y_{rms}^*}{\sigma_y^*} \approx \frac{l^*}{\beta^*} \sigma_\delta \approx \xi_y \sigma_\delta \quad (2.5)$$

where l^* is the focal length, σ_δ is the second moment of the energy spread distribution, β_y^* is the optical β function at the focal position and ξ_y is the chromaticity.

The chromatic dilution of the beam size can be expressed as

$$\sigma_y^* \approx \sigma_{y,0} \sqrt{1 + \xi_y^2 \sigma_\delta^2} \quad (2.6)$$

where $\sigma_{y,0}$ is the transverse beam size with zero energy spread.

Chromaticity correction

In the thin lens approximation with a vertically focusing quadrupole magnet of thickness ds , the kick in angle given to a crossing particle is expressed in [5] as

$$dx' = k_q(1 - \delta)xds \quad dy' = -k_q(1 - \delta)yds \quad (2.7)$$

where dx' , dy' are the horizontal and vertical angle kick respectively, k_q is the quadrupole gradient and $\delta = dP/P_0$ is the energy spread. A combination of bending magnets and sextupoles is used to subtract the extra kick due to energy spread.

First, horizontal position and energy are correlated by dispersion, η_x , generated by bending magnets [5]. This divides the particle motion in two parts: the betatron motion and an offset equal to $\eta_x\delta$. Equation (2.8) shows the coordinate transformation.

$$\begin{aligned} x &\rightarrow x_\beta + \eta_x\delta \\ y &\rightarrow y_\beta \end{aligned} \quad (2.8)$$

Then, sextupoles are located in dispersive regions ($\eta_x \neq 0$) to kick the particles cancelling the quadrupole angle kick dependence on δ . The quadrupole and sextupoles kicks in dispersive region are in Eq. (2.9), where k_s is sextupole gradient.

$$\begin{aligned} \text{Quadrupole: } dx' &= k_q(1 - \delta)(x_\beta + \eta_x\delta)ds & dy' &= -k_q(1 - \delta)y_\beta ds \\ \text{Sextupole: } dx' &= \frac{1}{2}k_s[(x_\beta + \eta_x\delta)^2 + y_\beta^2]ds & dy' &= -k_s(x_\beta + \eta_x\delta)y_\beta ds \end{aligned} \quad (2.9)$$

The chromatic terms, $k_qx_\beta\delta$ and $k_qy_\beta\delta$, are cancelled by matching k_q and $k_s\eta_x$.

The geometric terms introduced by the sextupole, $\frac{1}{2}k_s(x_\beta^2 + y_\beta^2)$ and $k_sx_\beta y_\beta$, are cancelled by another sextupole, both separated by a transport matrix equal to $-I$ transformation, being I the identity transport matrix.

The remaining terms are cancelled by a combination of bending magnets and sextupoles location and strengths. Two methods have been developed to achieve the cancellation all second order terms: the non-local correction and the local correction.

Non-local correction: The non-local correction scheme [10] compensates upstream the chromaticity in the FD. Figure 2.2 shows schematically the lattice configuration, where QF1 and QD0 constitute the FD, B0 to B5 are dipole magnets to produce horizontal dispersion, SD and SF sextupoles are used to cancel vertical and horizontal chromaticity respectively.

The chromatic terms, $k_qx_\beta\delta$ and $k_qy_\beta\delta$, are cancelled by making $k_q = k_s\eta_x$.

The term $k_q\eta_x\delta$ disappears because the final doublet is in a non-dispersive region.

The second order dispersion generated by the sextupoles, $\frac{1}{2}k_s\eta_x\delta^2$, is cancelled by matching the dispersion and sextupole strengths in the $-I$ transformation.

Local correction: The local chromaticity correction scheme [11] compensates chromaticity inside the FD and Fig. (2.3) shows the sextupoles locations.

The non-zero dispersion in the FD generates an offset on the quadrupole horizontal focusing center, $x = x_\beta + \eta_x\delta$.

The second order dispersion, $k_q\eta_x\delta^2$ and $\frac{1}{2}k_s\eta_x\delta^2$, is half cancelled if $k_q = k_s\eta_x$. One solution is to double the sextupole strength and produce the entire chromaticity upstream in a non-dispersive region.

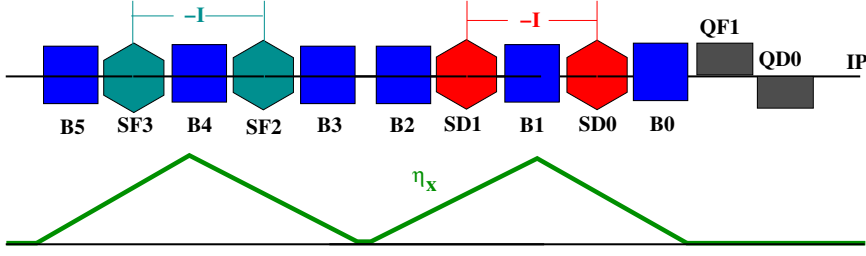


Figure 2.2 – Non-local chromaticity correction.

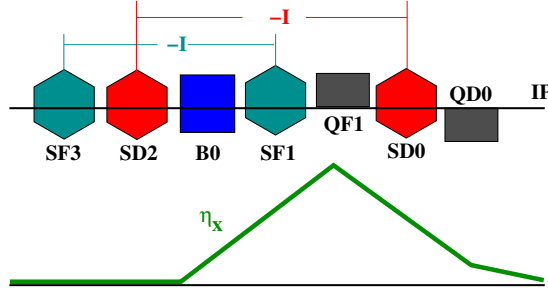


Figure 2.3 – Local chromaticity correction.

2.4.5 Tuning

When considering imperfections, the machine performance decreases dramatically, typically, the beam size increases and luminosity drops substantially about 6 orders of magnitude. The tuning is the procedure which brings the system performance to its design values. Since the initial errors are unknown, the tuning requires a statistical study. Usually more than 100 machines with randomly distributed errors are considered in computer simulations. The simulated tuning reproduces a realistic tuning procedure in a machine [6, 7].

Chapter 3

Current Linear Collider Projects

3.1 International Linear Collider (ILC)

The ILC is designed to have a continuous center-of-mass energy range between 200 MeV and 500 GeV, and peak luminosity $L = 2 \times 10^{34} \text{ cm}^{-2}\text{s}^{-1}$, consistent with producing 500 fb^{-1} in the first four years of operation. In addition, the machine should be upgradable to a center-of-mass of 1 TeV. It has been designed to achieve and energy stability and precision of 0.1 %, and to have 80% electron polarization at the IP as well as an option for 60% positron polarization. Furthermore, alternative options for $\gamma\gamma$ and e^-e^- collisions are under consideration.

3.1.1 Beam Parameters

The nominal ILC beam Parameters set has been chosen to optimize between known accelerator physics and technology challenges throughout the whole accelerator complex, as beam instability and kicker hardware constraints in the Damping Ring (DR), beam current, beam power and pulse length limitations in the main linac, emittance preservation, and acceptable levels of background and kink instability issues at the IP. The ILC has been designed such that each subsystem accommodates a range of beam parameters, resulting in flexible operating parameters that will allow identified problems in one area to be compensated for in another. For example

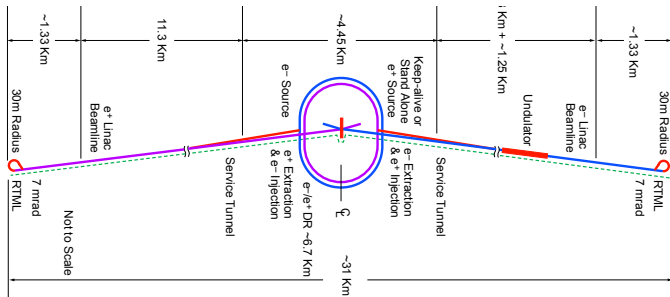


Figure 3.1 – CLIC non-local 3 TeV.

3.2 Compact Linear Collider (CLIC)

The first chapter...???

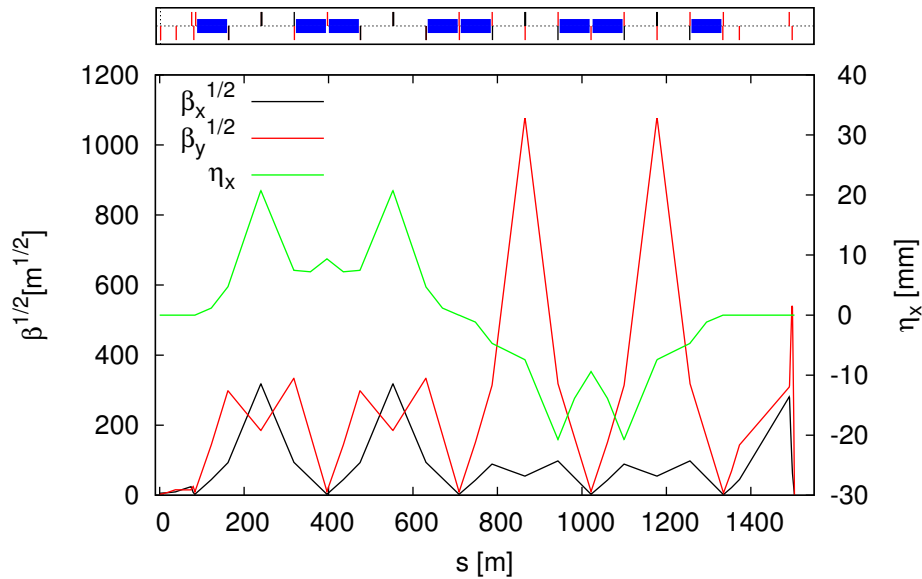


Figure 3.2 – CLIC non-local 3 TeV.

Part II

Final focus design for small beam size

Chapter 4

Chromaticity in the FFS

4.1 Chromaticity minimization in the Final Doublet (FD)

In this Section I find the Final Doublet distance that minimizes the chromaticity.

In the thin lens approximation, an FD as in Fig. 4.1, with $r = L/L_{IP}$ and $r_{im} = L_{IM}/L_{IP}$, has peak β -functions at the quadrupoles equal to $\beta_{y0} = \frac{L_{IP}^2}{\beta_x^*}$ for QD0 and

$\beta_{y1} = \beta_{x0} \left(1 + r \pm \sqrt{\frac{r}{r_{im}} + r + \frac{r^2}{r_{im}}} \sqrt{\frac{1+r}{1+r/r_{im}}} \right)^2$ for QF1, using $\left(\frac{\beta^*}{L_{IP}}\right)^2 \ll 1$, i.e. a small β function far from QD0. The factor β_{y1}/β_{x0} is the beta function at QF1 relative to QD0.

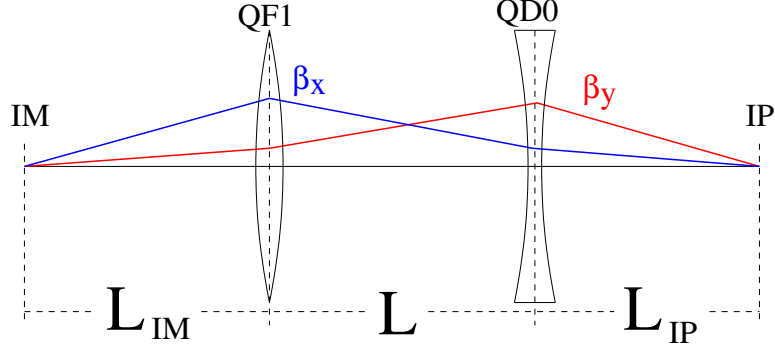


Figure 4.1 – FD with focal points IM and IP at different distances.

Being the chromaticity for a single quadrupole as in Eq. (4.1) from [6],

$$\xi_y^x = \int \beta_y^x(s) k(s) ds \quad (4.1)$$

where the k is the quadrupole gradient and s the longitudinal coordinate, then, ξ_y^x can be evaluated as

$$\xi_y^x = \mp \left(\beta_{y1} k_1 l_1 - \beta_{y0} k_0 l_0 \right) = \frac{L_{IP}}{\beta_x^*} \Xi_y^x(r, r_{im}) \quad (4.2)$$

where k, l are the quadrupole gradient and length, β^* is the β function at the IP, the indexes indicate the quadrupole and

$$\Xi_y^x(r, r_{im}) = \mp \sqrt{\frac{1}{rr_{im}} + \frac{1}{r} + \frac{1}{r_{im}}} \sqrt{\frac{1+r/r_{im}}{1+r}} \left[\left(1 + r \pm \sqrt{\frac{r}{r_{im}} + r + \frac{r^2}{r_{im}}} \sqrt{\frac{1+r}{1+r/r_{im}}} \right)^2 - \left(\frac{1+r}{1+r/r_{im}} \right) \right] \quad (4.3)$$

Figure 4.2 show the chromaticity Ξ_x and Ξ_y in L_{IP}/β^* units, and the ratio of the β functions at the quadrupoles.

In order to minimize the product of dispersion and sextupole strengths used to subtract the quadrupoles chromatic effect, explained in Section 2.4.4, one possibility is to minimize the sum of the horizontal and vertical chromaticities, i.e. the total chromaticity to be corrected. Being the sum,

$$\xi = \xi_x + \xi_y = \frac{L_{IP}}{\beta_y^*} \left(\frac{\Xi_x(r, r_{im})}{\beta_x^*/\beta_y^*} + \Xi_y(r, r_{im}) \right) \quad (4.4)$$

$$= \frac{L_{IP}}{\beta_y^*} \Xi(\beta_x^*/\beta_y^*, r, r_{im}) \quad (4.5)$$

Figure 4.3 shows Ξ for CLIC 3 TeV, $\beta_x^*/\beta_y^* = 6.9\text{mm}/0.068\text{mm} = 101$, and Fig 4.4 is the equivalent for CLIC 500 GeV [9], $\beta_x^*/\beta_y^* = 8.0\text{mm}/0.1\text{mm} = 80$.

Given L_{IM} , the minimum added chromaticity in the FD is found when L is one to two times the distance to the IP. In addition, Figs. 4.3-4.4 show the effect of scaling up the system. For example, starting at $L = L_{IP}$ and $L_{IM} = 10L_{IP}$, it is clear that a system with $L = 10L_{IP}$ and $L_{IM} = 100L_{IP}$, will decrease the vertical chromaticity by increasing the horizontal chromaticity.

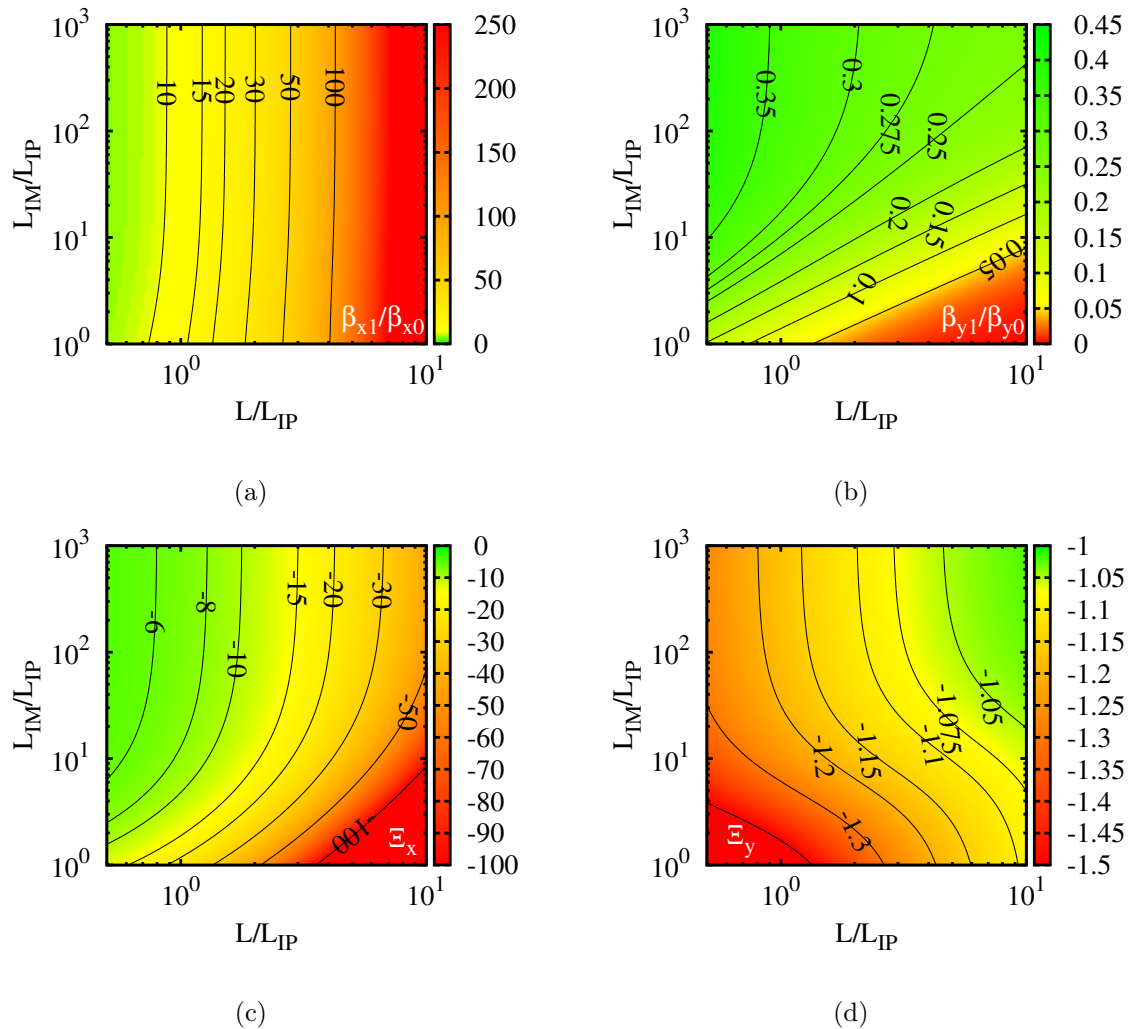


Figure 4.2 – Normalized transversal functions (4.2a) β_{x1}/β_{x0} , (4.2b) β_{y1}/β_{y0} , (4.2c) Ξ_x , (4.2d) Ξ_y

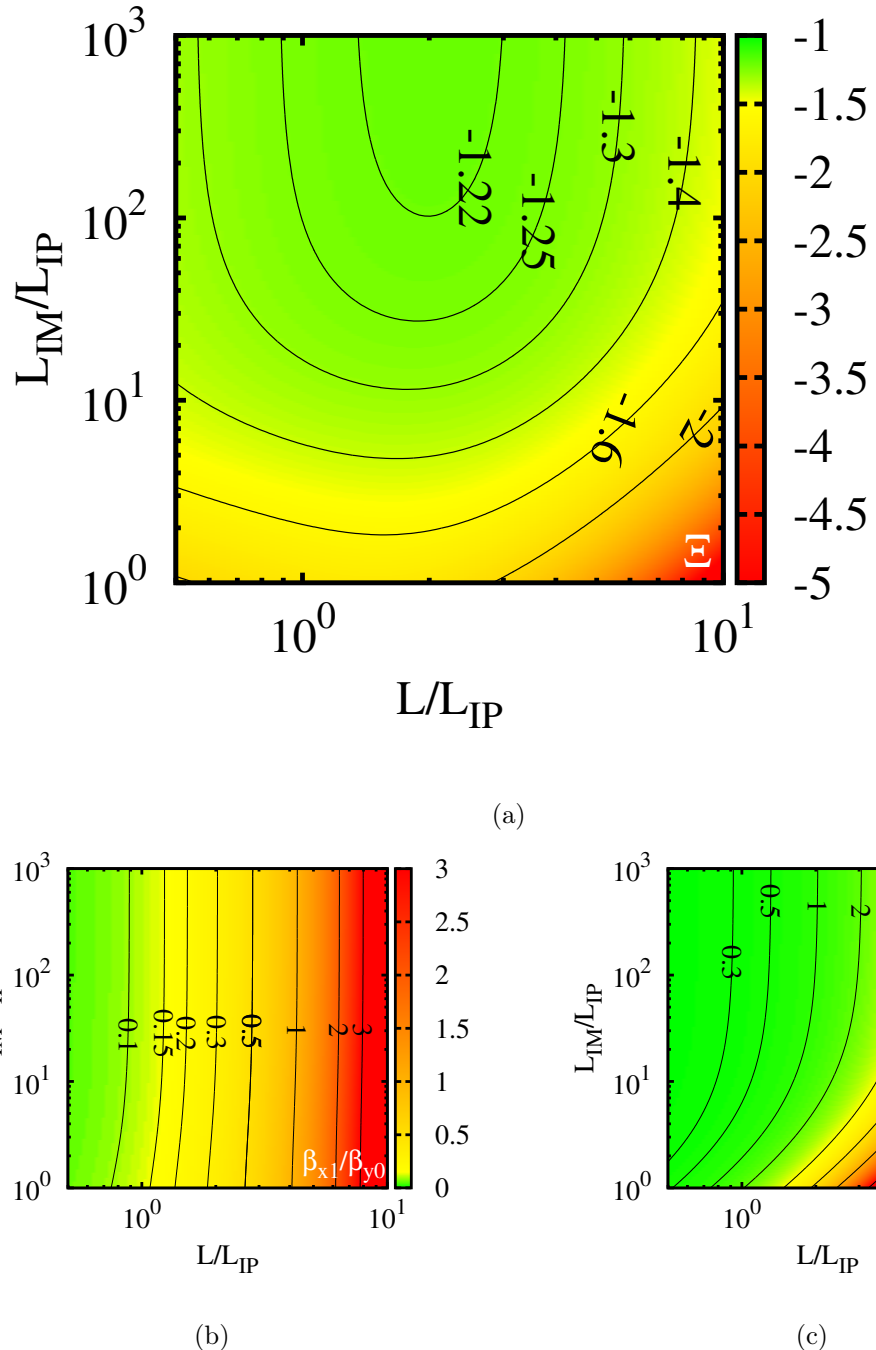


Figure 4.3 – CLIC 3TeV (4.3a) $\Xi(\beta_x^*/\beta_y^*, r, r_{im})$, (4.3b) β_{x1}/β_{y0} , (4.3c) β_{x1}/β_{y1}

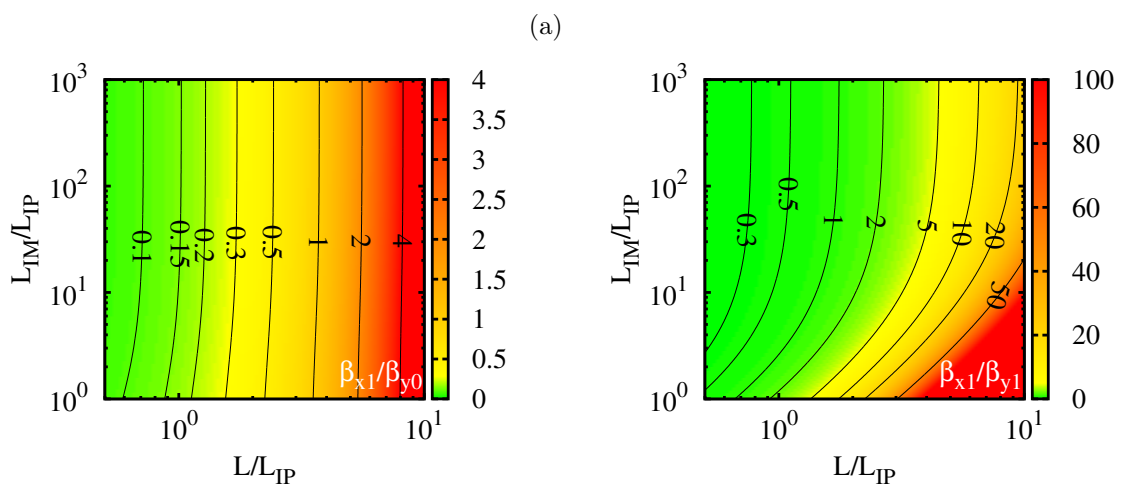
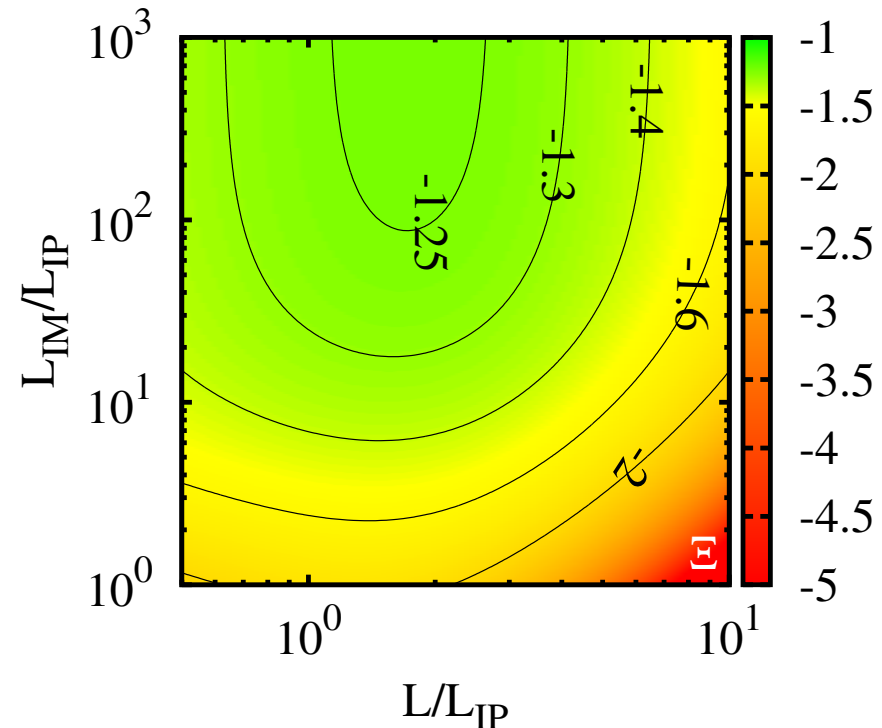


Figure 4.4 – CLIC 500GeV (4.3a) $\Xi(\beta_x^*/\beta_y^*, r, r_{im})$, (4.4b) β_{x1}/β_{y0} , (4.4c) β_{x1}/β_{y1}

4.2 The non-interleaved lattice

4.2.1 Introduction

Large chromaticity is generated in linear colliders due to the ratio of long L^* and low- β^* values. Table 4.1 shows the chromaticity in the current three main linear collider projects.

Parameter	Symbol	ILC	CLIC 500 GeV	CLIC 3 TeV
Distance from IP to QD0 [m]	L^*	3.5/4.5	4.3	3.5
Vertical β at the IP [mm]	β_y^*	0.48	0.1	0.07
Energy Spread [10^{-3}]	δ	3	3	3
Vertical Chromaticity	$\xi_y \approx L^*/\beta_y^*$	7300/9400	43000	50000

Table 4.1 – Approximative vertical chromaticity for the three current linear collider projects.

Two methods have been used to cancel the chromatic effect: non-local and local correction. The local and non-local schemes, presented in Section 2.4.4, have been compared for CLIC [12], concluding in easier tuning capabilities for the non-local. It has been mainly attributed to the separation of the horizontal and vertical chromatic correction sections, while in the local, the horizontal and vertical correction sections are interleaved.

This Section introduces an alternative lattice. In the non-interleaved scheme, the idea is to preserve the separation in the vertical and horizontal chromatic corrections while cancelling the geometrical components in the vertical plane at the FD. One of the paired sextupoles is inside a horizontally dispersive region while the other remains outside to cancel geometric contributions.

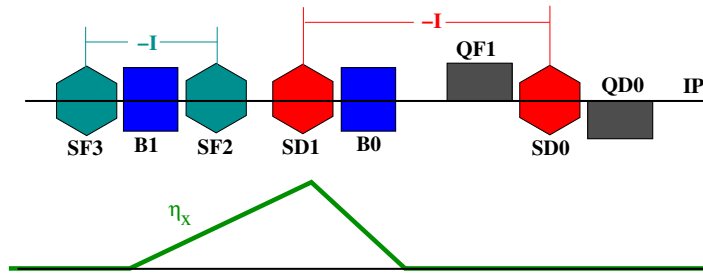


Figure 4.5 – Non-interleaved chromaticity correction.

Horizontal dispersion is generated over a common region and it is cancelled upstream, before the FD. Figure 4.5 shows QD0 preceded by a sextupole SD0, which is matched with a second SD1 by the -I transport map. The same configuration is used to cancel horizontal chromaticity in an upstream section of the lattice using SF sextupoles.

4.2.2 Geometric Terms Cancellation

Previously mentioned chromatic correction schemes use a pair of matched sextupoles to cancel one another geometrical components. It is generally noted as the -I transformation. However, results from [13] show that the -I transformation is one particular solution. When having a pair of sextupoles as in Fig. 4.6 joined by a transport matrix T_{12} , the general solution is $t_{12} = 0$, $t_{34} = 0$, $t_{11}t_{22} = 1$, $t_{33}t_{44} = 1$, $k_{s1} = -k_{s2}t_{11}$ and $t_{11} = \pm t_{33}$, where, t_{ij} are the matrix elements and k_{s1}, k_{s2} are the sextupole gradients. This general solution is used here to give more flexibility to the beta functions in the design. Fig. (4.7) shows the relative phase

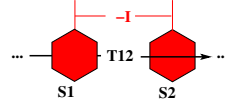


Figure 4.6 – Sextupoles joined by the transport matrix T_{12} .

advances required in the non-interleaved design.

Those expressions from the linear transport map set restrictions on the optic lattice parameters and tolerances during the lattice design stage. In order to evaluate those tolerances, $\Delta\phi_x, \Delta\phi_y, r_x, r_y$ have been defined as $\phi_{x12} + \Delta\phi_x = \pi$, $\phi_{y12} + \Delta\phi_y = \pi$, $k_{s1}\beta_{x1}^{3/2} - k_{s2}\beta_{x2}^{3/2} + r_x = 0$ and $k_{s1}\beta_{y1}^{3/2} - k_{s2}\beta_{y2}^{3/2} + r_y = 0$ respectively, where $\Delta\phi$ is the phase advance error, r is the residual after subtractions and ϕ, β are the optical parameters in horizontal x and vertical y planes for both sextupoles $S1$ or $S2$.

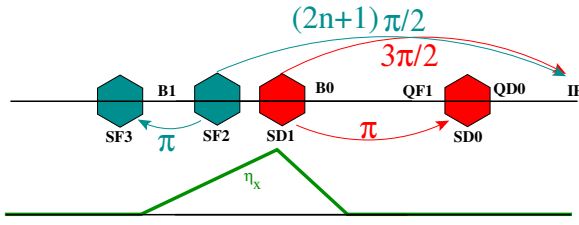


Figure 4.7 – Phase advance in the non-interleaved lattice design.

Factors $\alpha_{x1}\Delta\phi_x, \alpha_{x2}\Delta\phi_x, \alpha_{y1}\Delta\phi_y, \alpha_{y2}\Delta\phi_y \ll 1$, with α the optic parameter, are conditions to achieve geometrical terms cancellation. The FD requires phase advances finely matched because α and β are high, and the residuals r_x, r_y should be close to zero in order to cancel the second order map components in both planes at the same time. The β_y/β_x ratio can be chosen to match sextupole strengths.

4.2.3 The Lattice

Using the CLIC 500 GeV parameters listed in 4.2, new lattices were designed in MAD-X [14] following the previous considerations and those in [15]. Fig. (4.8) is an example. Phase advances have been matched to 10^{-6} precision due to high α values in the FD. MAPCLASS2 [16, 17, 18, 19] gives vertical beam size of 1.9nm and horizontal beam size of 186nm to the first order.

Parameter [Units]	Value
Maximum energy/beam [TeV]	0.25
Distance from IP to first quad, L^* [m]	4.3
Nominal core beam size at IP, $\sigma^*, x/y$ [nm]	202/2.3
Nominal beta-function at IP, $\beta^*, x/y$ [mm]	8/0.1

Table 4.2 – CLIC 500 GeV parameters used for the non-interleaved lattice design.

However, Fig. (4.9) shows that the horizontal beam size increases slightly to second order and by more than an order of magnitude when third order components in the map are considered.

The reason to this beam size growth is the second order dispersion (T_{166}) in the sextupole inside the FD, see Fig. (4.10). As opposed to the local chromaticity method were T_{166} is cancelled only at the IP by matching the sextupoles and dispersion function, here, the second order dispersion generates higher order components due to the sextupole inside the FD used

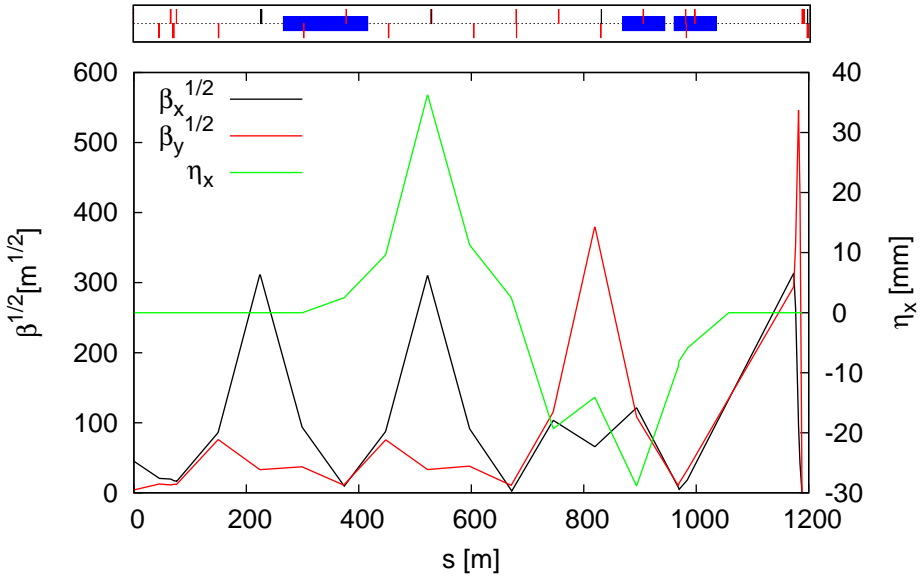


Figure 4.8 – Non-interleaved lattice design for CLIC 500 GeV. Dipoles in blue, horizontally focusing quadrupoles in red and above the axis, vertically focusing quadrupoles in red and below the axis, and sextupoles in black.

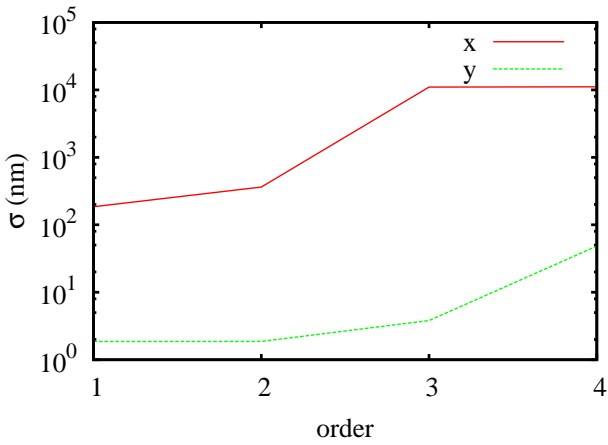


Figure 4.9 – Beam size at the IP of the CLIC 500 GeV non-interleaved design as a function of transfer map order obtained with MAD-X PTC.

for geometrical cancellation. This is not present in the non-local method because there is no sextupole in the FD.

Two possible solutions are foreseen at the moment : cancel the map components T_{166} and T_{266} before the FD, or alternatively tolerate some dispersion in the FD to cancel the second order

map and making it similar to the local method.

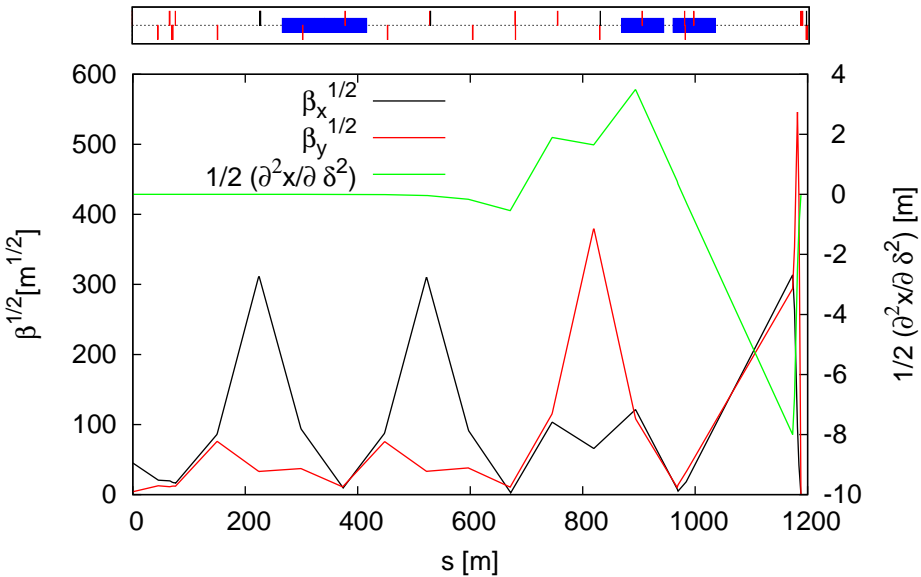


Figure 4.10 – CLIC 500 GeV non-interleaved lattice. The second order dispersion from the T_{166} map component is not zero at the sextupole in the FD.

4.2.4 Conclusion

The non-interleaved lattice proposal has been conceived as an alternative to the local and non-local chromaticity correction methods. The added horizontal and vertical chromaticity has been minimized by using a distance from QD0 to QF1 approximately one and two times the distance between QD0 and the IP. Also, a general geometrical cancellation has been used to give more flexibility to the linear lattice design, however the large beta functions close to the FD impose high precision in the phase advance between sextupole elements.

The non-interleaved design for CLIC 500 GeV has been diagnosed using MAD-X and MAPCLASS2, concluding that the second order dispersion must be cancelled before the FD because of the high gradient sextupole before QD0 used to cancel geometrical components only.

Two solutions are foreseen : the cancellation of the second order dispersion and its derivative before the FD, or alternatively generate dispersion in the FD to cancel the residual second and third order components making it similar to the local correction.

Cancellation could be achieved by introducing an additional horizontal focal point upstream with no dispersion and no sextupole, this will increase the amount of total horizontal chromaticity, thereby changing the SF2 and SF3 sextupole strengths without changing the quads in the dispersive region, and enabling perhaps a better cancellation of T_{166} generated by the quad and sextupole in the dispersive part.

Chapter 5

Radiation in Bending Magnets

Considering radiation effects is crucial during the design stage of an accelerator, where effects can be evaluated by tracking particles through the lattice or by analytical approximations. However, during the design process this effect is evaluated iteratively after lattice optic parameters are set. In order to include both, radiation and optic parameters, during the design optimization process, radiation in bending magnets is reviewed in this chapter.

The theory developed by Sands in [20] is first presented in order to clarify all terms used in the beam size contribution from the radiation model. The analytical result in [20] is generalized to the case with non-zero alpha at the IP and non-zero dispersion, required during the desing and luminosity optimization process. The closed solution for one dipole and one dipole with a drift is compared with the tracking code PLACET [21] and finally the model validity for the FFS design is analyzed.

5.1 Theoretical approximation

Assuming a lattice that can be described by transport matrices in the form written in the Eq. (5.1), radiation effects can be calculated by the model in [20].

$$\begin{pmatrix} x_2 \\ x'_2 \\ \delta \end{pmatrix} = \begin{pmatrix} C(s_1, s_2) & S(s_1, s_2) & R_{16}(s_1, s_2) \\ C'(s_1, s_2) & S'(s_1, s_2) & R_{26}(s_1, s_2) \\ 0 & 0 & 1 \end{pmatrix} \begin{pmatrix} x_1 \\ x'_1 \\ \delta \end{pmatrix} \quad (5.1)$$

Being $\Delta x_i = R_{16}(s_i, s_p)(-u)/E$, the deviation at the observation point s_p due to the i^{th} photon of energy u radiated at some point s_i , and E the beam energy.

The rhs term in Eq. (5.2) is the sum of Δx_i over the N photons radiated during the time T for the particle to cross the magnet. $N(T)$ describes the probability distribution of photon emission. As we are interested only in the second order moment, the mean $x_0 = \langle \sum_{i=1}^{N(T)} \Delta x_i \rangle$ is subtracted from the sum, obtaining $\langle x \rangle = 0$, $\sigma_{\text{bend}}^2 = \langle x^2 \rangle$, being x the horizontal transverse displacement from the reference orbit of a particle at the observation point.

$$\sum_{i=1}^{N(T)} \Delta x_i - x_0 = x \quad (5.2)$$

The photon emission follows a Poisson distribution as a consequence of the normalized radiation spectrum and photon number spectrum of synchrotron radiation used in [22] (Section 5). For any Poisson-like distribution $\sigma_N^2 = \langle N \rangle$. The beam size contribution due to

radiation has two components of variability: the spread of Δx_i due to the energy emission u and the number of times the emission process occurs N^1 . Calculations are shown in Eqs. (5.3),

$$\begin{aligned}\sigma_{bend}^2 &= \langle x^2 \rangle - \langle x \rangle^2 = \langle x^2 \rangle \\ &= \langle N \rangle \sigma_{\Delta x}^2 + \langle \Delta x \rangle^2 \sigma_N^2 \\ &= \langle N \rangle \langle (\Delta x)^2 \rangle - \langle N \rangle \langle \Delta x \rangle^2 + \langle \Delta x \rangle^2 \langle N \rangle \\ &= \langle N \rangle \langle (\Delta x)^2 \rangle\end{aligned}\quad (5.3)$$

where the i sub-index has been removed intentionally because the photon number emission is extracted from a continuous function of u , the photon energy and either T or s/c , where c is the speed of light.

The rate of emission of photons is calculated as in Eq. (5.4) where $K_{5/3}$ is the modified Bessel function, $u_c = \frac{3}{2} \frac{\hbar c \gamma^3}{\rho}$ called the critical energy which depends on the relativistic factor γ , the reduced Planck constant \hbar and the particle trajectory curvature ρ , and $P_\gamma = \frac{2c r_e m^2}{3\rho^2} \gamma^4$ is the instantaneous radiated power where r_e is the classical electron radius and m is the electron mass.

$$n(u, s) = \frac{P_\gamma}{u_c^2} \left[\frac{9\sqrt{3}}{8\pi} \int_{u/u_c}^\infty K_{5/3}(\xi) d\xi \right] \quad (5.4)$$

Using $\Delta x(s) = (-u/E)R_{16}(s, s_p)$ the second moment is calculated by integration over the entire space and energies.

$$\sigma_{bend}^2 = \int_0^T \int_0^\infty [\Delta x(u, s)]^2 n(u, s) du dt \quad (5.5)$$

$$= \frac{1}{c} \int_0^{s_p} \int_0^\infty \left[\frac{-u}{E} R_{16}(s, s_p) \right]^2 n(u, s) du ds \quad (5.6)$$

Finally,

$$\sigma_{bend}^2 = C_2 \int_0^{s_p} \frac{E^5}{\rho^3} R_{16}(s, s_p)^2 ds \quad (5.7)$$

where $C_2 = \frac{55}{24\sqrt{3}} \frac{r_e \hbar c}{(mc^2)^6} = 4.13 \times 10^{-11} \text{ m}^2 \text{GeV}^{-5}$ is a constant coming from the emission rate integration already derived by Sands.

5.1.1 Generalization of the optimization process

During the optimization process it is convenient to rewrite R_{16} using the off-momentum function η , lattice parameters and Eq. (5.1). Measuring from the reference orbit, the kick propagation from s to s_p can be written in terms of the general transport matrix, giving

$$\Delta x(s)_{total} = \frac{-u}{E} \eta(s_p) = \frac{-u}{E} [C(s, s_p) \eta(s) + S(s, s_p) \eta'(s) + R_{16}(s, s_p)] \quad (5.8)$$

$$\eta(s_p) = \sqrt{\frac{\beta_{s_p}}{\beta_s}} [\eta_s \cos \Delta\phi_{s,s_p} + (\alpha_s \eta_s + \beta_s \eta'_s) \sin \Delta\phi_{s,s_p}] + R_{16}(s, s_p) \quad (5.9)$$

where α, β and ϕ are the optics parameters and the subscripts indicate the evaluation point. The equations derived by Sands in [20] assume $\alpha_{s_p} = 0, \eta_{s_p} = 0$ and $\eta'_{s_p} = 0$, which are not

¹Using statistics notation, $\sigma_x = V(x)$ and $\langle x \rangle = E(x)$, then, a process with two components of variability has a variance expressed as $V(x) = E(V(x|N)) + V(E(x|N))$. The term $(x|N)$ denotes the evaluation of the x variable for a given N

valid during the lattice optimization process or when the waist shift is used to get more luminosity in ILC and CLIC [23].

From Eq. (5.7) and (5.9) the contribution to beam size due to radiation now can be calculated as:

$$\sigma_{bend}^2 = C_2 \int_0^{s_p} \frac{E_s^5}{\rho_s^3} \left\{ \sqrt{\frac{\beta_{s_p}}{\beta_s}} [\eta_s \cos \Delta\phi_{s,s_p} + (\alpha_s \eta_s + \beta_s \eta'_s) \sin \Delta\phi_{s,s_p}] - \eta_{s_p} \right\}^2 ds \quad (5.10)$$

Eq. (5.10) was included in MapClass2 in order to be used during lattice design and luminosity optimization. It is also worth noting that $\eta_{s_p} = 0$ agrees with the result obtained by Sands in the ideal case with zero dispersion at the IP. This generalized expression I obtained is solved for the simple case of one bending magnet and compared with tracking results.

5.1.2 One dipole and one dipole with a drift

An analytical closed expression has been derived for two cases: one sector magnet (ρ, L, θ), and a sector magnet plus a drift (L_{drift}). Beam energy loss is negligible compared with beam energy E .

For a sector magnet, $R_{16} = \rho(1 - \cos \theta)$, the radiation effect is calculated as follows

$$\sigma_{bend}^2 = C_2 E^5 \int_0^\theta \frac{1}{\rho^3} [\rho(1 - \cos(\theta - \chi))]^2 \rho d\chi \quad (5.11)$$

$$= C_2 E^5 \left[\frac{1}{4} (6\theta - 8 \sin \theta + \sin(2\theta)) \right] \quad (5.12)$$

$$= C_2 E^5 \left(\frac{\theta^5}{20} - \frac{\theta^7}{168} + \frac{\theta^9}{2880} - \frac{17\theta^{11}}{1330560} + O(\theta^{13}) \right) \quad (5.13)$$

In the case of a drift after the bending magnet and defining $j = \frac{L_{drift}}{\rho} = \frac{L_{drift}}{L} \theta$

$$\sigma_{bend}^2 = C_2 \int_0^\theta E^5 \left[1 - \cos(\theta - \xi) + \frac{L_{drift}}{\rho} \sin(\theta - \xi) \right]^2 d\xi \quad (5.14)$$

$$= \frac{C_2}{4} E^5 [(1 - j^2) \sin(2\theta) - 8 \sin \theta + 4j(1 - \cos \theta)^2 + (6 - 2j^2)\theta] \quad (5.15)$$

$$= C_2 E^5 \left[\frac{j^2 \theta^3}{3} + \frac{j \theta^4}{4} - \frac{(4j^2 - 3)\theta^5}{60} - \frac{j \theta^6}{24} + \frac{(16j^2 - 15)\theta^7}{2520} + \frac{j \theta^8}{320} \right. \\ \left. - \frac{(64j^2 - 63)\theta^9}{181440} - \frac{17j \theta^{10}}{120960} + \frac{(256j^2 - 255)\theta^{11}}{19958400} + \frac{31j \theta^{12}}{7257600} \right. \\ \left. - \frac{(1024j^2 - 1023)\theta^{13}}{3113510400} + O(\theta^{14}) \right] \quad (5.16)$$

Eqs. (5.12) and (5.15) will be used to normalize the results from MAPCLASS2 and PLACET [21] where some care should be taken due to numerical precision.

5.2 Comparison of theory and tracking results

The closed expression in Section 5.1.2 is now compared with the general expression included in MAPCLASS2, Eq. (5.10), and the tracking code PLACET in the case of one dipole and one dipole and a drift. This is shown in Fig. (5.1), normalized to the close expressions in Eqs.

(5.12) and (5.15), where radiation effect in PLACET was obtained by subtracting the squared beam size from two trackings with same input parameters except for radiation ON/OFF.

Figures (5.1) (a) and (b) show the effect of systematic change of θ while keeping ρ and L . Figures (5.1) (c) and (d) show the effect of changing L while keeping ρ and θ . Figures (5.1) (e) and (f) show the effect of changing L_{drift} while keeping the magnet constant. The equivalent magnetic field B is calculated using the magnetic rigidity $B\rho = P/e$ for $E = 1.5$ TeV.

When observing the PLACET results in Fig. 5.1, the left plots show agreement of (80~90)% between the closed expression and the tracking, while the right side shows perfect agreement in almost all cases. The difference is the tracking method used by PLACET.

In PLACET 0.99.01 two different implementations of radiation exist: the first is the ‘default’ and the second one will be called ‘six_dim’. ‘Default’ calculates radiation by segmenting the dipole in a *default* number of shorter pieces with Binomial probability of photon emission when the particle traverses each slide. This is called thin dipole approximation and it is also the default tracking method. On the other side, ‘six_dim’ does not make any sectioning of the dipole, it uses the Poisson probability of photon emission over the entire dipole, as in the theory.

In order to confirm, the authors of PLACET provided several variations of the code where the number of slices was increased, making the Binomial probability to approach the Poisson distribution. In the light of the results presented on this thesis, since PLACET 0.99.02 ‘six_dim’ is the default tracking method.

As expected, the MAPCLASS2 and the closed expression are in good agreement, showing the validity of the generalization in Section 5.1.1. There is a point to highlight in Fig. (5.1) (b). The tracking, theoretical and general calculations are all in good agreement in the range of angles between 10^{-2} and 10^{-5} rad. Below 10^{-5} rad the agreement again decays to (80~90)%. This is related to the average number of photons emitted when traversing the dipole and it is explored in Section 5.3.

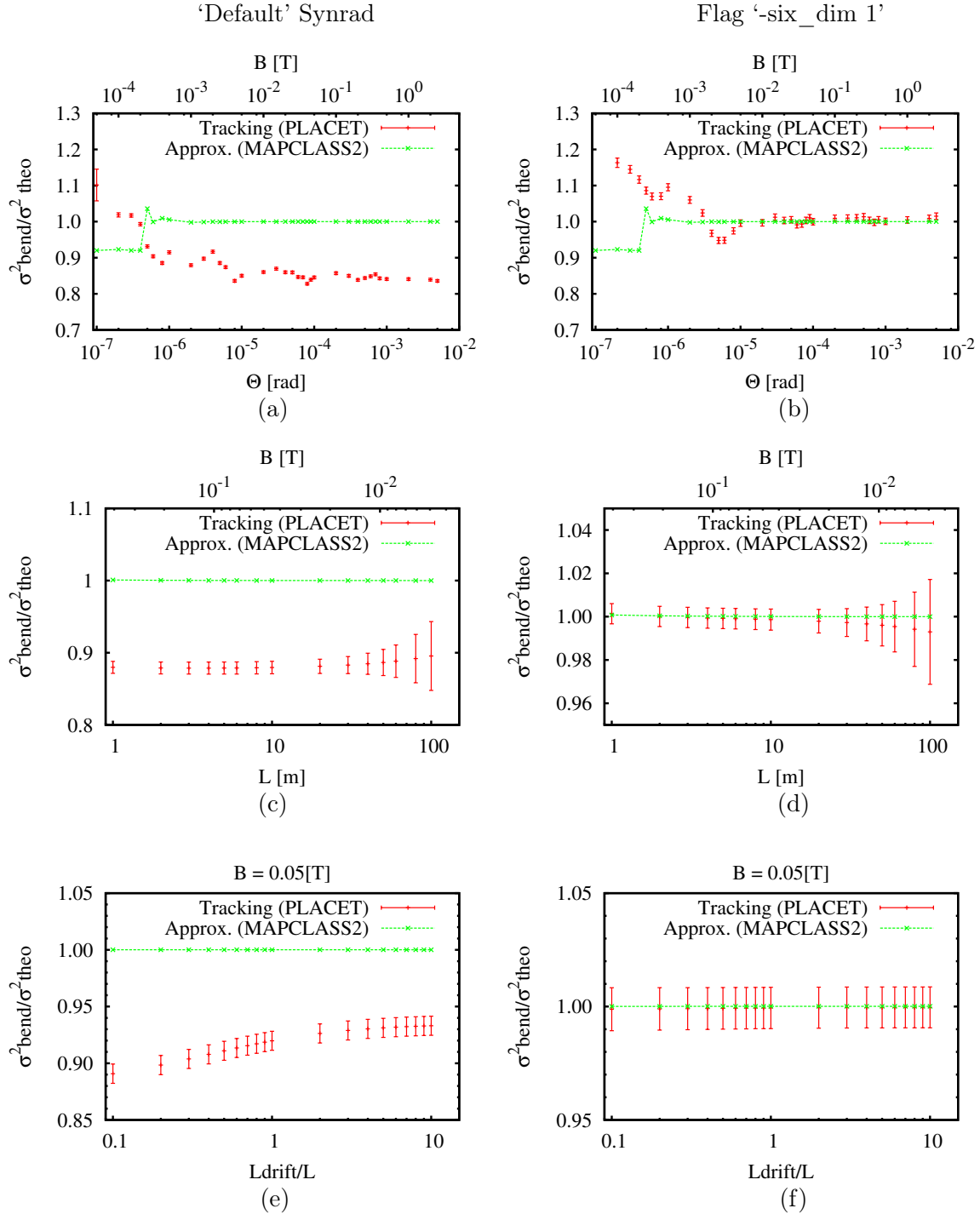


Figure 5.1 – Beam size increase due to radiation normalized to closed expression assuming negligible energy loss. (Left) ‘Default’ radiation option, (Right) ‘Six_dim’ option in PLACET 0.99.01. Plots (a) and (b) correspond to $L = 10$ m for a dipole only. Plots (c) and (d) correspond to $\theta = 10^{-4}$ rad for a dipole only. Plots (e) and (f) correspond to $L = 10$ m and $\theta = 10^{-4}$ rad while varying the drift length. Beam energy is 1500 GeV in all cases.

5.3 Model limitations

The radiation model is valid when the average number of photons radiated per particle $\langle N \rangle$ is enough to characterize the overall effect in position by its second moment, where $\langle N \rangle = C_1 E \theta$ with $C_1 = 20.61 \text{ GeV}^{-1}$.

Although, Section 5.2 explores the variation of θ , this also implies a change in the magnetic field strength B . In this Section the magnetic field is fixed $5 \times 10^{-3} \text{ T}$ and the magnet length L is systematically shortened to reduce the average number of photons emitted by each particle, changing θ because $B\rho$ is fixed for $E = 1500 \text{ GeV}$.

Figure (5.2) shows how the average number of photons emitted decreases with the dipole length L . It is visible also that the region where the average is below one photon is also the starting point when tracking and theory start to differ, reaching $\pm 10\%$ max.

This result is equivalent to the thin dipole approximation mentioned in Section 5.2, where the dipole sectioning makes of each slice a binomial trial of photon emission, approaching the Poisson theoretical distribution for large number of slices.

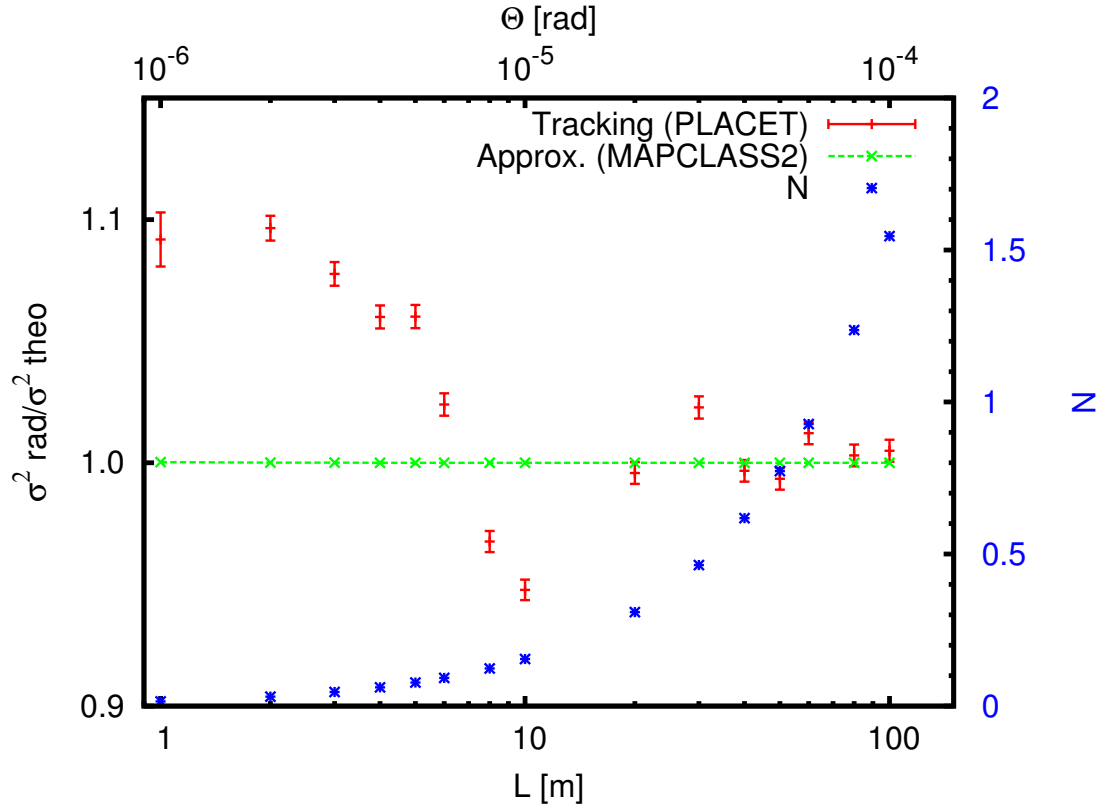


Figure 5.2 – Result from tracking, closed expression with the mean number of photons emitted by particle superimposed. Magnetic field is fixed at $5 \times 10^{-3} \text{ T}$ and $E = 1500 \text{ GeV}$.

5.4 Validity for the FFS

The CLIC FFS design is composed by magnets with bending angles shown in Table 5.1 for 3 TeV and Table 5.2 for 500 GeV. The third column indicates the number of magnets used in each of those sections.

Although the average value of photons emitted per magnet is low, these are grouped in long

sections with common bending angle. Using the conclusions from Sect. 5.3 it will be similar to

$ \theta $ (μrad)	$\langle N \rangle$	Qty.
1.1	0.07	70
3.9	0.24	20
17.2	1.06	10

$ \theta $ (μrad)	$\langle N \rangle$	Qty.
8.3	0.08	70
27.5	0.28	20
135.0	1.39	10

Table 5.2 – Bending angles in CLIC 500 GeV.

Table 5.1 – Bending angles in CLIC 3 TeV.

the thin dipole approximation and the tracking coded should be within $\pm 10\%$ agreement with the theoretical contribution from radiation in bending magnets.

Chapter 6

Oide effect

This part of the document addresses the radiation phenomenon in quadrupoles called Oide effect[24], which sets a limit on the beam size demagnification, specially important in linear colliders because of the strong focusing required in the Final Doublet before the Interaction Point (IP).

First, a brief introduction to the beam size limit (Oide limit) is given, where calculations have been derived to include this radiation phenomenon in the lattice design and optimization software. The Oide effect is evaluated for the CLIC 3 TeV and CLIC 500 GeV parameters, leading to change the length of the first quadrupole before the IP, called QD0. It ends with a proposal to mitigate the impact of the Oide effect by adding correctors before and after the QD0, reducing the beam size.

6.1 Beam size limit

The Oide effect is caused by the interaction of charged particles with the magnetic field from quadrupoles. Radiation in a focusing magnet, schematically represented as QD0 in Fig. (6.1), changes the energy of the particle and modifies the focusing effect. This results in a limit on the minimum beam size specially relevant in the vertical plane.

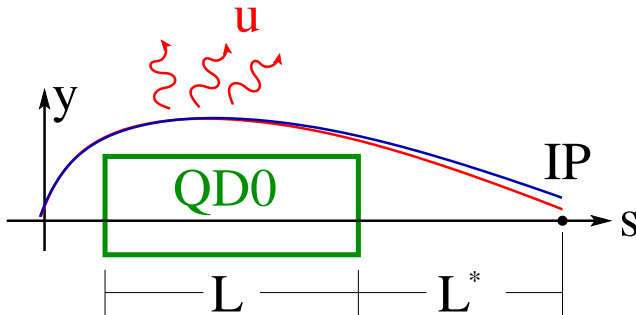


Figure 6.1 – Design particle trajectory in blue and the trajectory of a particle due to radiation in the quadrupole in red.

The beam size growth due to radiation is added quadratically to the linear beam size $\sigma_0^2 = \epsilon\beta$ where β represents the optical beta function and ϵ is the emittance. Therefore, $\sigma^2 = \sigma_0^2 + \sigma_{oide}^2$, where the beam size contribution from the Oide effect is [24],

$$\sigma_{oide}^2 = \frac{110}{3\sqrt{6\pi}} r_e \frac{\lambda_e}{2\pi} \gamma^5 F(\sqrt{k}L, \sqrt{k}L^*) \left(\frac{\epsilon}{\beta^*} \right)^{5/2} \quad (6.1)$$

where

$$F(\sqrt{k}L, \sqrt{k}L^*) = \int_0^{\sqrt{k}L} |\sin \phi + \sqrt{k}L^* \cos \phi|^3 \left[\int_0^\phi (\sin \phi' + \sqrt{k}L^* \cos \phi')^2 d\phi' \right]^2 d\phi \quad (6.2)$$

and λ_e is the Compton wavelength of the electron, r_e is the classical electron radius, γ is the relativistic factor, ϵ is the geometrical beam emittance, β^* is the Twiss parameter at the observation point (in this case, the IP), and k , L and L^* are the quadrupole gradient, the quadrupole length and the distance to the observation point measured from the closest magnet face.

Although the total contribution to beam size depends on the lattice and beam parameters, the minimum achievable beam size is given by [24]

$$\sigma_y \min = \left(\frac{7}{5} \right)^{\frac{1}{2}} \left[\frac{275}{3\sqrt{6}\pi} r_e \frac{\lambda_e}{2\pi} F(\sqrt{K}L, \sqrt{K}L^*) \right]^{\frac{1}{7}} (\epsilon_N)^{\frac{5}{7}} \quad (6.3)$$

where $\epsilon_N = \gamma\epsilon$ is the normalized emittance, showing the independence from beam energy.

The only possibility to reduce the beam size is by changing the value of F , by modifying the magnet parameters, or to minimize the beam emittance. However, using the ILC 500 GeV [25], CLIC 500 GeV and CLIC 3 TeV [9] parameters, it is possible to conclude from columns σ_0 and σ_{oide} in Table (6.1) that the contribution of the Oide effect to beam size is only significant for CLIC 3 TeV.

In addition, columns σ and σ_{min} in Table (6.1) show that both CLIC designs are close to the minimum achievable beam size.

Lattice	ϵ_N (nm)	γ (10^3)	σ_0 (nm)	k (m^{-2})	L (m)	L^* (m)	F	σ_{oide} (nm)	σ (nm)	σ_{min} (nm)
CLIC 3 TeV	20	2935.0	0.70	0.116	2.73	3.5	4.086	0.85	1.10	1.00
CLIC 500 GeV	25	489.2	2.3	0.077	3.35	4.3	4.115	0.08	2.3	1.17
ILC 500 GeV	40	489.2	5.7	0.170	2.20	4.3	9.567	0.04	5.7	1.85

Table 6.1 – Vertical beam size and radiation beam size contribution for three lattices. ϵ_N is the normalized emittance, $\epsilon_N = \gamma\epsilon$.

6.2 Oide Double Integral Solution

In this section the double integral used to calculate F is solved with the goal to increase the computational calculation speed. It was included in MapClass2[16, 17, 18, 19] to be used in lattice design and optimization.

The inner integral over ϕ' can be solved because it has a known primitive.

$$\int_0^\phi (\sin \phi' + \sqrt{k}l^* \cos \phi')^2 d\phi' = \frac{\phi}{2} [(\sqrt{k}l^*)^2 + 1] + \frac{\sin(2\phi)}{4} [(\sqrt{k}l^*)^2 - 1] + \sqrt{k}l^* \sin^2 \phi \quad (6.4)$$

The Eq. (6.2) can now be expressed as one integral.

$$F(\sqrt{k}L, \sqrt{k}l^*) = \int_0^{\sqrt{k}L} |\sin \phi + \sqrt{k}l^* \cos \phi|^3 \left(\frac{\phi}{2} [(\sqrt{k}l^*)^2 + 1] + \frac{\sin(2\phi)}{4} [(\sqrt{k}l^*)^2 - 1] + \sqrt{k}l^* \sin^2 \phi \right)^2 d\phi \quad (6.5)$$

The squared factor in brackets is always positive because all inner terms are real. The term inside the absolute value is also always positive, therefore, the integrand is always positive.

Now, considering the function:

$$|\sin \phi + \sqrt{k}l^* \cos \phi| = \begin{cases} \sin \phi + \sqrt{k}l^* \cos \phi, & \text{if, } \sin \phi + \sqrt{k}l^* \cos \phi \geq 0 \\ -(\sin \phi + \sqrt{k}l^* \cos \phi), & \text{if, } \sin \phi + \sqrt{k}l^* \cos \phi < 0 \end{cases} \quad (6.6)$$

sign changes at every point $\phi_n = \arctan(-\sqrt{k}l^*) \pm n\pi$, $n \geq 1$.

It is possible to split the integration interval i times, being i the number of ϕ_n solutions where $0 < \phi_n < \sqrt{k}L$. On each of those intervals, the absolute value definition can be removed and replaced by the corresponding expression in Eq. (6.6), having only a difference in sign. By defining the primitive \mathcal{F} in an interval where the factor inside the absolute value is positive it is possible to evaluate F as it is shown in Eq. (6.7).

$$F(\sqrt{k}L, \sqrt{k}l^*) = \mathcal{F}|_0^{\phi_1} - \mathcal{F}|_{\phi_1}^{\phi_2} + \mathcal{F}|_{\phi_2}^{\phi_3} - \mathcal{F}|_{\phi_3}^{\phi_4} + \cdots \pm \mathcal{F}|_{\phi_i}^{\sqrt{k}L} \quad (6.7)$$

The change of signs in each interval is only given by the absolute value definition, then, it is simpler to add the absolute value of each contribution.

$$F(\sqrt{k}L, \sqrt{k}l^*) = |\mathcal{F}|_0^{\phi_1}| + |\mathcal{F}|_{\phi_1}^{\phi_2}| + |\mathcal{F}|_{\phi_2}^{\phi_3}| + |\mathcal{F}|_{\phi_3}^{\phi_4}| + \cdots + |\mathcal{F}|_{\phi_i}^{\sqrt{k}L}| \quad (6.8)$$

If we know the primitive \mathcal{F} and we are able to calculate the ϕ_n s in the integration interval, then, it is possible to calculate the factor F without using an approximate integrator. The double integration has been simplified to a primitive evaluation.

The primitive \mathcal{F} exists and it has been calculated using Maxima [26] and Wolfram Alpha Mathematica[27] software, the expression is in Appendix A.

6.3 Mitigating the impact on the beam size

6.3.1 QD0 length

As shown in Sect. 6.1 the Oide beam size contribution depends on a combination of beam and optics parameters. If none of the beam parameters is to be changed then F can be used as a figure of merit of the optics as it is calculated only from k , L and l^* . The target is to reduce it as much as possible. Two energy cases are analyzed in the following: 3 TeV ($l^* = 3.5$ m) and 500 GeV ($l^* = 4.3$ m).

Columns σ_0 , σ_{oide} and F in Table 6.1 show that CLIC 3 TeV and 500 GeV [9, 28] have larger contributions to beam size even having a lower F value than ILC 500 GeV [25].

In order to evaluate the minimum possible F for l^* given, the minimum k required to get the particles focused is when the Twiss function α is zero just at the quadrupole opposite face to the IP.

Figure 6.2a shows the ratio squared between the beam size contribution due to Oide effect and the linear beam size for three cases: when k is the minimum required to get particles focused (to get $\alpha_y = 0$ at QD0 opposite side to the IP), when k is calculated as thin lens ($k = \frac{1}{Ll^*}$), and the current QD0 status. Fig. 6.2b shows the k values for the previous mentioned cases.

The Oide contribution to beam size is of the same order of the linear beam size. It might be possible to reduce it by doubling the current quad length and using a lower k between the minimum required for the focusing and the thin lens approximation. This also points to increasing the lattice length as this change reduces the tolerance to variations of α at the quadrupole input.

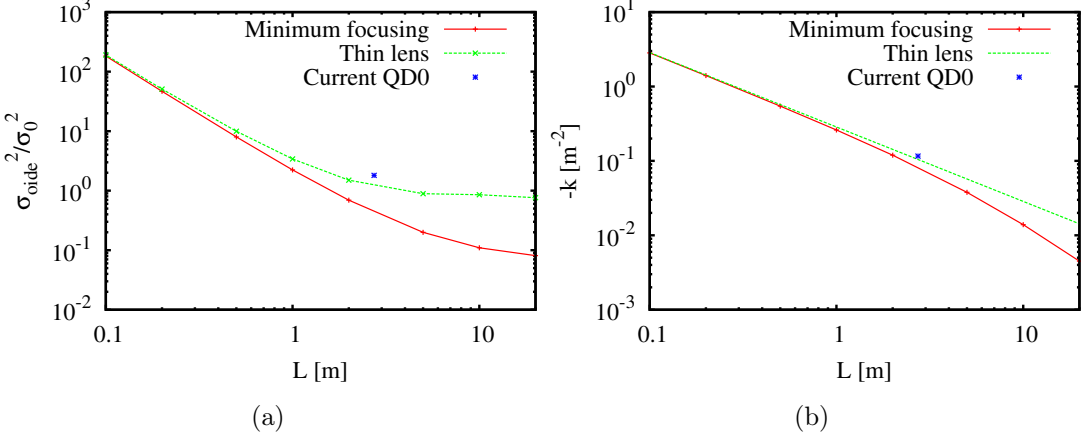


Figure 6.2 – Oide effect beam size contribution for CLIC 3 TeV design parameters. (a) σ_{oxide}^2 normalized to designed linear beam size as a function of quad length for the minimum focusing k (when $\alpha_y = 0$ at the quadrupole opposite side to the IP), for k calculated as thin lens ($k = \frac{1}{Ll^*}$) and the current QD0. (b) k in the three previous cases for comparison.

Quad lengths larger than 10 m do not lead to further improvements with the current parameters.

Figure 6.3 is the corresponding to Fig. 6.2 for the 500 GeV case. The current design contributes less than 4% of the total beam size, concluding that the current QD0 length with the CLIC 500 GeV parameters does not need adjustment.

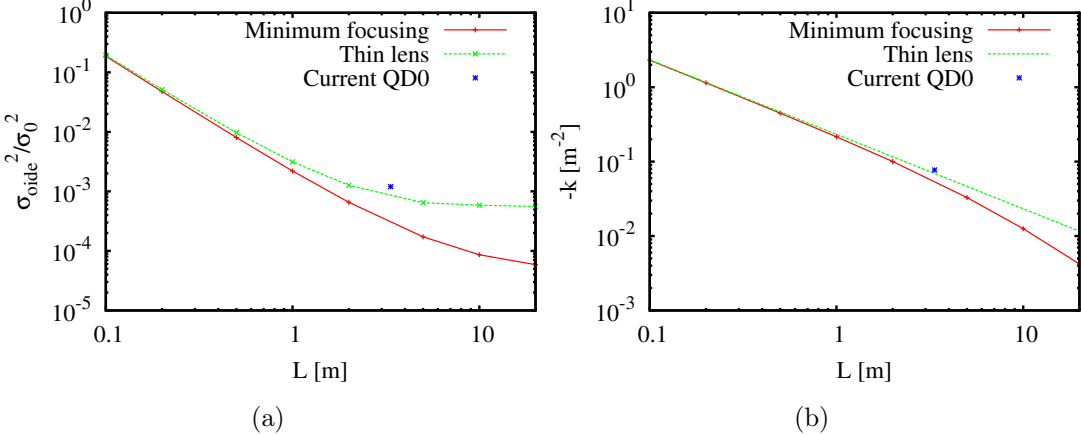


Figure 6.3 – Oide effect beam size contribution for CLIC 500 GeV design parameters. (a) σ_{oxide}^2 normalized to designed linear beam size as a function of quad length for the minimum focusing k (when $\alpha_y = 0$ at the quadrupole opposite side to the IP), for k calculated as thin lens ($k = \frac{1}{Ll^*}$) and the current QD0. (b) k in the three previous cases for comparison.

6.3.2 Correctors

Δy due to radiation

Particle tracking from the input of QD0 to the IP for CLIC 3 TeV with and without radiation, using PLACET [21], allows one to compute the effects of radiation on the six dimensional phase space. Figure 6.4 shows the current transverse distribution of particles at the IP. To

compensate the adverse effects a compensation system would ideally remove the position change due to radiation $\Delta y = y_{\text{rad}} - y_0$.

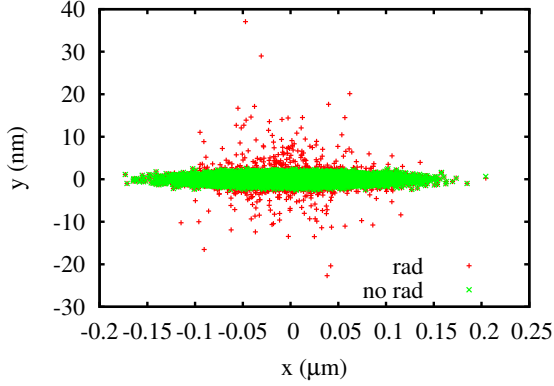


Figure 6.4 – CLIC 3 TeV beam at the IP after tracking through QD0 with and without radiation.

Although the average radiation effect is zero, $\langle \Delta y \rangle = 0$ because of the cubic term $(y'_0)^3$ as stated by Oide [24], the correlation between $\Delta y, y'$ is not zero. The correlation expression is shown in Eq. (6.9).

$$\langle \Delta y, y'_0 \rangle = \frac{2}{3} r_e \gamma^3 G(\sqrt{K}L, \sqrt{K}L^*) (y'_0)^3 \quad (6.9)$$

where $G(\sqrt{K}L, \sqrt{K}L^*)$ is given by

$$\int_0^{\sqrt{K}L} (\sin \phi + \sqrt{K}L^* \cos \phi)^2 \int_0^\phi (\sin \phi' + \sqrt{K}L^* \cos \phi')^2 d\phi' d\phi \quad (6.10)$$

Fig. 6.5 shows the comparison between the correlation obtained from tracking and the theoretical evaluation of the previous expression.

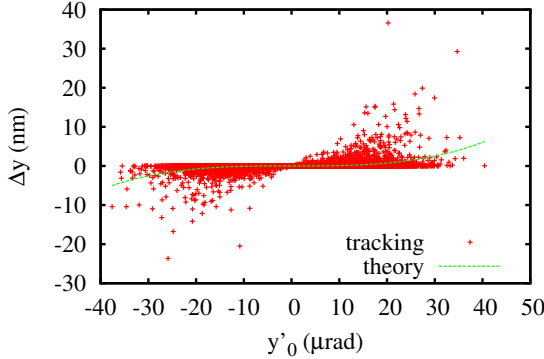


Figure 6.5 – Correlation between the phase space coordinates $\Delta y, y'$ for CLIC 3 TeV from particle tracking and theoretical expression in Eq. (6.9).

This correlation could be removed from the beam size by a set of octupolar correctors to be presented in next Section.

Correctors

A pair of correctors, placed as in Fig. 6.6, is added to the strong focusing in order to mitigate the radiation effect. Particles that did not radiate along QD0 receive kicks in C1 and C0

cancelling one another. However, the C1 and C0 kicks do not cancel for particles that did radiate, this difference is used to correct only the particles trajectory change due to radiation.

The procedure consists in scanning the best position and multipole gradient (s, k_i) for C0, and then set C1 at QD0 input to cancel the effect of C0. If two points with same β_y/β_x ratio are chosen, then the mutual cancellation of C1 and C0 correctors is limited only by the phase advance between them [13] and angle dispersion in the general case. Figure 6.7 shows the horizontal and vertical β functions for CLIC 3 TeV in FD region, and their ratio.

The equal β_y/β_x ratio for C0 and C1 condition is difficult to fulfill because C0 should be too close to the IP. In addition, it will lead to correctors running at very high strengths perturbing the beam.

A second approach is to minimize the phase advance between correctors. Therefore they will be located on both faces of QD0. This has the advantage of correctors running at lower strengths thanks to large β functions.

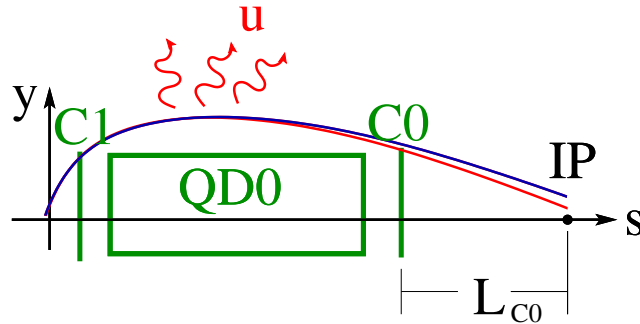


Figure 6.6 – For the nominal trajectory in blue, the kick in C1 must cancel the kick in C0. For all particles that radiate in red, the difference in kicks should cancel Δy .

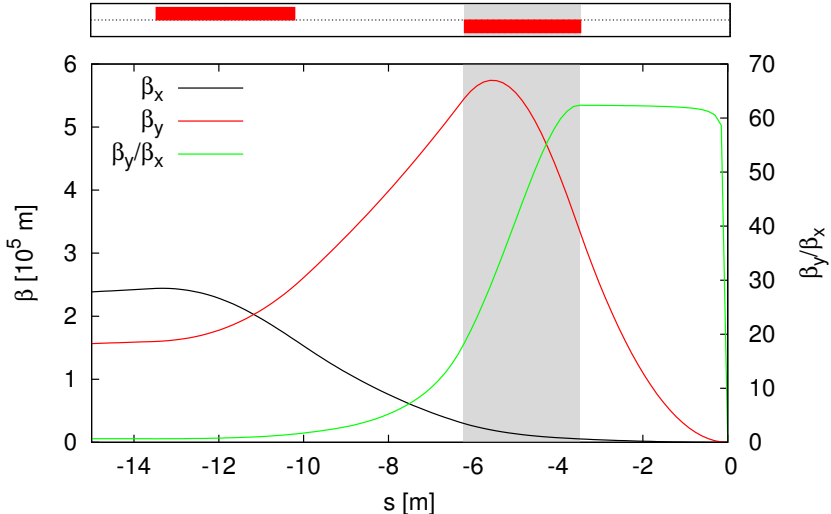


Figure 6.7 – β functions and β_y/β_x ratio for CLIC 3 TeV FD, QF1 and QD0 in red on top. The dark area is occupied by QD0 and the IP is at $s = 0$.

Two octupoles (OD0,OD1) were tried as correctors (C0,C1) to subtract the cubic fit. A CLIC 3 TeV nominal beam with no energy spread is generated at the IP and tracked back to the entrance of the C1 without radiation with both correctors off. This beam is used to study the Oide effect mitigation in QD0 using correctors by tracking to the IP with radiation.

The best result obtained with the octupole correctors is a vertical beam size reduction by

$(-4.3 \pm 0.2)\%$ using OD0 only. Table 6.2 shows the result of luminosity changes less than 10% for the case with no radiation in QD0, with radiation, with one corrector and with the two correctors obtained with Guinea Pig ++ [29].

	OD1		OD0		σ_x	σ_y	L_{tot}	L_{peak}
	L [m]	k_3 [m^{-4}]	L [m]	k_3 [m^{-4}]	[nm]	[nm]	[$10^{34} \text{cm}^{-2} \cdot \text{s}^{-1}$]	[$10^{34} \text{cm}^{-2} \cdot \text{s}^{-1}$]
NO RAD	0.01	0	0.01	0	47.45	0.69	7.7	2.9
RAD	0.01	0	0.01	0	47.45	1.18	7.5	2.7
RAD	0.01	0	0.01	-3900	47.45	1.13	7.4	2.7
RAD	0.01	1502	0.01	-3900	47.45	1.17	7.1	2.7

Table 6.2 – Effect of octupolar correctors on the beam size, total luminosity and peak luminosity.

The Oide effect contribution to vertical beam size affects very little the luminosity. The single corrector option., OD0, does not show any improvement in peak luminosities. However, the case of two correctors OD1 and OD0 shows a drop in the total luminosity. This has been attributed to the limited cancellation between correctors due to different β_y/β_x ratio and phase advance.

The possibility of slicing QD0 in two or three sections and mitigate the radiation effect with a pair of octupoles on each/any slice could be studied.

6.3.3 Conclusions

Radiation in the final quad sets a limit on the vertical beamsize, this is called Oide effect. Only for CLIC 3 TeV this limit is significant, therefore two possibilities have been explored to mitigate its contribution to beam size: double the length and reduce the QD0 gradient, or the integration of a pair of octupoles before and after QD0.

The best result with octupoles demonstrated vertical beam size reduction of $(4.3 \pm 0.2)\%$, with little or negative impact on luminosity. The correction scheme is currently limited by the phase advance and β_y/β_x ratio between correctors. It may be possible to improve its performance by slicing QD0.

Part III

BPMs at the ATF2 Interaction Point (IPBPMs)

Chapter 7

Relevance of ATF/ATF2

7.1 Facility purpose

The main objective of the Accelerator Test Facility (ATF) built at the High Energy Accelerator Research Organization (KEK) in Tsukuba, Japan, is to serve as R&D platform for the requirements of linear accelerators, in particular ILC. ATF obtained the record of minimum vertical beam emittance [30, 31], see Table 7.1, leading to the next step, the vertical beam size reduction at the IP.

The Final Focus Test Beam (FFTB) [32], at the Stanford Linear Accelerator Center (SLAC) in the U.S.A., explored the beam size reduction using the non-local chromaticity correction scheme. It operated since 1994 to 1997 with a final result of 70nm in the vertical plane. The nominal 40 nm was not achieved and the difference was attributed to beam jitter and tuning limitations [33].

The beam size reduction using the local chromaticity correction is explored by an extension of the original design, called ATF2 [34, 35], which involves an ILC-like FFS lattice scaled down to 100 m with two goals: (**goal 1**) achieve 37 nm of vertical beam size at the IP and (**goal 2**) the stabilization of the IP beam position at the level of few nanometres.

The CLIC, ILC and ATF2 main parameters are shown in Table 7.1, where the vertical chromaticity ξ_y is similar for ATF2 and ILC designs. The ILC and ATF2 relative increase in beam size is a factor 10, calculated from L^* , β^* and σ_δ , if chromaticity is not corrected.

Parameter	Symbol	Units	CLIC 3 TeV	CLIC 500 GeV	ILC	ATF2
Beam Energy per beam	E	GeV	3000	250	250	1.3
Energy Spread (e^+ / e^-)	σ_δ	%	0.3	0.3	0.07/0.12	0.06~0.08
Final quad to IP distance	L^*	m	3.5	4.3	3.5/4.5†	1.0
Horizontal β function at the IP	β_x^*	mm	6.9	9	11	4
Vertical β function at the IP	β_y^*	mm	0.07	0.2	0.48	0.1
Normalized horizontal emittance	ϵ_{xN}^*	μm	660	2400	10	2.8
Normalized vertical emittance	ϵ_{yN}^*	nm	20	25	35	31
Horizontal beam size	σ_x^*	nm	45	200	5.9	37
Vertical beam size	σ_y^*	nm	0.9	2.3	5.9	37
Natural vertical chromaticity	ξ_y		50000	43000	7300/9400†	10000

Table 7.1 – Design parameters of ILC and ATF2 Final Focus. †The ILC lattice has two detector options: SiD and ILD.

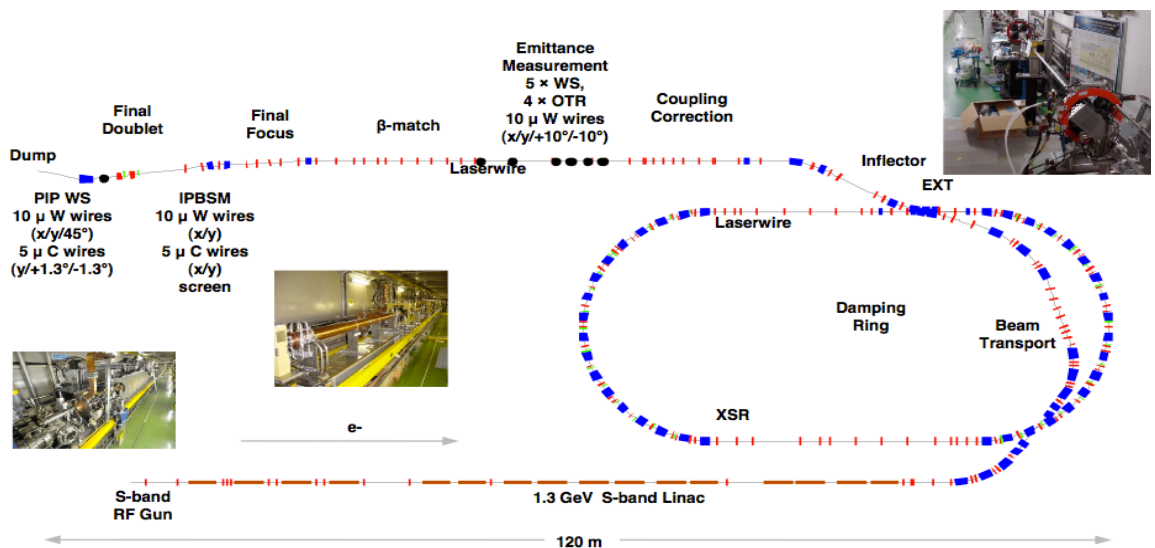
When compared with the current linear accelerator projects, ATF2 will not be as sensitive to time variations due to ground motion and wakefields, nor to misalignments, because the ATF2 FFS in an order of magnitude shorter than in ILC and because of the larger geometric

emittances involved. However the tolerances to magnetic fields, jitter vibration and power supply stability are similar in ATF2 and ILC.

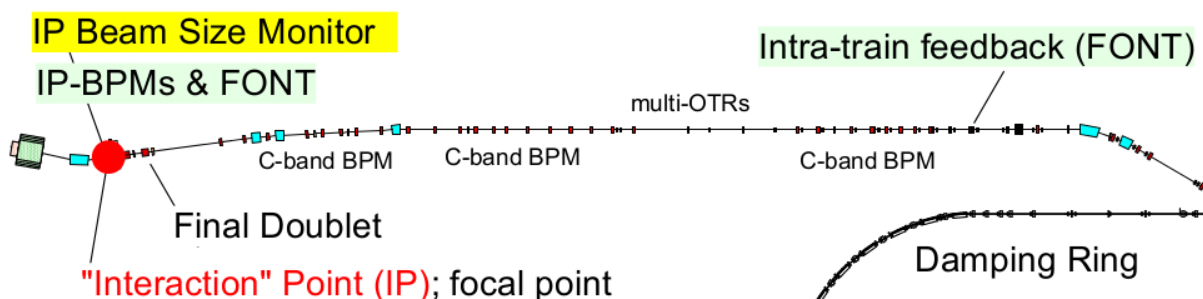
On the other side, ATF2 needs dedicated systems to measure the beam position and beam size at the IP because the focusing effects of beam-beam interactions used in a collider are not applicable.

7.2 Beam line Description

The ATF accelerator facility, shown in Fig. 7.1, is composed of a photocathode giving electrons to a linac which accelerates the particles to 1.3 GeV, a damping ring to reduce the beam vertical and horizontal emittances and an extraction line which provides bunch packets to the Final Focus Section (FFS) where the beam is transported to the nominal IP and dump. The goal is to generate, accelerate and damp a train of 20 bunches with 2×10^{10} particles per bunch and 2.8 ns bunch spacing. A detailed description is available in [34, 36, 37].



(a) Disposition of the Accelerator Test Facility (ATF), composed by a photocathode, a linac to 1.3GeV, a damping ring, an extraction line, the Final Focus (FF), and the beam dump.



(b) Zoom over the extraction line, and Final Focus Section, highlighting the nominal Interaction Point location (IP). This region is known as ATF2.

Figure 7.1 – Diagrams containing the ATF composition and a zoom on the ATF2 section.

7.2.1 The RF Gun and Linac

The total length of the linac is 80 m divided in: 18 m for the pre-injector section, a 70 m long accelerator section with energy compensation structures and 12 m for the transport line to the damping ring (DR) and a positron test stand. The RF gun with a 1.6 cell S-Band Cs₂Te photocathode generates an electron beam with intensity up to 3.2nC per bunch. The pre-injector contains also an accelerating structure. An accelerating field of 35.2 MeV/m is required to accelerate 20 bunches of 2×10^{10} particles per bunch. The linac is operated at a repetition rate of 25 pps (pulses per second) to allow circulating 5 bunch trains in the Damping ring. Table 7.2 shows the main parameters of the DR.

Beam energy, E_{beam}	1.54 GeV
Bunch population, N	2×10^{10}
Bunches per train, N_b	20
Bunch spacing, Δt_{bunch}	2.8 ns
Energy spread Full Width, σ_δ	<1.0% (90% beam)
Normalized emittance, $\epsilon_{Nx/y}$	$< 3 \times 10^{-4}$ m·rad

Table 7.2 – Basic design parameters of the ATF injector linac.

7.2.2 The Damping Ring

The ring has a length of 138.6 m. It has achieved in 2004 a vertical normalized emittance of 1.5×10^{-8} m·rad, equivalent to 6pm·rad for a bunch intensity of 10^{10} particles. It was achieved by a precise alignment of components and beam control. The structure is a combination of bending magnets and wiggler cells where the value of the horizontal emittance is determined by the structure unit cell. The wigglers reduce the damping time and each bend is placed at the minimum of the dispersion in each periodic structure. The ATF DR consists in 36 of these units cells and the main parameters are in Table 7.3.

Beam energy, E_{beam}	1.54 GeV
Bunch population, N	2×10^{10}
Bunches per train, N_b	20
Bunch spacing, Δt_{bunch}	2.8 ns
Energy spread Full Width, σ_δ	<1.0% (90% beam)
Normalized emittance, $\epsilon_{Nx/y}$	$3 \times 10^{-6}/3 \times 10^{-8}$ m·rad

Table 7.3 – ATF DR main parameters.

7.2.3 The extraction line

In the extraction line the beam is extracted from the DR by means of a first kicker (KICKER1), and then passes off-axis through two quadrupoles centered on the DR reference orbit. Then, the beam passes through three septum magnets which complete the extraction. After the extraction, the beam passes through a dispersion suppressor section to reduce fluctuations.

There are two extraction modes: single bunch and multibunch.

In single bunch mode one bunch is extracted approximately every 1/3 s from the damping ring

to the ATF2 line. In multibunch mode a train of up to 20 bunches is extracted from the damping ring. The number of bunches and spacing are set by the damping ring fill up.

7.2.4 The extraction diagnostic section

After the extraction, the diagnostic section is used for measuring the emittance and dispersion, and correcting betatron coupling. This section has been designed to be as close as possible to the ideal skew correction described in [38].

The measured vertical emittance in the diagnostic region downstream shows typically a factor 3 increase with respect to values obtained in the DR and dependence with beam intensity. One of the possibilities of the emittance growth is the non-linearity of the magnetic fields in the extraction region experienced by the beam when passing off-axis. One second possibility is the wakefields induced by the extraction kicker. The correlation with beam intensity is not fully understood; it could be due to the beam position monitors response.

Connecting dispersion and betatron matching plus careful alignment are the keys to mitigate the factor 3 increase in vertical emittance.

7.2.5 The ATF2 lattice

The ATF2 lattice can be subdivided in two sections : the matching section and the FFS. The following section describes the FFS.

The FFS focuses the beam to a small vertical beam size following the telescope design with local chromaticity correction, as in Sect. 2.4.4. The top of Fig. 7.2 shows the lattice elements and the optics functions along the FFS. The Final Doublet (FD), QD0FF and QF1FF, provide the vertical and horizontal focusing, respectively. The horizontal off-momentum function η and the pair of sextupoles in the FD are used to cancel the beam size dependence on energy spread at the IP.

The second pair of sextupoles in the lattice section from 70 to 75 m are used to cancel the geometrical components induced by the sextupoles in the FD. And, additional chromaticity is created upstream QF7 to match the local correction [11], see Section 2.4.4.

Quadrupole displacements are used to steer the beam, while sextupole displacements are used to induce corrective focusing (normal and skew components for horizontal and vertical displacements, respectively). This has an impact on the beam size. The tolerances to misalignments, roll angle and magnet strength errors in the FFS have been initially studied with a target of 2% impact on the beam size, and it has resulted in similar tolerances as in ILC [37]. All quadrupoles and sextupoles are placed on individual movers to allow the beam steering and adjustment of relative alignment in X, Y and Roll angle.

7.2.6 The IP Region

The β functions at the IP, β^* , can be set by changing the matching section quadrupole strengths. Three configurations are normally used : 1BX1BY, 10BX1BY, and 100BX1000BY, where the factor indicates the number of times that the original β^* has been amplified.

The 1BX1BY optics has the original design parameters. Here the angular divergence of the beam is 0.35 mrad vertically and 0.52 mrad horizontally in the IP region.

The 10BX1BY preserves the β_y^* goal while relaxing the tolerance to multipole errors in

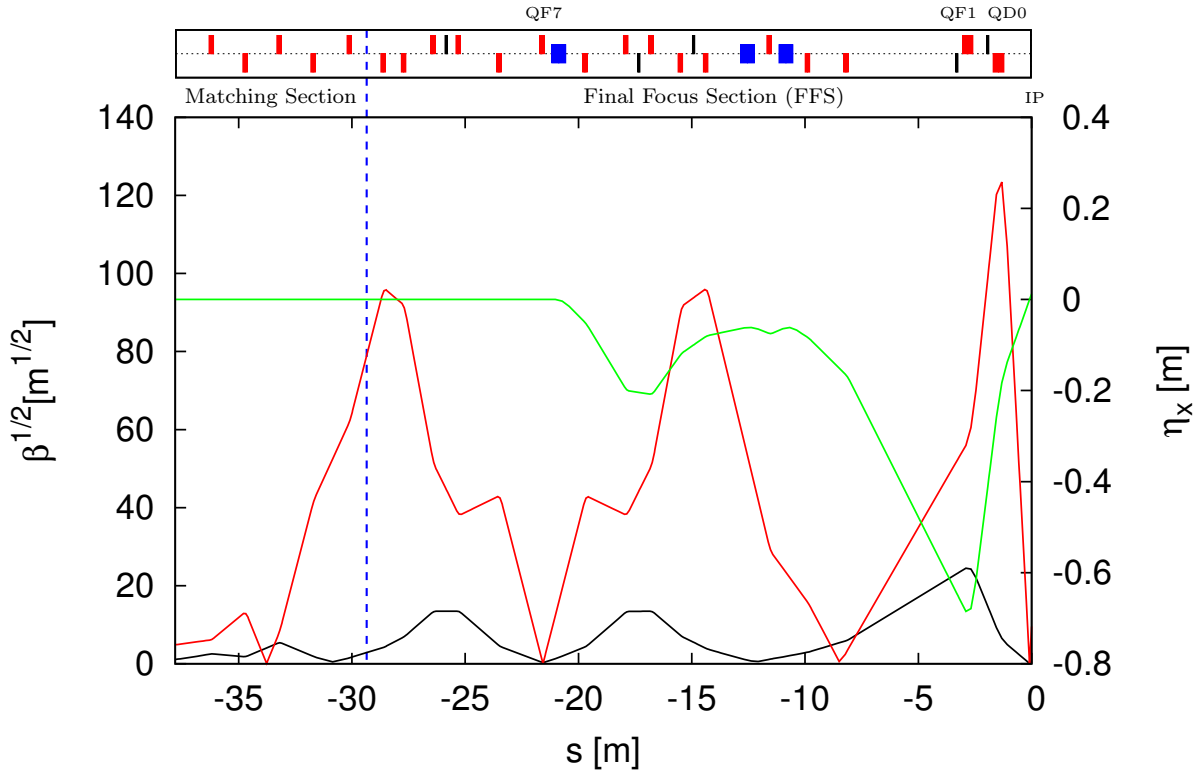


Figure 7.2 – Optical functions in the Final Focus Section at ATF2. On top is the ATF2 lattice: dipoles in blue, quadrupoles in red and sextupoles in black.

magnets by increasing ten times the original β_x^* , making them comparable with those of ILC 500 GeV [39]. This optics is the one shown in Fig. 7.2 and it is currently used in operation.

The 100BX1000BY optics sets a parallel beam through the IP area by enlarging the beam size at the IP. It is principally used to avoid the issues of large angle divergence displayed by the 1BX1BY optics.

Even smaller β_y^* functions have been explored recently at ATF2 aiming to investigate resulting increases in tuning difficulty and beam size measurements limitations [40].

Figure 7.3 shows the beam size in vertical and horizontal planes for several optics combinations in a region of 300 mm around the IP. It also shows clearly how the beam divergence affects the beam size along the IP region.

The QD0 strength sets the vertical beam waist location with a small impact on the horizontal beam waist location, and viceversa for the QF1. The two are set to put the beam waist to its the nominal location at $s = 0$. However, one or a combination of the two quadrupole strengths can be used to bring the beam waist to any location upstream or downstream. Moving the beam waist along the section of the IP region displayed in Fig. 7.3 is effectively changing the focal distance by less than -20% to +10%.

QD0 and QF1 horizontal and vertical movers can also be used to steer the beam in the FD region, changing the position and angle through the IP region. Angles can also be steered by moving QF7 horizontally and vertically because of its location near a focal point upstream. See Fig. 7.1b showing the QF7 location and Eq. (2.3) to see that the kick at the input of a telescope lattice affects only the angle at the output.

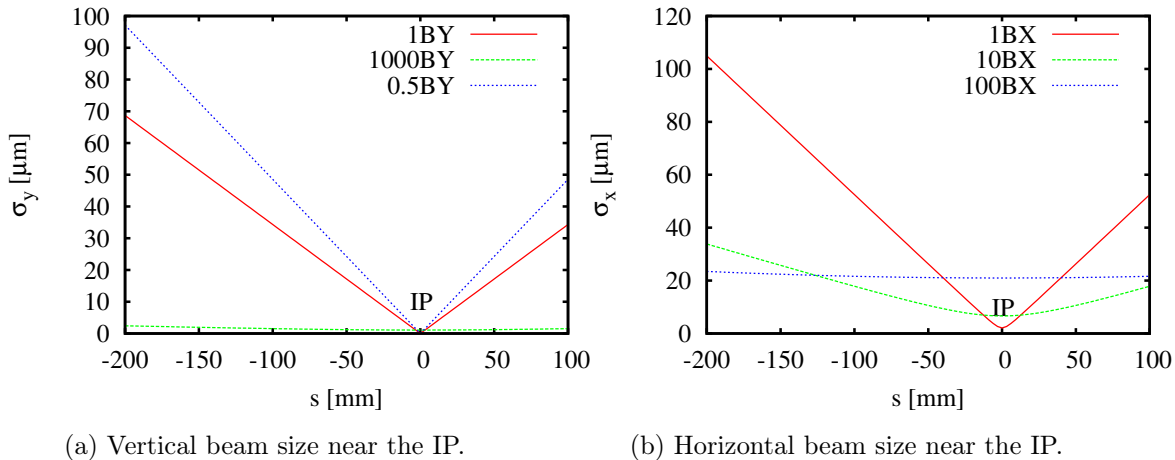


Figure 7.3 – Vertical and horizontal beam sizes for 1BY, 1000BY, and 0.5BY in the vertical plane, and 1BX, 10BX and 100BX in the horizontal plane.

7.3 Beam Size Measurement at the IP

A direct beam size measurement at the ATF2 IP is required because it can not be deduced from beam-beam effects as in a collider.

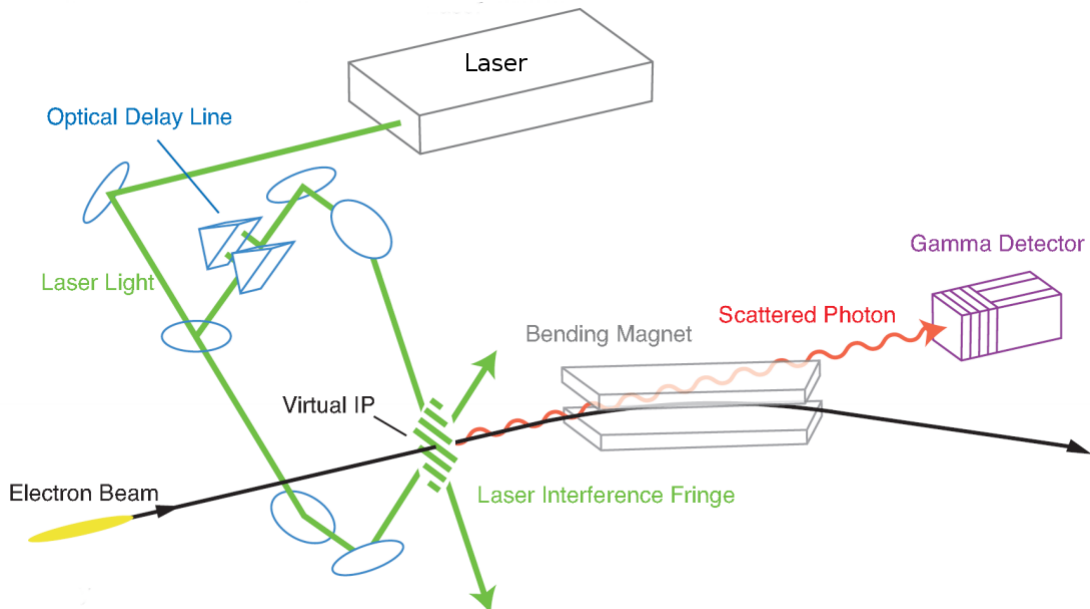


Figure 7.4 – IPBSM schematic design. The particle beams cross the interference pattern generated by a perpendicular laser beam. The number of electron-photon interactions varies with the fringe size and the particle beam size.

The Beam Size Monitor (IPBSM) measures the number of scattered photons from an electron-photon collision between the particle bunch and a perpendicular interference pattern generated by high intensity laser perpendicular to the bunch trajectory [41]. The number of photons is proportional to the photon density at the beam position. Moving the beam or scanning the phase of the laser fringe produces a modulation of gamma flux ray, the amplitude of which depends on beam size [37]. Figure 7.4 shows a schematic design of the IPBSM.

Such a device was previously used at the FFTB line at SLAC [42]. A similar one is now located in the IP region at ATF2 [43].

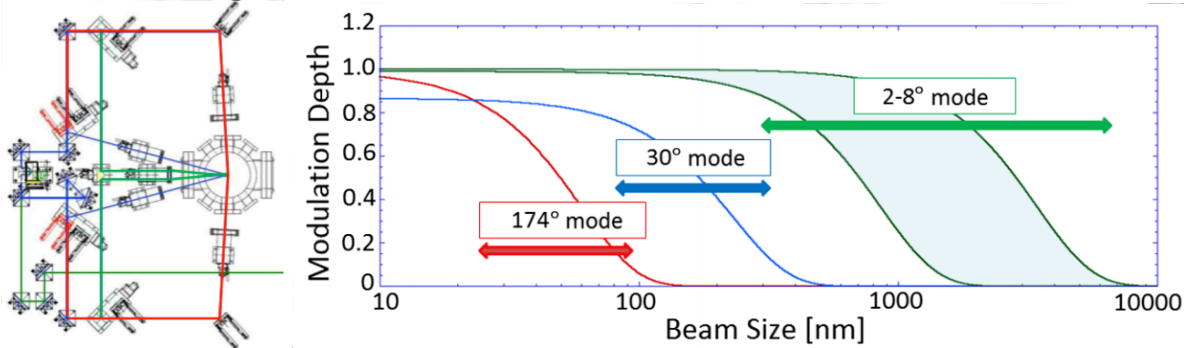


Figure 7.5 – (Right) IPBSM laser path over the optical table perpendicular to the beam propagation. (Left) Beam size resolution for the angle modes : $2 \sim 8^\circ$ in green, 30° in blue and 174° in red.

At ATF2, it is installed on a vertical optical table where the laser incident angle can be adjusted to change the interference fringe pitch allowing measurements of beam sizes from $6 \mu\text{m}$ down to 25 nm . Figure 7.5 shows the laser beam paths along the vertical optical table for three angle modes and the corresponding ranges of possible beam measurements.

Larger beam sizes are measured by a wire scanner installed in the same region. It consists in a wire moved across the beam generating bremsstrahlung gamma rays. The number of photons is proportional to the charge of the slice interacting with the wire at each position setting. Profiles are constructed from the number of photons as a function of wire position [44].

7.4 Beam stabilization

Three regimes are defined for the beam stability: random fluctuations over timescales which are effectively uncorrectable (jitter), fast variations that can be corrected by feedback (FB) systems, and slow or static changes that can be addressed by systematic orbit correction (tuning).

The jitter requirement for goal 1 is beam jitter less than 30% of σ_y , while goal 2 requires jitter less than 5% of σ_y . The measured bunch position jitter upstream of the FD for single bunch extraction mode, i.e. the fluctuations on bunch position before the last strong focusing magnets, is around $10\sim20\%$ of beam size in the vertical plane and $5\sim10\%$ on the horizontal plane [45]. Additional jitter could come from the mechanical vibration of the FD.

7.4.1 Tuning

The contribution to beam size due to field errors is considered static or slowly changing. It is possible to reduce their impact by systematic orbit correction using magnetic or mechanical means [34]. Goal 1 jitter requirements can be achieved for single bunch extraction.

7.4.2 Feedback

The fluctuations coming from ground motion, magnet strength variations, changes in the damping ring, energy oscillations are considered fast errors. Also, the bunch to bunch jitter

from multibunch extraction requires active correction.

The feedback system is then the last line of defense to correct the beam trajectory and three schemes are tested in ATF2 using two bunches.

- Upstream FB: Measures the first bunch position in the IP region and uses a set of kickers upstream of the matching section to stabilize the position of the second bunch.
- Feedforward: Measures the first bunch position upstream of the matching section and uses a kicker in the IP region to stabilize the position of a second.
- Local IP FB: Measures the first bunch position in the IP region and uses a kicker in the IP region to stabilize the position of a second.

7.5 Recent achievements and current work

In 2014 vertical beam size about 55 nm was observed at ATF2 [46], and since then smaller beam size are achieved as a regular basis down to 44 nm [47], demonstrating the local chromaticity correction method at charges of about 0.1×10^{10} particules per bunch.

A main identified issue, intensity dependence, is currently explored by the ATF2 collaboration. Nonetheless, at low intensities, the beam size remains above the design 37 nm. Possible contributions are: (1) the increase of the incoming beam emittance along the ATF2 line, (2) systematic errors and resolution limitations on the beam size monitor, (3) beam drift/jitter beyond the tolerable margin and (4) undetected optics mismatch.

Last two issues can be addressed by measuring the beam trajectory in the IP Region after the Final Doublet. In addition, looking forward to **goal 2**, beam position measurement is a requirement for beam stabilization.

The work here described corresponds to the beam position monitors installed in 2013 by LAL in collaboration with Kyungpook National University (KNU), the Feedback in Nanosecond Timescale (FONT) group from Oxford, and the ATF2 staff.

7.6 Position Measurement Requirements

A direct beam position measurement at the ATF2 IP is required because it can not be deduced from beam-beam focusing effects as in a collider [48].

Knowing the beam trajectory with nanometric precision is valuable information for beam tuning and a requirement for feedback. The position measurement system could be used to correct the beam positions used in the reconstruction of the IPBSM modulation pattern, in order to remove the dilution from beam jitter in the beam size reconstruction pulse by pulse.

Therefore, a set of three cavities (IPA, IPB and IPC), two upstream and one downstream of the nominal IP, were installed and are used to measure the beam trajectory in the IP region, thus providing enough information to reconstruct the bunch position and angle at the IP.

Cavities are located at $s = -167.9$ mm, $s = -87.1$ mm and $s = 87.1$ mm, with respect to the nominal IP at $s = 0$. It has been shown in section 7.2.6 the effect of different optics on the beam size along the IP region. As the measured beam jitter upstream is around $10 \sim 20\%$ of beam size, then, the change of optics will have a direct impact on the dynamic range of the position measurement.

Dynamic Range

Table 7.4 shows that beam size only increases by a factor two among the cavities using the 1000BY optics, while Table 7.5 shows a beam one and two thousand times larger than the beam size at the focal point, due to the large divergence in the nominal optics.

From these optics settings the maximum vertical beam size is $58 \mu\text{m}$. The dynamic range required for the cavity is then around 10 to 11 μm using the 20% jitter to beam size ratio.

	IPA	IPB	IP	IPC
s [mm]	-174.2	-87.1	0	87.1
σ_y [$1.086 \mu\text{m}$]	2.0	1.3	1	1.3
$\sigma_{y'}$ [0.011 mrad]	0.5	0.8	1	0.8

Table 7.4 – Vertical beam size at the cavities positions and the IP with the 1000BY optics.

	IPA	IPB	IP	IPC
s [mm]	-174.2	-87.1	0	87.1
σ_y [34 nm]	1.7×10^3	871	1	871
$\sigma_{y'}$ [0.3 mrad]	$0.6(10^{-3})$	$1.2(10^{-3})$	1	$1.2(10^{-3})$

Table 7.5 – Vertical beam size at the cavities positions and the IP with the 1BY optics.

Resolution and Calibration

The beam stabilization to the nanometer level requires position measurement with nanometric resolution. In addition, due to the low β^* for the nominal 1BX1BY optics, the beam size and therefore the jitter increases rapidly making the 1 nm resolution over the 10 μm dynamic range a challenge. The calibrations must be then valid for measurement over 3 to 4 order of magnitude.

Chapter 8

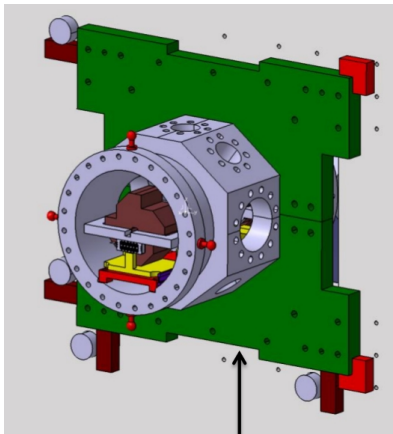
BPMs System description

In this section I describe the beam position monitor (BPM) system installed at the IP region and the signal analysis method used to test the system.

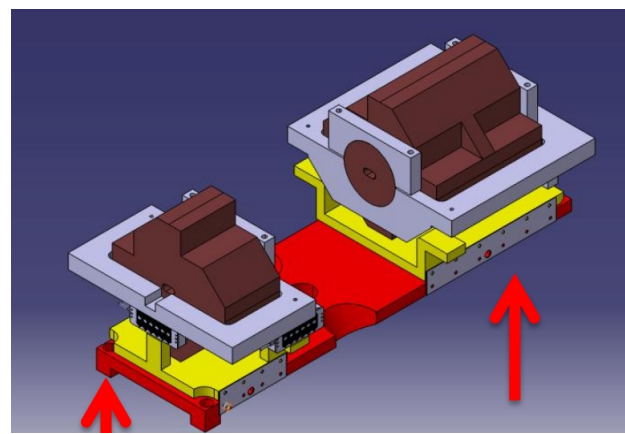
8.1 The system

The system consists in three cavities inside a vacuum chamber shown in Fig. 8.1a which is fixed to the optical table used for the IPBSM laser and optical instruments. Flanges and viewports on the sides are compatible with the IPBSM operation. Inside the chamber, a system of three cavities (IPA, IPB and IPC) are installed in two separated blocks: one block upstream for IPA and IPB and the other downstream of the IP for IPC.

Each block is placed on top of a piezo-electric displacement system shown in Fig. 8.1b with three degrees of freedom: vertical displacement, horizontal displacement and pitch angle. Position and angle conventions can be seen in Annex B.2.



(a) Vacuum chamber design.



(b) Piezo-electric displacement system and cavities.

This piezo mover system is remotely controlled to align the cavities with the beam, and to do systematic studies of the cavity sensitivity to position change. A set of in-vacuum PT100 thermal gauges are included on each block. The initial checks on the system can be consulted in [49], and the control and readout scheme can be seen in Annex B with alignment results.

8.1.1 The cavities

Cavities for beam position measurement must have good stability since precision depends on mechanical precision. Resolution at thermal noise level of the readout electronics can be achieved by narrowing the dynamic range and using high gain electronics since signal is small near the cavity center. The following is a description of the cavity parameters as presented by Nakamura in [50].

Cavity modes

The cavity consists of a cavity and a waveguide. When the particles passes through the cavity, it resonates in several modes at frequencies given by the cavity dimension and shape [51].

Cylindrical coordinates are used for cylindrical cavities. The electric $E = (E_r, E_\phi, E_z)$ and magnetic field $B = (B_r, B_\phi, B_z)$ are excited in the cavity. For beam position monitoring the transverse mode (TM) $B = (B_r, B_\phi, 0)$ is essential. Three numbers m, n, l which are the mode numbers in r, ϕ, z are used to identify the modes. The TM₀₁₀ is the monopole mode and it is used for charge intensity measurement and downmixing of the signals from the position sensitive cavities. It is shown in Fig. 8.3.

In a similar way, rectangular coordinates are used for rectangular cavities. The electric $E = (E_x, E_y, E_z)$ and magnetic field $B = (B_x, B_y, B_z)$ are excited in the cavity. For beam position monitoring the TM $B = (B_x, B_y, 0)$ is essential. Three numbers m, n, l which are the node numbers in x, y, z are used to identify the modes. The TM₁₂₀ and TM₂₁₀ are the dipole modes and are used for bunch position measurement. The TM₁₁₀ is the monopole mode in rectangular cavities. They are shown in Fig. 8.2.

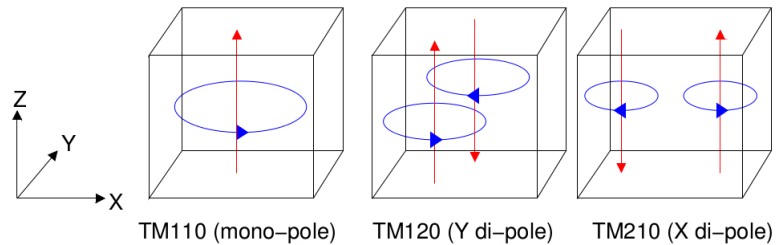


Figure 8.2 – Dipolar and monopolar mode in rectangular cavities.

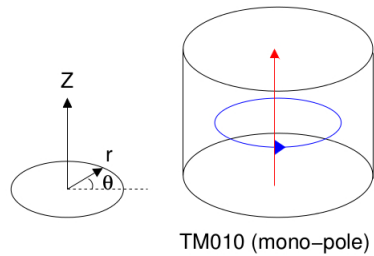


Figure 8.3 – Monopolar mode in cylindrical cavities.

Only the dipole mode is of interest for beam position measurement so it is separated from other modes which are considered noise components. The separation between the vertical and horizontal dipole mode is made by making the cavity rectangular, resulting in different resonant frequencies for each plane.

A set of slots is introduced on the cavity walls to couple only the dipole mode to a waveguide

with a cut-off frequency above the monopole mode. This is made to separate the dipole signal from large noise coming from the monopole component. An antenna picks up the signal in the waveguide and connects it to the output port. The cavity design has then four ports, two ports in antiphase per plane, one on each side. Figure 8.4 shows the cavity transversal plane with the four slots and the coupling to the waveguide and antenna for the horizontal ports.

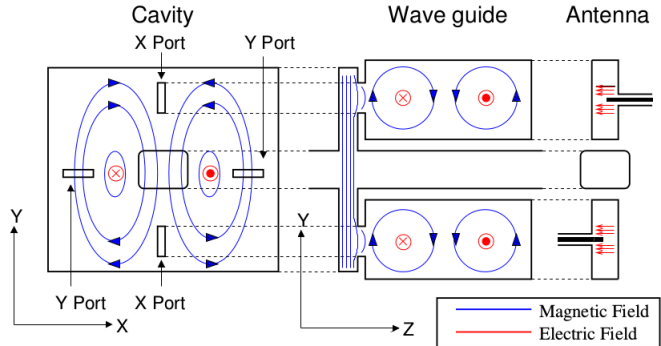


Figure 8.4 – Coupling to the dipole mode of the cavity.

Output signal

Voltage of a resonant mode excited in a cavity by a passing beam, V_{exc} , is expressed as

$$V_{exc} = \frac{\omega}{2} \left(\frac{R}{Q} \right) q \quad (8.1)$$

where ω is the resonant angular frequency of the mode, q is the beam charge, R is the shunt impedance and Q is the quality factor which represents the efficiency of the resonant mode of a cavity. The factor R/Q is

$$\frac{R}{Q} = \frac{|\int E \cdot ds|^2}{\omega U} \quad (8.2)$$

where U is the energy stored in the cavity and $E \cdot ds$ is the longitudinal component of the electric field in the cavity generated by the passing beam. The cavity design for the IP region targets high R/Q (high Q_0), minimizing the energy loss in the cavity walls and maximizing the output power.

The finite bunch length σ_z results in an effective reduction of V_{exc} given by the expression

$$V_{totalexc} = V_{exc} \exp \left(-\frac{\omega^2 \sigma_z^2}{c^2} \right) \quad (8.3)$$

The stored energy of a cavity is $U = V_{totalexc}^2 / (\omega R / Q)$, and the output power is $P_o = \omega U / Q_{ext}$, where Q_{ext} is the quality factor of the external coupling. Detecting the power output, P_o , by an impedance Z gives the output voltage

$$V_{out0} = \sqrt{Z P_o} = \frac{wq}{2} \sqrt{\frac{Z}{Q_{ext}} \frac{R}{Q}} \exp \left(-\frac{\omega^2 \sigma_z^2}{2c^2} \right) \quad (8.4)$$

The energy dissipation in the cavity is

$$U = U_0 e^{-\frac{\omega}{Q_L} t} \quad (8.5)$$

where $\frac{1}{Q_L} = \frac{1}{Q_0} + \frac{1}{Q_{ext}}$, and the energy decay time $\tau = Q_L/\omega$. As the signal is proportional to the square root of the power, then the signal decay time is a factor two smaller.

Finally, as the R/Q factor depends on the longitudinal component of the electric field, the integration depends on the TM mode. It has been derived in [50] concluding that in the dipole mode R/Q depends on the square of the bunch transverse position in the case of bunches passing near the center, while the monopole mode R/Q is independent of position. From this, the output voltage in the TM_{120} and TM_{210} is proportional to position, while TM_{110} and TM_{010} are not.

Components orthogonal to position

Additional components are present in the cavity signal output which are orthogonal to bunch position. They have been described in [50] as

$$V = V_{\text{position}} + iV_{\text{angle}} + iV_{\text{pitch}} + iV_{\text{commontail}} \quad (8.6)$$

where the imaginary factor i involves a $\pi/2$ phase difference, and the following is a brief description of each component:

- Angle: a cavity of length L gives a position voltage as $V_{\text{position}} = Ax\sqrt{L}\sin(\omega t)$. Assuming a beam passing through the cavity center making an angle x' , it can be decomposed as the sum of two position signals with $x = x'L/4$ and phase difference of $\pm L/4c$, affecting the amplitude by $\sin(\omega L/4c)$ and the phase by $\pi/2$. The ratio of angle to position signals for $\omega L/4c \ll 1$ is

$$\frac{|V_{\text{angle}}|}{|V_{\text{pos}}|} = \frac{\omega L^2}{2\sqrt{2}c} \frac{x'}{x} \quad (8.7)$$

- Pitch: a cavity gives a position voltage as $V_{\text{position}} = Aqx\sin(\omega t)$. The beam is decomposed in two points with $q/2$ total charge each, while traversing the cavity with an angle θ . The sum of two position signals with $q/2$ charge each, $x = \sigma_z\theta$ being σ_z the bunch charge, and phase difference of $\pm\sigma_z/c$ will affect the amplitude by $\theta\sigma_z^2/c$ and the phase by $\pi/2$. The ratio of angle to position signals is

$$\frac{|V_{\text{pitch}}|}{|V_{\text{pos}}|} = \frac{\omega\sigma_z^2}{c} \frac{\theta}{x} \quad (8.8)$$

- Commontail: the common-tail [52] comes from the monopole component. At the dipole component frequency it is 2 to 3 orders of magnitude stronger than the dipole component. However, it is attenuated by the coupling to the waveguide. Nakamura [50] shows that the phase advance between the monopole and the dipole signals is $\pi/2$.

The phase difference of these components allows one to remove them from the position signal by phase detection. In addition the cavity design was conceived to reduce the angle signal by making it short to mitigate the effects from the large beam divergence seen in Section 7.2.6.

Cavities at the IP Region

The three cavities (IPA, IPB and IPC) are rectangular and resonate in the TM_{210} and TM_{120} modes, at the C-band frequency of 5.7 and 6.4 GHz, in the horizontal and vertical planes, respectively. They have a design decay time of 19 ns (horizontal) and 17 ns (vertical), and sensitivities to bunch position of $2.2 \mu\text{V}/\text{nm}/\text{nC}$ (horizontal) and $3.7 \mu\text{V}/\text{nm}/\text{nC}$ (vertical). Two additional cylindrical cavities with decay time of 29 ns, sensitivity to bunch charge of

3.27 V/nC, one per resonant frequency, are placed downstream of the IP to measure the bunch charge and to enable downmixing the C-Band frequency signals in the readout (see Section 8.1.2); these are the reference cavities.

The IPA, IPB and IPC sensitivity to orthogonal components are: position to angle ratio of 3.2 $\mu\text{m}/\text{mrad}$, position to bunch pitch ratio of 8.6 $\mu\text{m}/\text{mrad}$ with $\sigma_z=8 \text{ mm}$ and unknown comtail component.

Previous to the installation, the cavity signals' decay time was measured giving the results shown in Table 8.1. In particular IPC shows a shorter decay time than IPA and IPB. The effect of the large difference between the design and the measured values on resolution is currently under investigation.

Plane	Design	IPA	IPB	IPC
X [ns]	19.41	8.722	8.181	4.925
Y [ns]	17.49	11.11	11.25	6.745

Table 8.1 – Measured decay time for the three cavities before installation.

The reference cavities have been tuned to match the measured resonant dipole frequency from the sensor cavities, showing maximum difference of 3.5 MHz in Table 8.2, and good agreement with the design.

Plane	Reference	Average	IPA	IPB	IPC
X [MHz]	5712	5712	-2	-2.5	+2.5
Y [MHz]	6426	6420	+1	0	-3.5

Table 8.2 – Resonant dipole frequency measurement at KEK before installation.

8.1.2 The processing electronics

Each position measurement cavity has two output ports in antiphase per plane connected to independent processing electronics to downmix the signals, separate them into two orthogonal components called I and Q , and set the gain according to beam charge conditions. A set of remotely-controllable attenuators, variable between 0-70 dB in steps of 10 dB can be used to increase the linear range of electronics at the expense of resolution.

At the moment the reference cavities are not used to downmix the position cavities signals directly to base band. Instead, as explained below, a 714 MHz signal from the DR is used to downmix the three cavity signals to 714 MHz in a first stage and then a second stage downmixes the position cavities to baseband using the reference cavity signal. This allows the installation of the second stage outside the ATF2 line, aiming at studying the signals with different phase detection settings changed by hand in the hardware. An scheme of the electronics is shown in Fig. 8.5. The following is a description of components extracted from [50].

- Combiner: The combiner outputs the difference of the signals. However, the signal from the two cavity ports are in antiphase so the net effect is factor 2 of amplification.
- Variable attenuator: it attenuates the input signal from 0 dB to 70 dB in steps of 10 dB. The purpose is to enlarge the dynamic range at the expense of resolution.

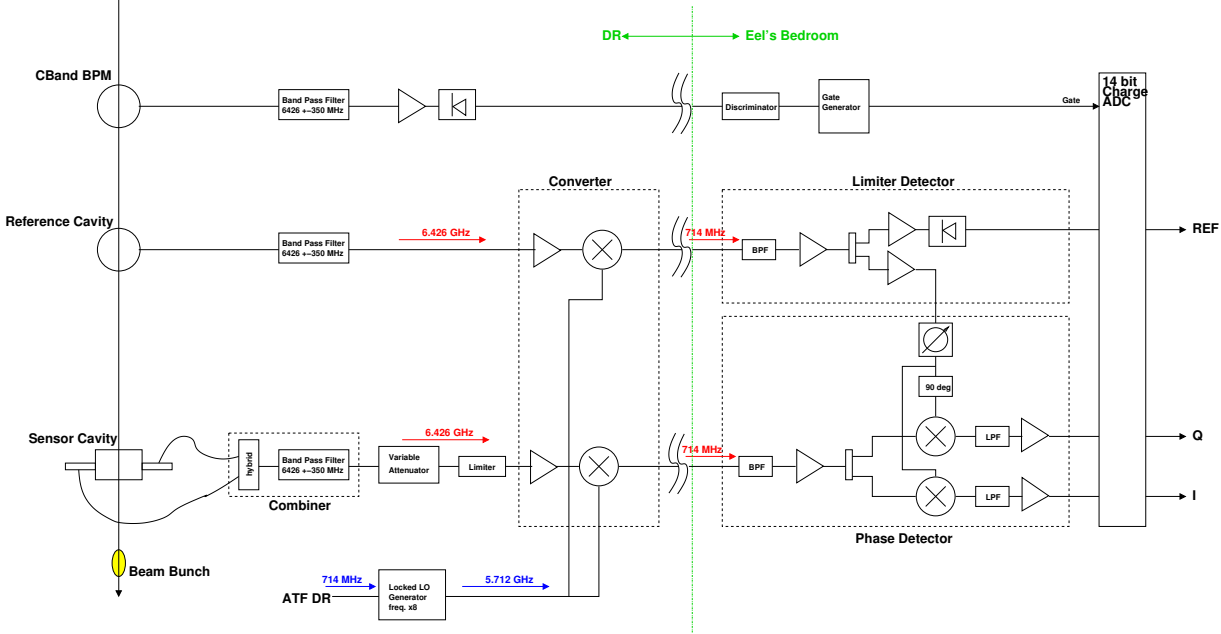


Figure 8.5 – Processing electronics per BPM per plane.

- First stage of down conversion: it downmixes the BPM and reference cavity signals to 714 MHz using an 8×714 MHz (for the vertical plane) and 9×714 MHz (for the horizontal plane) signal from the LOCKED LO module, and amplifies the output by 20 dB. It is required to do it as close as possible to the BPMs because of the short decay time.
- LOCKED LO: Multiplies the frequency of the DR 714 MHz by a factor 8 for the vertical plane and 9 for the horizontal plane to perform the first stage of signal downmixing.
- Limiter detector: Set a constant amplitude of the Reference signal at 714 MHz to be used for the downmixing in the second stage. Fig. 8.6 shows a diagram with 4 outputs to be used for downmixing. It also outputs the signal proportional to charge.
- Phase detector: It sets the common phase between the ref cavity signal and the IPBPMs signals by means of a knob. Then, it separates the IPBPMs signals in two set of orthogonal components by downmixing the signals at 0° , 90° , 45° and 135° . The outputs at 0° and 90° are amplified by 25 to 30 dB, and the 45° and 135° outputs by extra 10 dB according to the module used. One of the two orthogonal sets is read out as In-phase (I) and Quadrature-phase (Q).

At the moment only one Limiter detector is available, therefore, acquisition of only four signals was possible. Priority was given to the study of the three IPBPMs vertical signals. The horizontal signals were studied only for alignment matters.

The noise floor of the first stage of downmixing has been previously measured to be -95 dBm ($4 \mu\text{V}_{\text{rms}}$). It limits the resolution to 2 to 3 nm (horizontal) and 1 to 2 nm (vertical) at 0.5×10^{10} particles per bunch because of sensitivities shown in Sect. 8.1.1.

The gain and attenuation settings are used to achieve the maximum dynamic range within the acquisition system limits described in Sect. 8.1.4. The dynamic range of the electronics is estimated as follows: at 10 dB attenuation, for 0.4×10^{10} particles and $3.7 \mu\text{C}/\text{nm/nC}$ vertical position sensitivity the signal is $0.75 \mu\text{V}/\text{nm}$. This signal is amplified by a total of 53.7 dB from the first (+20 dB) and second (+43.7 dB) downmixing stages with 10 dB losses estimated from

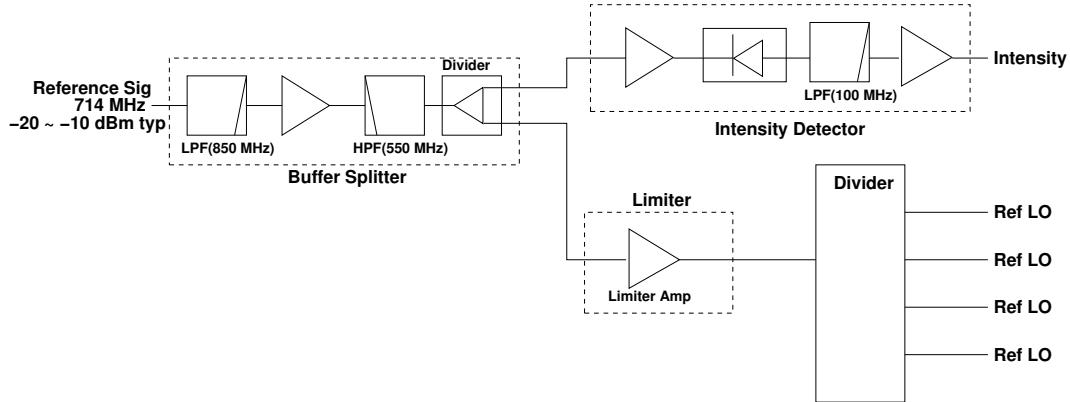


Figure 8.6 – Limiter detector.

cables and couplers. Using +2.5 V as maximum range of acquisition, the signal dynamic range is $6.9 \mu\text{m}$. This can be directly compared with the dynamic range measurement in Sect. 9.2.

However, the typical input value to the first downmixing stage is of -60 dBm ($223.7 \mu\text{V}_{rms}$). It results in a much tighter dynamic range of 300 nm. The estimated input signal to the first downmixing stage and $6.9 \mu\text{m}$ offset is only -33 dB (5 mV_{rms}).

8.1.3 Feedback system

A local beam-based feedback system has been installed at the IP, in order to stabilise the beam position at the IP. This system comprises a stripline kicker, just upstream of the IP chamber, a fast kicker amplifier and digital feedback controller, and can be driven by any of the three IPBPM *IQ* signals, or a linear combination of the signals from any two BPMs. The system is designed for operation within bunch train of two or more bunches, separated by less than 150-200 ns, where the measurement of the first bunch provides the input to the feedback system, and the correction is applied to subsequent bunches.

8.1.4 The acquisition system

The acquisition system samples the two downmixed orthogonal waveforms per cavity per plane over the decay time. This amounts to 14 simultaneous channels: *I* and *Q* waveforms for both *x* and *y* for each of the three position measurement cavities plus the charge signal from each of the two reference cavities.

The resolution required to measure 1 nm over the $10 \mu\text{m}$ of dynamic range is at least 14 bits (2^{14} discrete steps). However, several systems have been used during the course of the IPBPM operation.

Initially a set of four Agilent 3000 X-Series oscilloscopes of 8 bits resolution, four channels each, 5V_{rms} dynamic range and up to 4 Gsamples/s was used for IPBPMs commissioning. Also a dedicated acquisition board, FONT5, operated by FONT group to perform the IP feedback was used. It digitised 9 channels synchronized in banks of three, 13 bits resolution, and a maximum sampling of 400 MHz with $\pm 0.5 \text{ V}$ dynamic range.

A dedicated acquisition system built around a SIS digitizer has recently been introduced. The resolution is 14-bits, the dynamic range is either 2 or 5 V, and the sampling frequency is configurable with 238 MHz being the typical value. This is an important step towards

integration of the IP position measurements into the existing ATF control system because of the gain in dynamic range, higher resolution and assured data availability.

8.2 BPM Analysis Method

The system has been tested with three sets of optics : (1) parallel beam (large beam size at waist and hence approximately constant beam size through the IP region) (2) nominal and (3) low beta.

The longitudinal position of the beam focus was moved closer to the location of IPB, by changing the strength of the FD, to reduce the beam jitter at IPB, allowing operation without additional attenuation and hence maximal sensitivity.

8.2.1 Waveform analysis

The I and Q waveforms are analysed by choosing a single sample point on the signal. In general, the on-peak sample is chosen except in cases where the post analysis shows saturation of the processing electronics. The identification of position and orthogonal components requires a position scan, as explained in Section 8.2.2.

Averaging or integrating the samples may do something to improve the analysis due to the presence of (714 ± 10) MHz band pass filters between the first and second stage of downmixing of the processing electronics as part of an investigation into the reduction of large unwanted static waveform components.

8.2.2 Position scans

While the beam is running the cavity position is systematically changed and the I and Q waveforms are acquired and analysed offline to obtain the signal change to displacement ratio, known as calibration factor.

By definition I' is the position signal and Q' contains all signals orthogonal to position. Figure 8.7 shows that a systematic change in I' signal could change the I and Q values because of a relative phase fixed by the detector in between the reference and the IQ signals. In addition, the mismatch between the BPM dipole frequencies with respect to the reference cavity frequency generates a constant rotation of the I and Q signals which depends on the chosen sample on the waveform.

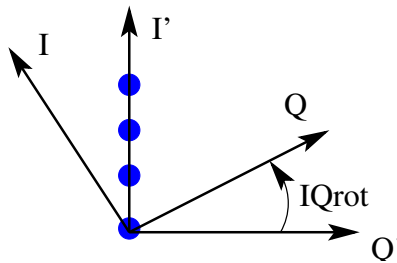


Figure 8.7 – IQ rotation. The blue dots represent the systematic change in position.

The position scan analysis allows to identify I' and Q' by the following procedure:

- Single samples in the waveform for I , Q and Ref signals are chosen.

- The I and Q values per pulse are divided by the Ref value, in order to remove the charge dependence. We have now I_n and Q_n .
- Plotting I_n vs Q_n allows one to find the IQ rotation angle, IQ_{rot} .
- The I_n and Q_n are counter rotated by the IQ_{rot} angle, to determine I' and Q' .

The ratio $I'/\Delta y$ in a.u./ μm is the cavity calibration factor, C_{bpm} .

It also gives the information of the beam center position, $I' = 0$, and the amplitud in μm of the constant orthogonal component Q'/C_{bpm} .

8.2.3 Angle scans

First a position scan should be done to identify I' and Q' signal. Then, a combination of piezo-movers setting keep the cavity center stable and changes the BPM pitch angle in systematic steps while the beam is running. See Appendix B.2.2 for the required mover settings for angle scans.

The I and Q signals are analysed applying the IQ_{rot} angle from the position scan, and it will show the change in I' and Q' while changing the angle. The Q'/θ_p and the calibration factor from the position scan are divided to find the angle to position ratio. It has been measured for IPBy giving $3.2 \mu\text{m}/\text{mrad}$ as expected from cavity parameters [53] (see Section 8.1.1).

8.2.4 Jitter acquisitions

The beam jitter is determined from measurements of the bunch position over several hundred pulses with static BPM mover settings.

Consider now the signal S as the sum of the two outputs from the cavity. The signal S for the vertical outputs of one BPM and one bunch is composed of:

$$S = y + is_p\theta_p + s_{xy}(x + is_y\theta_y) + x\theta_r \quad (8.9)$$

where i represents the $\pi/2$ phase difference, s_p is the sensitivity to pitch angle, s_{xy} is the inverse of X-Y isolation, s_y is the yaw angle sensitivity and $x, y, \theta_p, \theta_r, \theta_y$, are horizontal position, vertical position, pitch, roll and yaw angles of the BPM with respect to beam.

The signal S can be separated in real and imaginary parts:

$$S = (y + s_{xy}x + x\theta_r) + i(s_p\theta_p + s_{xy}s_y\theta_y) \quad (8.10)$$

The amplitude $|S|$ is the total contribution to signal and should be below the dynamic range of the first downmixing stage.

This signals are rotated by an arbitrary angle ϕ to obtain the I' and Q' at the phase shifter block.

$$\begin{aligned} S &= \underbrace{(y + s_{xy}x + x\theta_r)(\cos \phi + i \sin \phi)}_{= I'} + \underbrace{i(s_p\theta_p + s_{xy}s_y\theta_y)(\cos \phi + i \sin \phi)}_{= Q'} \\ &= I' + Q' \end{aligned}$$

In the case of perfect IQ rotation ($\phi = 0$), all the imaginary (angle and others) component is removed from the real (position) component in the S signal. However, in practice this rotation could be achieved to a precision $\Delta\phi$, then, to first order

$$S = [(y + s_{xy}x + x\theta_r) - \Delta\phi(s_p\theta_p + s_{xy}s_y\theta_y)] + i[\Delta\phi(y + s_{xy}x + x\theta_r) + (s_p\theta_p + s_{xy}s_y\theta_y)] \quad (8.11)$$

At this point we will only be interested in the real part as it contains most of the vertical position signal.

$$\Re[S] = S_y = (y + s_{xy}x + x\theta_r) - \Delta\phi(s_p\theta_p + s_{xy}s_y\theta_y) \quad (8.12)$$

The last equation shows the contribution to vertical signal from the relative position of the BPM to the beam.

The mean value of the S_y signal over m bunch samples will be equal to

$$\langle S_y \rangle = [y_0 + (x_0 + \eta\delta)(s_{xy} + \theta_{r0})] - \Delta\phi[s_p\theta_{p0} + s_{xy}s_y(\theta_{y0} + \eta'\delta)] \quad (8.13)$$

where all parameters 0-index correspond to misalignments, η and η' are the spatial dispersion and angular dispersion optical functions, $\delta = 10^{-3}$ is the energy spread, and no beam rotation is considered. The alignment purpose is to make $\langle S \rangle = 0$.

The variance of the signal jitter $\sigma_{S_y}^2 = \langle S_y^2 \rangle - \langle S_y \rangle^2$ can be expressed as

$$\begin{aligned} \sigma_{S_y}^2 &= \sigma_{jy}^2 + \sigma_{jx}^2[s_{xy} + \theta_{r0}]^2 + (\Delta\phi)^2[s_p^2\sigma_{jy'}^2 + s_{xy}^2s_y^2\sigma_{jx'}^2] \\ &= \langle y^2 \rangle - y_0^2 + (\langle x^2 \rangle - x_0^2)[s_{xy} + \theta_{r0}]^2 + (\Delta\phi)^2[s_p^2\langle y'^2 \rangle - y_0'^2 + s_{xy}^2s_y^2(\langle x'^2 \rangle - x_0'^2)] \end{aligned}$$

and subtracting all means effects

$$\sigma_{S_y}^2 = \langle y^2 \rangle + \langle x^2 \rangle[s_{xy} + \theta_{r0}]^2 + (\Delta\phi)^2[s_p^2\langle y'^2 \rangle + s_{xy}^2s_y^2(\langle x'^2 \rangle)] \quad (8.14)$$

Isolation X-Y ($1/s_{xy}$) was measured to be under 50dB, sensitivity to pitch (s_p) was measured to be $3.2\mu\text{m}/\text{mrad}$, and sensitivity to yaw (s_y) is $2.9\mu\text{m}/\text{mrad}$ estimated in similar way as s_p .

For a 1 nm contribution to beam size we get:

$$1 \text{ nm} \geq \sqrt{\langle x^2 \rangle}[s_{xy} + \theta_{r0}] = \sqrt{\langle x^2 \rangle}[1.880 \times 10^{-3} + \theta_{r0}] \quad (8.15)$$

$$1 \text{ nm} \geq \Delta\phi s_p \sqrt{\langle y'^2 \rangle} = 3.2\Delta\phi \sqrt{\langle y'^2 \rangle} \quad (8.16)$$

$$1 \text{ nm} \geq \Delta\phi s_{xy} s_y \sqrt{\langle x'^2 \rangle} = 5.453 \times 10^{-3} \Delta\phi \sqrt{\langle x'^2 \rangle} \quad (8.17)$$

where the BPM vertical ($3.7\text{mV}/\mu\text{m}/\text{nC}$) and horizontal ($2.2\text{mV}/\mu\text{m}/\text{nC}$) sensitivities have been used to translate voltage isolation X-Y to position scale, position jitter is in nm and angle jitter in μrad .

Tables 8.3-8.6 show the typical jitter magnitude at the beam waist and the farthest BPM (IPA) for the two optics with the largest angular jitter.

Using the above jitter magnitudes at the beam waist for the 10BX1BY optics, one can calculate that $\theta_{r0} \leq 0.6 \text{ mrad}$ and $|\Delta\phi| \leq 4.525 \text{ mrad}$ are required to 1 nm resolution.

The current precision of $|\Delta\phi|$ has been found to be 43 mrad by redoing 7 calibrations one after another. This is 10 times bigger than specified and could contribute to 3 to 4 nm to the position jitter at the IP because it adds up in quadrature.

Jitter	10%	20%
$\sigma_{yj}(\text{nm})$	3	7
$\sigma_{xj}(\text{nm})$	283	565
$\sigma_{y'j}(\mu\text{rad})$	34	69
$\sigma_{x'j}(\mu\text{rad})$	71	141

Table 8.3 – Jitter at beam waist with 1BX1BY optics.

Jitter	10%	20%
σ_{yj} (nm)	3	7
σ_{xj} (nm)	894	1787
$\sigma_{y'j}$ (μ rad)	34	69
$\sigma_{x'j}$ (μ rad)	22	44

Table 8.4 – Jitter at beam waist with 10BX1BY optics.

Jitter	10%	20%
σ_{yj} (nm)	5766	11531
σ_{xj} (nm)	11866	23733
$\sigma_{y'j}$ (μ rad)	0	0
$\sigma_{x'j}$ (μ rad)	1	3

Table 8.5 – Jitter at IP with 1BX1BY optics.

Jitter	10%	20%
σ_{yj} (nm)	5766	11531
σ_{xj} (nm)	3856	7713
$\sigma_{y'j}$ (μ rad)	0	0
$\sigma_{x'j}$ (μ rad)	5	10

Table 8.6 – Jitter at IPA with 10BX1BY optics.

Chapter 9

System characterization and Preliminary Results

In this chapter I present the results of the studies in the vertical plane of the piezo-movers calibration factor per block, the BPM signal calibration per BPM and the dynamic range measurement for the IPB system. The resolution is estimated by the analysis of the electronics noise limit and the beam trajectory reconstruction from jitter acquisitions. The system is also used to test feedback in one BPM.

Finally the status of the BPM system is shown with remarks about the ongoing work to improve the current performance.

9.1 Calibration

The calibration factor is obtained per cavity and in the vertical plane y by measuring the position signal change as a function of the physical displacement of the cavity. Two factors are used to obtain each calibration : the movers' displacement versus voltage setting C_m [$\mu\text{m}/\text{V}$] and the cavity response versus voltage setting C_c [a.u./V]. Therefore the cavity calibration factor is $C_{bpm} = C_c/C_m$ [a.u./ μm].

9.1.1 Movers' Calibrations C_m

Prior to installation, the movers' displacement versus voltage setting was measured per BPM block. An interferometer with better than 1 nm resolution was used to measure the BPM vertical position as shown in Fig. 9.1a. As the head is located on top of the BPM, positive displacement implies negative change in the interreferometer readout. Four cycles are shown in Fig. 9.1b, two descending and two rising, covering the total dynamic range and divided in 100 steps, with a 3 s settling time between steps.

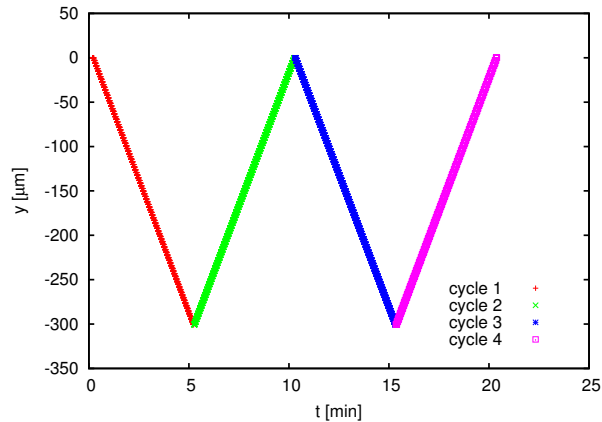
Block AB movers, Cedrat

Linearity was tested in the four cycles with feedback. Fig. 9.2a shows the mover step and Fig. 9.2b shows the residuals from the linear fitting subtraction on each cycle.

The calibration mean from these 4 cycles is $C_{mAB} = (-31.015 \pm 12)\mu\text{m}/\text{V}$. This value is valid for ranges were the residual is constant enough, therefore, it is recommended to use the movers



(a) Picture of SIOS interferometer used to test the movers. Precision is better than 1 nm.



(b) Four cycles are performed over the entire dynamic range of movers.

Figure 9.1 – Movers calibration test setup for the vertical plane.

with voltage settings in the middle of the total dynamic range and to scan over less than 1 V. Improved calibration over full the range can be obtained using a non-linear function.

The step stability was tested by moving back and forth the voltage setting hundreds of times. Figure 9.3a shows that 10 nm steps are observable and Fig. 9.3b shows 1.1 nm of stability on each setting.

Coupling effect of horizontal displacement on the vertical plane was also tested. Figure 9.4 shows a vertical position variation of $2.5 \mu\text{m}$ (1%) over the full horizontal dynamic range.

Only the readbacks from the control box are available after installation indicating current mover position. Results from readback linearity with respect to voltage setting within ranges below 1 V show that readbacks are limited by electrical noise of 0.8 mV limiting the calibration steps. This however does not provide information of the movers stability because the feedback loop is closed inside the control box. The noise is Gaussian, and its effect on

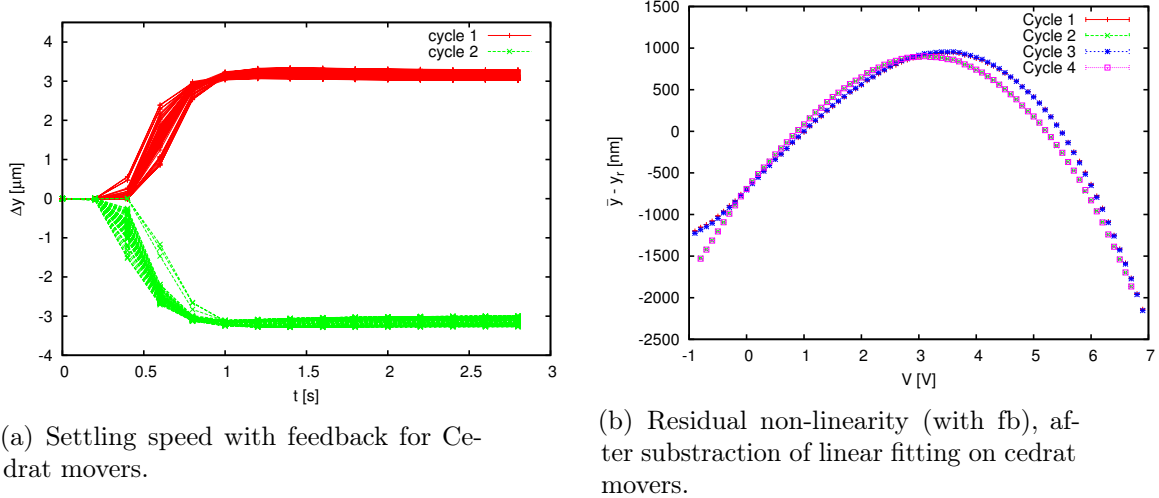


Figure 9.2 – Block AB movers, linearity test over four cycles.

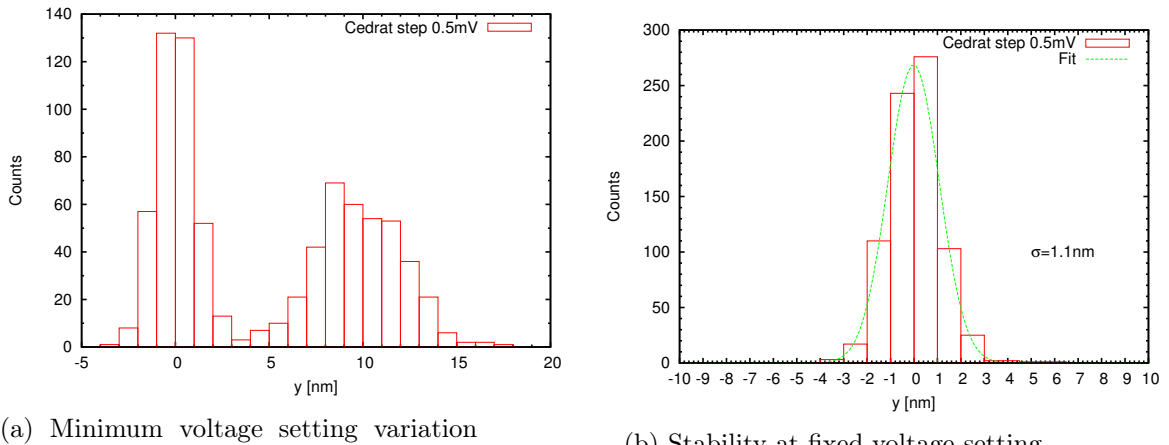


Figure 9.3 – Block AB movers minimum step and stability.

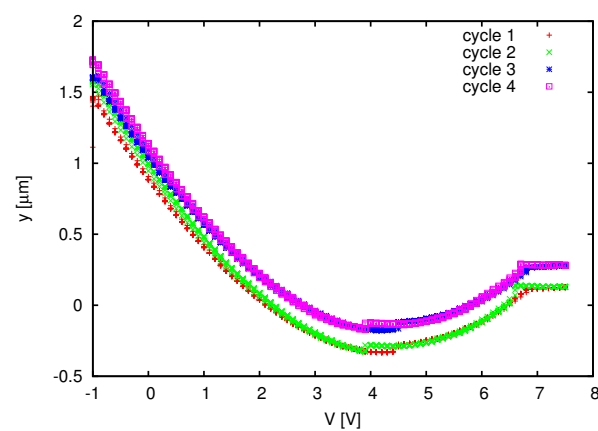
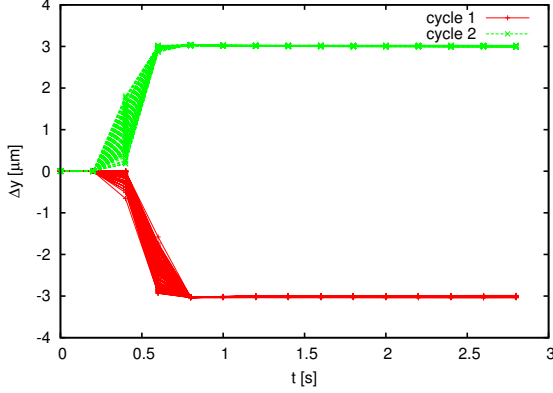


Figure 9.4 – Horizontal to vertical coupling of movers motion.

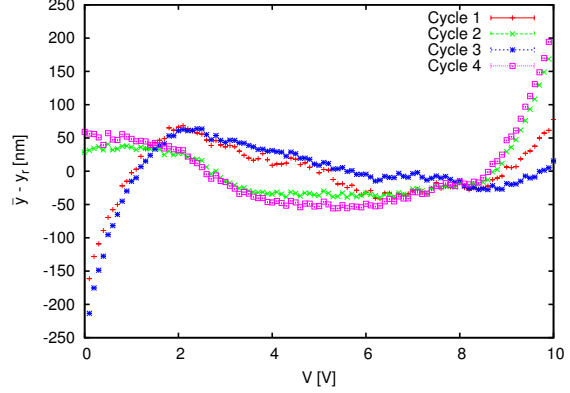
calibration can be minimized by averaging over several readings.

Block C movers, PI

Linearity was tested in the four cycles with feedback. Figure 9.5a shows the settling time of the feedback and Fig. 9.5b shows the residuals from the linear fitting subtraction on each cycle.



(a) Settling speed with feedback for PI movers.

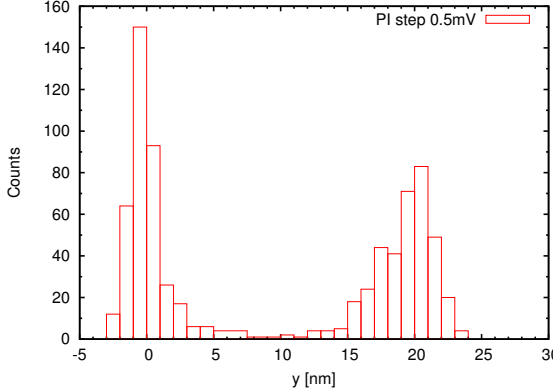


(b) Residual non-linearity (with fb), after subtraction of linear fitting on PI movers.

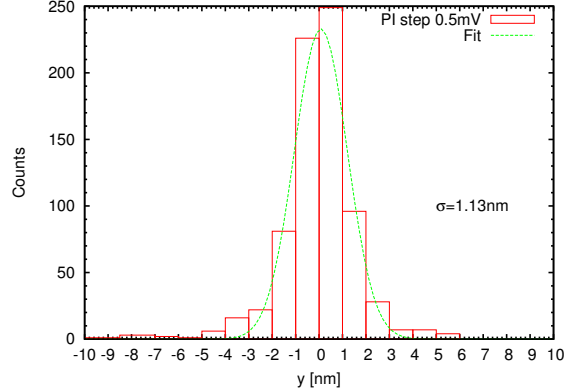
Figure 9.5 – Block C movers, linearity test over four cycles.

The calibration mean from these 4 cycles is $C_{mC} = (30.002 \pm 7)\mu\text{m}/\text{V}$. This value is valid for ranges were the residual is constant enough, therefore, it is recommended to use the movers with voltage settings in the middle of the total dynamic range and/or scan over less than 1 V.

The step stability was tested by moving back and forth the voltage setting hundreds of times. Fig. 9.6a shows that 20 nm steps can be resolved and Fig. 9.6b shows 1.13 nm of stability on each setting with feedback.



(a) Minimum voltage setting variation back and forth tested was 0.5 mV.



(b) Settling speed with feedback for PI movers.

Figure 9.6 – Stability at fixed voltage setting.

Coupling effect of horizontal displacement on the vertical plane was also tested. Fig (9.7) shows vertical position variation of 3 μm (1%) of total horizontal dynamic range.

In the same way as with previous block, only the readbacks from the control box are available after installation indicating current mover position. Results from readback linearity with respect to voltage setting within ranges below 1 V show that readbacks are limited by electrical noise of 5.3 mV limiting the calibration steps. This however does not provide information of the movers stability because the feedback loop is closed inside the control box. The noise is

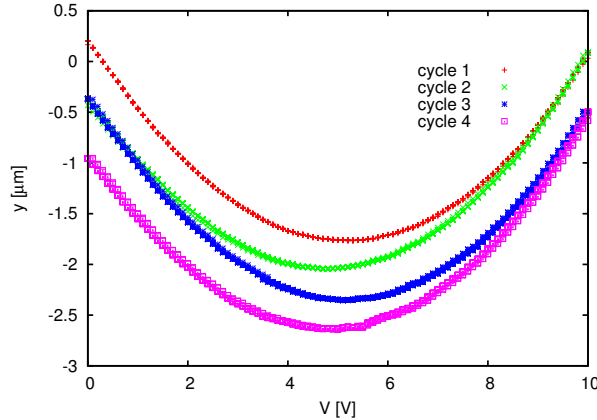


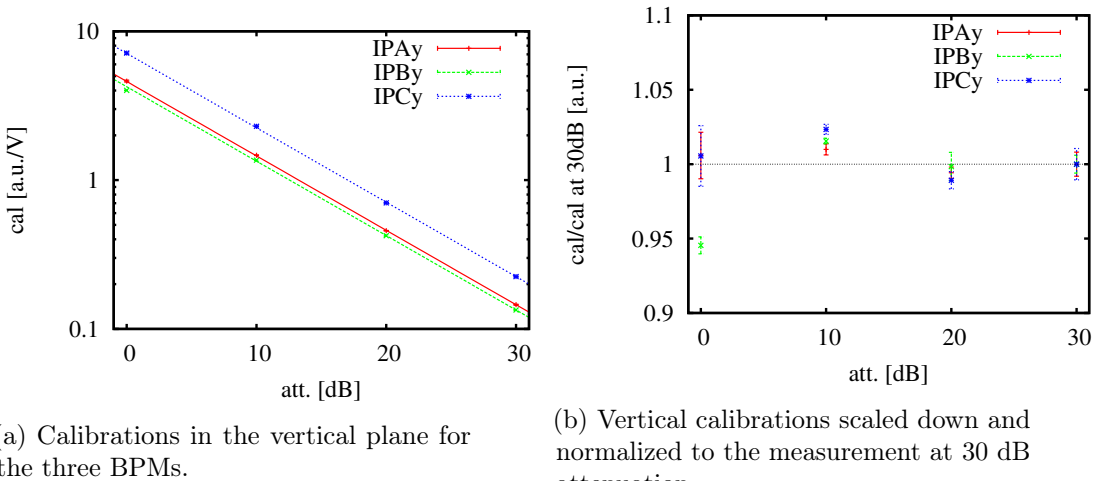
Figure 9.7 – Horizontal to vertical movers coupling.

Gaussian, and its effect on calibration can be minimized by averaging over several readings.

9.1.2 Cavity response calibration C_c

During beam time the cavity position is systematically changed and the amplitude of the cavity output signal is measured. Calibration is calculated from the movers voltage readbacks and choosing the signal peak from the acquired waveform, giving the factor $C_c = I'/V$ [a.u./V], and the IQ rotation angle ϕ .

Input signal can be attenuated from 0 dB to 70 dB in order to keep it inside of the electronics linear response and acquisition system limits. The system response with attenuation change can be seen in Fig. 9.8. The variation of the calibration is within $\pm 5\%$ for charge between $(0.4 \sim 0.5) \times 10^{10}$ particles, except for IPBy at 0 dB. The reason for this is a saturation of the electronics, as explained in Section 9.2.



(a) Calibrations in the vertical plane for the three BPMs.

(b) Vertical calibrations scaled down and normalized to the measurement at 30 dB attenuation.

Figure 9.8 – Calibrations as a function of attenuation.

9.2 Dynamic Range

Dynamic range is defined in this section as the movers' voltage range in which the cavity response is linear within a tolerance, and where it therefore can be translated to position using the calibration factor, c_m , obtained in Sect. 9.1.1. The dynamic range is limited by the linear response of the cavity sensitivity, the processing electronics and the acquisition system.

9.2.1 Acquisition System

Every study case has been performed with signals inside the acquisition system dynamic range, described in 8.1.4. The initial FONT board has been recently replaced by a dedicated SIS digitizer with larger and configurable voltage range. This is no longer a limitation.

9.2.2 Processing electronics and cavity sensitivity

The processing and cavity response are combined in the calibration study showing linearity within $\pm 5\%$ as described in Sect. 9.1.2. However, Fig. 9.8b shows that IPBy calibration is just outside this range at 0 dB attenuation. In order to explain this behaviour the Q' signals from calibrations are shown in Fig. 9.9. A visible difference between IPAy and IPCy with respect to IPBy can be seen. The decay of IPAy and IPCy Q' signals is consistent with system resolution studies shown in Sect. 9.3. However, the IPBy Q' signal remains close to $(0.2 \sim 0.3)$ V of movers voltage in the attenuation range from 0 to 20 dB, equivalent to $(6.2 \sim 9.3)$ μm using C_{mAB} .

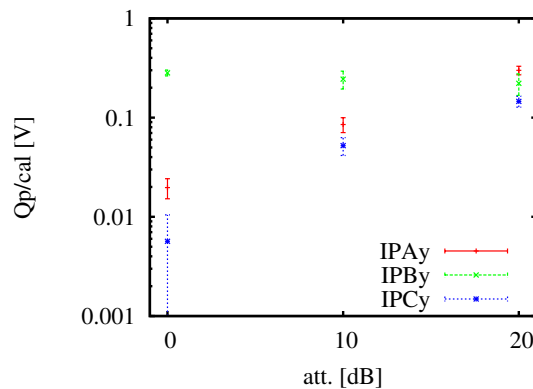


Figure 9.9 – Effect of attenuation in Q' signals from calibrations. Error bars are RMS.

In the same way, the IPBy calibration versus charge is shown in Fig. 9.10, where the calibration values have been normalized to the minimum charge and attenuation is fixed at 10 dB. The calibration constant decays by more than 5% at charges above 0.4×10^{10} particles.

The maximum amplitude of the signal $A = \sqrt{I'^2 + Q'^2}$ has been used to obtain the dynamic range. From the non-saturated calibration at 0.36×10^{10} and 10 dB att. the signals I' and Q' are used to obtain $A = 0.36$ V of movers range, equivalent to 11 μm using c_{mAB} , where the cavity calibration c_B varies less than $\pm 5\%$. Similar dynamic ranges, in the order of 8 to 10 μm , have been found for IPAy and IPCy, however they lack the charge scan.

The IPBy Q' signal fills up almost all dynamic range at 10 dB attenuation and 0.4×10^{10} particles, and it is saturating the processing electronics at 0 dB.

To predict the measured dynamic range of IPBy it is necessary to put extra 6dB of

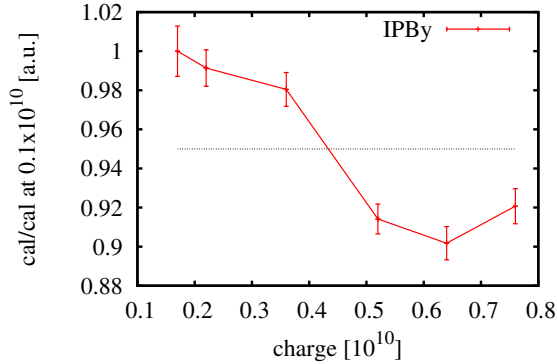


Figure 9.10 – IPBy Calibration versus charge normalized to the calibration at minimum charge.

attenuation in the processing electronics gain model (Sect. 8.1.2) . At the moment, it has been attributed to lower than expected sensitivity of the cavities in Section 9.3.2 and/or cable loss in the processing electronics interconnection.

9.3 Resolution

Resolution is measured in nm using the calibration results from Sect. 9.1. It is limited by the cavity sensitivity, the electronics noise floor and the acquisition system resolution.

9.3.1 Acquisition System

The acquisition system resolution is specified in Sect. 8.1.4. Only the oscilloscopes had lower than required resolution, however, they have already been replaced by a dedicated SIS digitizer. This is no longer a limitation.

9.3.2 Noise floor and cavity sensitivity

The BPMs, processing electronics and connections along the BPM signal path generate noise limiting the minimum detectable waveform. This minimum is estimated by scanning the measured jitter versus the attenuation value.

At large attenuations the noise floor is bigger than beam jitter at the BPM, while at low attenuations is the opposite. There is an inflection point where both are relevant. The cavity calibrations are used to translate the measurements into nm.

The jitter acquisition is the measurement of bunch position over several hundreds of pulses with a fixed BPM position. The readings from the 3 BPMs are shown in Fig. 9.11. Jitter for the three BPMs is in the order of $300 \sim 400$ nm, consistent with true beam jitter at that day (because the beam was not tuned after a DR extraction kicker issue). At 40 dB the noise is larger than beam signal and by extrapolation the resolution limit per BPM is 13 nm for IPAy, 11 nm for IPBy, and 23 nm for IPCy at 0 dB.

It is also clear that IPC shows a worse resolution limit than IPA or IPB. Two possibilities arise: the electronics noise is larger for IPC or the sensitivity is lower.

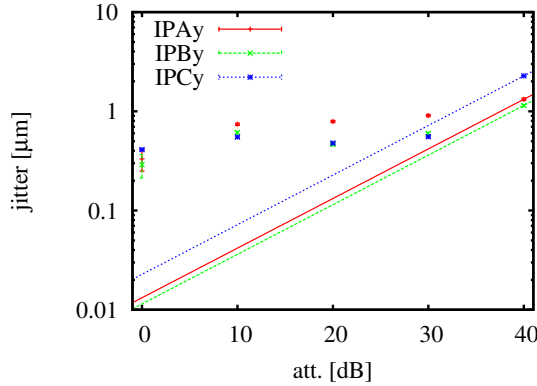


Figure 9.11 – Jitter measurement for the 3 BPMs.

Noise floor

Jitter measurements at 60 dB and 70 dB attenuation with 0.4×10^{10} particles have shown that, after subtraction of known gains from first, second down-mixing stages and hybrid, the noise floor value varies by only ± 1 dB among BPMs.

Although, it can not be considered a direct measurement of the processing noise floor as in [54] because additional losses are not included, it does indicate that the noise floor is similar for the three BPMs and that it is not the explanation for the discrepancy seen in Fig. 9.11 between IPCy when compared to IPAY and IPBy.

A lower limit of 10 nm on the resolution per BPM results from the processing electronics noise floor in the current state.

Cavity sensitivity

Cavity sensitivity and processing electronics gain change the calibration factors. Due to the 6 dB mismatch between the dynamic range measured and predicted for IPBy, as shown in Sect. 9.2, and the lack of charge scans for IPAY and IPCy, it is not possible to conclude about the total gain without making assumptions.

However, the signal decay time from waveforms gives information about the cavity performance. The measurement of the decay time τ described in Sect. 8.1.1 shows a 6 ns decay for IPCy compared to 11 ns and 12 ns for IPAY and IPCy. This difference indicates power losses which might be attributed to partially tightened bolts during mechanical assembly of the BPM. In addition, 11 ns is short when compared with expected 17 ns from design. The effect on cavity sensitivity is still under investigation.

The electronics gain needs to be measured per component and losses need to be identified in order to conclude whether the noise limit comes from processing electronics or the reduced cavity power.

9.3.3 Resolution by trajectory reconstruction

The system resolution could be estimated by the reconstruction of beam trajectories. Two BPMs are used to measure the bunch position and to predict the measurement at the third BPM. The residuals difference between prediction and measurement will depend on each BPM resolution.

Large β^* optics has been used to obtain similar beam jitter and dynamic range in the study of the three BPMs at the same time.

Geometrical method

As longitudinal distances are known within a ± 0.1 mm over 250 mm, i.e. better than 0.1% precision, then, geometrical factors can be used to predict the beam trajectory [55], assuming that all three BPMs have the same resolution. The advantage of this method is that it is independent from beam optics as it does not require to fit parameters to do predictions. The following is an explanation of the method.

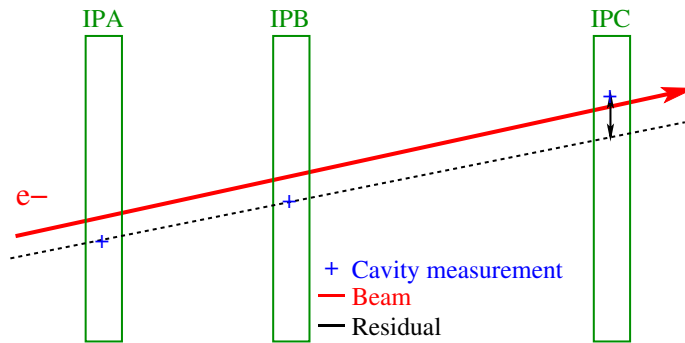


Figure 9.12 – Three BPM resolution. The position measurement at IPA and IPB are used to extrapolate to IPC. The residual from subtraction of the measured and extrapolated position at IPC is used to estimate the system resolution.

Being $f_C(y_A, y_B)$ the prediction at IPC from the measurement at IPA and IPB using the relative distances between the BPMs as in Fig. 9.12, its evaluation is subtracted from the measurement in IPC as in Eq. (9.1). It would be possible to calculate the theoretical propagation of uncertainty of the residual, $\sqrt{\langle R_t \rangle}$, as in Eq. (9.2), from the individual resolutions r_A, r_B , and r_c if they were known.

$$R_t = y_C - f_C(y_A, y_B) \quad (9.1)$$

$$\sqrt{\langle R_t^2 \rangle} = \sqrt{\left(\frac{\partial R_t}{\partial y_A}\right)^2 r_A^2 + \left(\frac{\partial R_t}{\partial y_B}\right)^2 r_B^2 + \left(\frac{\partial R_t}{\partial y_C}\right)^2 r_C^2} \quad (9.2)$$

Assuming that each BPMs position measurement is independent and Gaussian distributed, the standard deviation of the residuals distribution σ_{Rm} from measurements should be equal to the theoretical value $\sqrt{\langle R_t^2 \rangle}$. Equation (9.4) becomes Eq. (9.5) by assuming that each BPM has the same resolution $r_A = r_B = r_C = r$. The factor in the square root in Eq. (9.5) does no longer contain any unknowns, as R_t is a linear extrapolation using distances, and it will be a constant, g , multiplying the standard deviation from measurements to estimate the BPM resolution r . This constant is known as the *geometrical factor*.

$$\frac{\sigma_{Rm}}{\sqrt{\langle R_t^2 \rangle}} = 1 \quad (9.3)$$

$$\frac{\sigma_{Rm}}{\sqrt{\left(\frac{\partial R_t}{\partial y_A}\right)^2 r_A^2 + \left(\frac{\partial R_t}{\partial y_B}\right)^2 r_B^2 + \left(\frac{\partial R_t}{\partial y_C}\right)^2 r_C^2}} = 1 \quad (9.4)$$

$$\frac{\sigma_{Rm}}{\sqrt{\left(\frac{\partial R_t}{\partial y_A}\right)^2 + \left(\frac{\partial R_t}{\partial y_B}\right)^2 + \left(\frac{\partial R_t}{\partial y_C}\right)^2}} = r \quad (9.5)$$

$$g\sigma_{Rm} = r \quad (9.6)$$

The equations used for position prediction are shown in Eq. (9.7), where the coefficients are calculated from the longitudinal distance among BPMs.

$$\begin{aligned} f_A(y_B, y_C) &= 1.463y_B - 0.463y_C \\ f_B(y_A, y_C) &= 0.683y_A + 0.317y_C \\ f_C(y_A, y_B) &= -2.156y_A + 3.156y_B \end{aligned} \quad (9.7)$$

Following the same example with IPC, it is possible to plot the measured value versus the prediction to find the slope and correlation. Ideally, both, slope and correlation are one, however they are resolution limited.

Being C_m the measured value at IPC, C_p the predicted value at IPC from the measurement in other cavities, and $R = C_m - C_p$ the residual from subtraction, it is possible to obtain the slope, m , as in Eq. (9.8). The factor $\langle C_m \cdot R \rangle$ indicates the over or under prediction of the measurement at IPC.

$$m = 1 - \frac{\langle C_m \cdot R \rangle}{\langle C_m^2 \rangle} \quad (9.8)$$

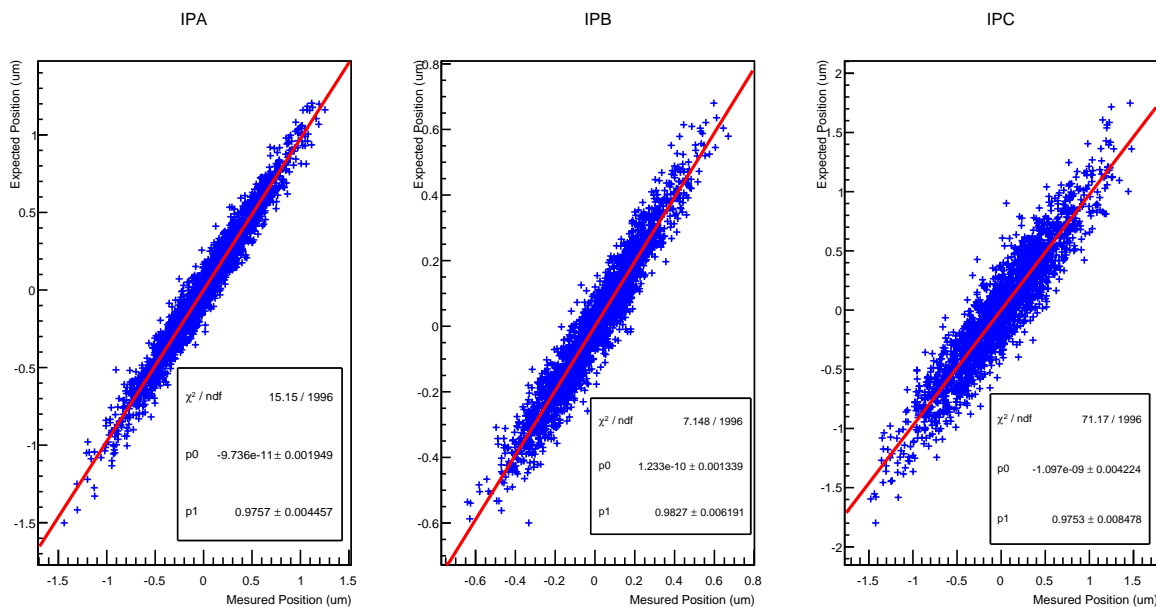


Figure 9.13 – Correlation of the three BPMs measurements and predictions.

Figure 9.13 shows the correlation between the measured and predicted position at 4×10^{10} particles per bunch and 0 dB attenuation, where calibration has been modified by +3.7%, +10.9% and -2.8% for IPAy, IPBy and IPCy respectively in order to obtain unitary slopes within 2%.

The large correction made in the IPBy calibration could be explained by the results shown in Sect. 9.1.2, and the others lay within calibration precision limits.

The measured jitter and the residuals from subtracting the predicted value are gaussian. The jitter values, slopes and correlations of predicted vs measured positions, and geometrical factors are shown in Table 9.1.

The resolution per BPM estimated with this method by calculating the residuals on each one of the three BPMs is (47.4 ± 0.8) nm.

Parameter	IPAy	IPBy	IPCy
Jitter [μm]	0.437	0.216	0.498
Slope	0.9757 ± 0.0044	0.9827 ± 0.0062	0.9753 ± 0.0085
Correlation	0.9798	0.9626	0.9322
Geometrical factor	0.5457	0.7988	0.2531
R [nm]	87.2 ± 1.4	59.7 ± 1.0	185.3 ± 2.9
Resolution [nm]	47.6 ± 0.8	47.7 ± 0.8	46.9 ± 0.7

Table 9.1 – Results from trajectory reconstruction.

9.4 Feedback

During recent tests, a two bunch beam train was used with a bunch spacing of 215.6 ns, and the signals from IPBy were input to the feedback system. Feedback has been tested by the FONT Group [56] obtaining a reduction of beam jitter down to 67 nm, compatible with the resolution shown in Section 9.3.

9.5 Present Status and Prospects

Table (9.2) show a summary of the current IP-BPM results.

The efforts to improve over the results listed above are continuous. Precisely now, two improvements have been done on the system. First, the horizontal and vertical planes can be analyzed simultaneously, such that data can be checked for coupling from one plane to another. Second, filters are added to the system in order to reduce the effect of the mismatch between frequencies in the down-mixing process.

At the moment, the first limitation to improve the resolution is the noise limit. The target is to explore the origin of the noise and characterize the gain along the signal path. That will allow to conclude on the cavity sensitivity.

The IPBy Q' signal is a second limitation to avoid saturation and inaccurate calibration. The reason is unknown for the moment, but it could be generated by an angular misalignment between cavities or a large static monopole signal. I think the monopole would affect also the horizontal plane too, therefore the upgraded electronics will help to diagnose this aspect.

In all cases, the electronics needs to be upgraded because it saturates at half the bunch charge

PARAMETER	REQUIREMENT	STATUS	Comments
Resolution	$\sim \text{nm} @ 1 \times 10^{10}$	$< 50 \text{ nm} @ 0.4 \sim 0.5 \times 10^{10}$	Calibration factors within 5% linearity BPM/Electronics noise : 10 nm per cavity IPC sensitivity and/or gain : $\pm 20 \text{ nm}$ X to Y coupling is still unexplored
Dynamic Range	$\sim 10 \mu\text{m} + \text{extra} @ 0 \text{ dB att.}$	$9 \sim 11 \mu\text{m} @ 10 \text{ dB att.}$	Cavity response is linear within 5% Electronics starts to saturate at $0.4 \times 10^{10} @ 10 \text{ dB att.}$ IPBy Q' signal saturates at 0 dB
Compatibility	IPBSM, EPICS	In progress	Calibration Software : Initial version released and in use. Requires comparison with offline results. Jitter analysis Software : Initial version released and in use. Requires comparison with offline analysis. IP-BSM, requires study of resolution vs low charge, $0.1 \sim 0.5 \times 10^{10}$
Feedback	Operative	Tested	Jitter reduction to 67 nm. Limited by BPM resolution.

Table 9.2 – IPBPMs status.

required. Extra dynamic range in electronics for residual Q' signals would solve the problem.

Under current conditions the characterization of the resolution at low charges is possible, if data are synchronized with the IP-BSM system, then it will provide useful information when tuning the beam size at the IP, leading to finally including the IPBPM as a regular measurement instrument.

Part IV

Conclusions, Results and Perspectives

Conclusions, Results and Perspectives

In order to achieve design luminosities, linear colliders feature nanometer IP beam spot sizes. The CLIC and ILC lattices have been designed using the local or non-local chromaticity correction schemes. A new chromaticity correction scheme has been proposed to the local and non-local chromaticity corrections for CLIC. This lattice has been design and diagnose. The main issue in the current state is the non-zero second order dispersion in the FD region where a strong sextupole is used to correct the remaining geometrical components. It could be solved by cancelling the second order dispersion and its derivative before the FD.

Radiation effects are crucial during the design stage of the lattices, where effects can be evaluated by tracking particles through the lattice or by analytical approximations. In order to include both, radiation and optic parameters, during the design optimization process, radiation phenomena is reviewed. This document addressed two particular radiation phenomena: the Oide effect [24] and the radiation caused by bending magnets [20].

In the Oide effect, radiation in the final quadrupole sets a limit on the vertical beamsize. Only for CLIC 3 TeV this limit is significant, therefore two possibilities have been explored to mitigate its contribution to beam size: double the length and reduce the QD0 gradient, or the integration of a pair of octupoles before and after QD0.

The best result with octupoles demonstrated vertical beam size reduction of $(4.3 \pm 0.2)\%$, with little or negative impact on luminosity. The correction scheme is currently limited by the phase advance and β_y/β_x ratio between correctors. It may be possible to improve its performance by slicing QD0.

The radiation in bending magnets has been reviewed. The analytical result in [20] was generalized to the case with non-zero alpha at the IP and non-zero dispersion, required during the desing and luminosity optimization process. The closed solution for one dipole and one dipole with a drift was compared with the tracking code PLACET [21] resulting in the improvement of the tracking code results. Finally the model validity for the FFS design is analyzed concluding an agreement within $\pm 10\%$ between the theoretical contribution to beam size and the tracking.

ATF serves as R&D platform for the requirements of linear accelerators, in particular ILC. The beam size reduction using the local chromaticity correction is explored by an extension of the original design, called ATF2 with two goals: (**goal 1**) achieve 37 nm of vertical beam size at the IP and (**goal 2**) the stabilization of the IP beam position at the level of few nanometres. Since 2014 beam size of 44 nm are achieved as a regular basis at charges of about 0.1×10^{10} particules per bunch. Possible contributions to beam size are: (1) the increase of the incoming beam emittance along the ATF2 line, (2) systematic errors and resolution limitations on the beam size monitor, (3) beam drift/jitter beyond the tolerable margin and (4) undetected optics mismatch. Last two issues can be adressed by measuring the beam trajectory in the IP Region after the Final Doublet. In addition, looking forward to **goal 2**, beam position measurement is a requirement for beam stabilization.

Therefore, a set of three cavities (IPA, IPB and IPC), two upstream and one downstream of the nominal IP, were installed and are used to measure the beam trajectory in the IP region, thus providing enough information to reconstruct the bunch position and angle at the IP.

The results of the studies in the vertical plane of the cavities calibration show linearity within 5% over two orders of magnitude of signal attenuation. The minimum resolution achieved is just below 50 nm at 0.4×10^{10} particules per bunch with a set of electronics imposing a noise limit on resolution of 10 nm per cavity. The dynamic range is $10 \mu\text{m}$ at 10 dB attenuation and 0.4×10^{10} particules per bunch, indicating the need to upgrade the electronics. The integration to the ATF tuning instruments is ongoing. Nonetheless, feedback has been tested resulting in reduction of beam jitter down to 67 nm, compatible with resolution.

These results are for the moment far from the required specifications with nominal optics of 1 nm resolution over $10 \mu\text{m}$ dynamic range at 1.0×10^{10} particules per bunch. Two improvements have been done on the system since this study. First, the horizontal and vertical planes can be analyzed simultaneously, such that data can be checked for coupling from one plane to another. Second, filters are added to the system in order to reduce the effect of the mismatch between frequencies in the down-mixing process.

Appendix A

The primitive \mathcal{F}

$$\begin{aligned}
\mathcal{F} = & \frac{1}{1209600.0} \{ 1323 \cos(5\sqrt{k}L) - 675 \cos(7\sqrt{k}L) \\
& + \sqrt{k}L(378000 \sin(\sqrt{k}L) + 21000 \sin(3\sqrt{k}L) - 7560 \sin(5\sqrt{k}L)) \\
& + \sqrt{k}l^*[23625 \sin(\sqrt{k}L) + 4725 \sin(3\sqrt{k}L) - 14175 \sin(5\sqrt{k}L) + 4725 \sin(7\sqrt{k}L) \\
& + \sqrt{k}L(-37800 \cos(5\sqrt{k}L)) \\
& + (\sqrt{k}L)^2(-75600 \sin(3\sqrt{k}L) + 226800 \sin(\sqrt{k}L))] \\
& + (\sqrt{k}l^*)^2[-49707 \cos(5\sqrt{k}L) + 14175 \cos(7\sqrt{k}L) \\
& + \sqrt{k}L(1587600 \sin(\sqrt{k}L) - 172200 \sin(3\sqrt{k}L) + 68040 \sin(5\sqrt{k}L))] \\
& + (\sqrt{k}l^*)^3[-80325 \sin(\sqrt{k}L) - 144725 \sin(3\sqrt{k}L) + 82215 \sin(5\sqrt{k}L) - 23625 \sin(7\sqrt{k}L) \\
& + \sqrt{k}L(37800 \cos(5\sqrt{k}L)) \\
& + (\sqrt{k}L)^2(680400 \sin(\sqrt{k}L) - 126000 \sin(3\sqrt{k}L))] \\
& + (\sqrt{k}l^*)^4[68985 \cos(5\sqrt{k}L) - 23625 \cos(\sqrt{k}L) \\
& + \sqrt{k}L(2041200 \sin(\sqrt{k}L) - 205800 \sin(3\sqrt{k}L) + 37800 \sin(5\sqrt{k}L))] \\
& + (\sqrt{k}l^*)^5[-458325 \sin(\sqrt{k}L) - 43225 \sin(3\sqrt{k}L) - 25893 \sin(5\sqrt{k}L) + 14175 \sin(7\sqrt{k}L) \\
& + \sqrt{k}L(68040 \cos(5\sqrt{k}L)) \\
& + (\sqrt{k}L)^2(680400 \sin(\sqrt{k}L) - 25200 \sin(3\sqrt{k}L))] \\
& + (\sqrt{k}l^*)^6[-945 \cos(5\sqrt{k}L) + 4725 \cos(7\sqrt{k}L) \\
& + \sqrt{k}L(831600 \sin(\sqrt{k}L) - 12600 \sin(3\sqrt{k}L) - 37800 \sin(5\sqrt{k}L))] \\
& + (\sqrt{k}l^*)^7[(-354375) \sin(\sqrt{k}L) + 5425 \sin(3\sqrt{k}L) - 1323 \sin(5\sqrt{k}L) - 675 \sin(7\sqrt{k}L) \\
& + \sqrt{k}L(-7560 \cos(5\sqrt{k}L)) \\
& + (\sqrt{k}L)^2(226800 \sin(\sqrt{k}L) + 25200 \sin(3\sqrt{k}L))] \\
& + \cos(\sqrt{k}L)((\sqrt{k}l^*)^2 + 1)(4725)[(\sqrt{k}l^*)^5(\sqrt{k}L)(80) \\
& + (\sqrt{k}l^*)^4(155 - 48(\sqrt{k}L)^2) \\
& + (\sqrt{k}l^*)^3(\sqrt{k}L)(64) \\
& + (\sqrt{k}l^*)^2(182 - 96(\sqrt{k}L)^2) \\
& + \sqrt{k}l^*(-16\sqrt{k}L) \\
& + (\sqrt{k}L)^2(-48) + 75] \\
& + \cos(3\sqrt{k}L)(-175)[(\sqrt{k}l^*)^7(\sqrt{k}L)(120) \\
& + (\sqrt{k}l^*)^6(3)(144(\sqrt{k}L)^2 + 71) \\
& + (\sqrt{k}l^*)^5(\sqrt{k}L)(744) \\
& + (\sqrt{k}l^*)^4(720(\sqrt{k}L)^2 + 347) \\
& + (\sqrt{k}l^*)^3(\sqrt{k}L)(-24) \\
& + (\sqrt{k}l^*)^2(144(\sqrt{k}L)^2 - 473) \\
& + \sqrt{k}l^*(-648)\sqrt{k}L \\
& + (\sqrt{k}L)^2(-144) - 31]\}
\end{aligned}$$

In order to confirm that the code implementation gave the same result than the original double integral, random values were assigned to $\sqrt{k}l^*$ and $\sqrt{k}L$ and both expressions, the solved and the double integral, were numerically evaluated with difference lower than 10^{-3} relative.

Appendix B

IPBPMs Movers

B.1 System Description

At the ATF2 IP, inside the vacuum chamber, the BPMs positioning system has been installed during the first two weeks of July 2013. It moves two independent blocks: Block IPAB and Block IPC. Each block has three degrees of freedom: vertical, lateral and pitch angle, by using 4 piezo-movers: three vertical and one horizontal.

Movers made by the german company “PI” electronics moves IPC and the french company “Cedrat Technologies” moves IPAB.

B.1.1 The Piezo Movers

Piezo mover changes its position as a function of voltage. Each one of the eight movers has its own control electronics block composed of:

- the mover
- the strain gauge
- the control box (manufacturer module) to:
 - set piezo mover voltage (high voltage)
 - * PI module E-621
 - * CEDRAT module LA75
 - read strain gauge
 - * PI module E-621 (same as control)
 - * CEDRAT module SG75
 - set feedback operation (ON/OFF)
 - set control mode (external control, PLC is used for setpoint setting)
- PLC channel to
 - set voltage to displace the mover
 - read voltage to determine mover position (with FB ON, read voltage approaches the set voltage.)

B.1.2 Electrical connections

Figure B.1 shows the connections diagram of electrical connections between the movers displacement system. It shows the connexion to the local network by Ethernet, the DACs and ADCs used to set and read the voltage levels, the connection to the dedicated control boxes, a linking box to match the cable conexions, the 25 m cable to connect to the vacuum chamber flanges, the movers, and temperature probes.

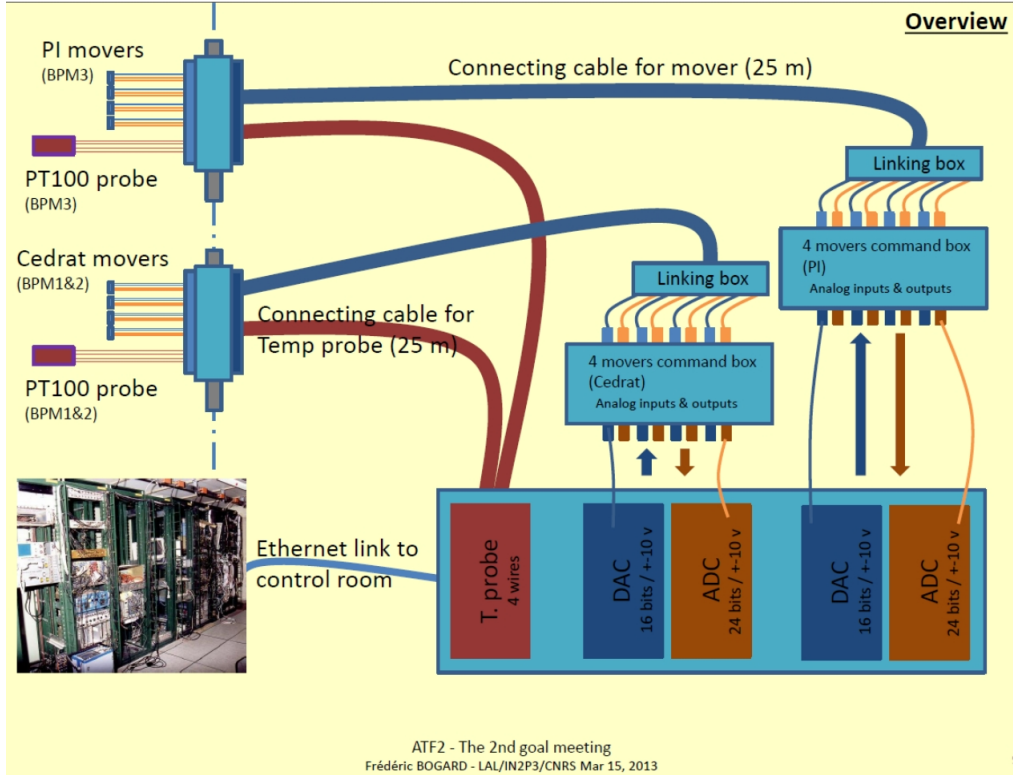


Figure B.1 – Piezo mover system connection diagram.

Mover range

PI and Cedrat have different ranges: PI (300 um), Cedrat (250 um). The Control voltage and displacement (min-max) is opposite between companies:

- PI: (min) 0V to (max) 10V
- CEDRAT: (max) -1V to (min) 7V

It is important to note that:

- The voltage-displacement relation is inverse for CEDRAT movers.
- When the system is OFF (0V), PI mover are at its minimum, however CEDRAT are not.

Mover Control

Figure B.2 shows an schematic of the control system per mover. The voltage value is set via an EPICS Process Variable (PV), and it is send to a DAC, the analog voltage set the control box

to move the piezo-electric. The displacement is measured by a set of strain-gauges. The FB loop is closed at the Control box. A read-out voltage is taken by the ADC and published as another PV.

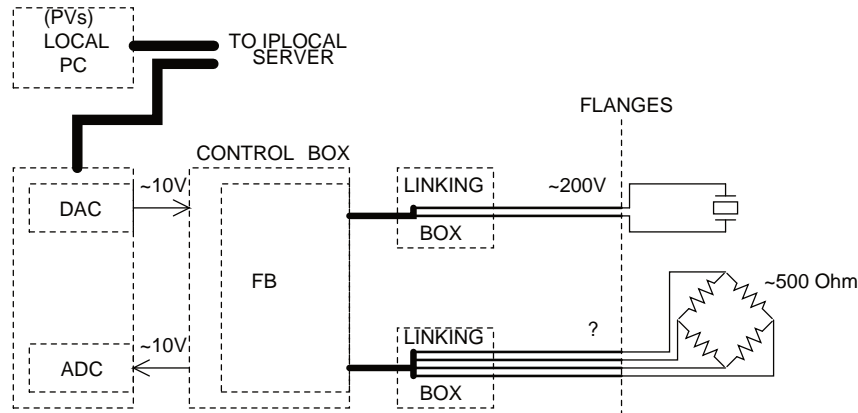


Figure B.2 – Control system per mover.

BLOCK AB 1 mV=31.25 nm, BLOCK C 1 mV=30 nm

Feedback and NO Feedback

There are two operation possibilities per mover: Feedback (fb) and No Feedback (no fb). It means 8 feedback loops. On each case the control module sets a voltage value on the mover and read the strain gauge to create a closed loop. However, their implementations are different on each company.

B.1.3 The PLC

Two NI9263 are used to set analogue voltage into the mover control electronics. Two NI9239 are used to read analogue voltage from the strain gauge readback. One NI9219 is used to read temperature. These modules are connected to the chassis NI9188 which is connected by network to a working station with Labview installed. The block chassis+NI modules is called **PLC**.

National instruments Chassis: NI9188

- Mac Address: 0080.2f14.b777
- DHCP
- IP address (ATF) 31.1.1.39
- IP address (KEK): None
- Host name: ipmv-plc.ip-local
- Net Mask: 255.255.255.0
- connected to ip-local during installation

Chassis NI9188 can connect up to 8 modules, not all are used:

- PI
 - Module 5: NI9263 Digital to analogue converter
 - Module 6: NI9239 Analogue to digital converter
- Cedrat
 - Module 2: NI9263 Digital to analogue converter
 - Module 3: NI9239 Analogue to digital converter
- Temperature
 - Module 8: NI9219 Temperature probes
 - * Cedrat: Channel 0
 - * PI: Channel 2
- The other slots are not used

B.1.4 The PC

It is used to control from close locations the BPM positioning system. It sets the digital values to put in the PLC and reads the digital values from the PLC channels corresponding to strain gauges.

Characteristics

LAL Computer (Laptop) Processor Inter Core i7 vPro

Mac Address: d067.e550.620e

Network Parameters

DHCP

IP address(ATF): (31.1.1.38) ipmover-pc.ip-local

Net Mask: 255.255.255.0

Connected to ip-local server

Used Software

Windows 7 Fran ais

National Instrument - Labview 2011

National Instruments - Measurement & Automation Explorer (NI MAX) 5.4

Evince 2.32.0

CALab (Labview + EPICS) [57]

In adition, this Software is present but not used by movers:

SIOS Interferometer Software INFASNTC 6.3.1.42 2012

Festo Positioning Drivers

Access

Account (Nom d'utilisateur): *****

Password: KEKJapan2012

Folder Content Description

Path to applications and info

Bureau/Actionneurs Piezo/Applis

All applications were done in Labview. Filenames gives a hint of its content (keywords used in filenames):

- **oscilloscope**: uses de ADC to read signals
- **generateur**: function generator, uses de DACs to produce signals
- **Actionneurs positionnement BPMs**: activate the system displacement
- **Ethernet**: connected by wired network,
- **USB**: corresponds to previous version connected by USB.
- **Verticaux groupe**: all 3 vertical mover movers are activated by one voltage control
- **mouvements identiques**: first version of BPM displacement system (PI and CEDRAT) integrated.
- **Jauge**: stores the strain gauges info in excel format.
- **temp**: stores temperature info in excel format.
- **epics**: control from epics system, Labview works as interface.
- **Actionneurs multicycles**: several cycles over the defined voltage range are performed
- **Cedrat, PI**: identifies the group of movers to use.
- **Vertical, lateral fixe**: it means that one direction of movement is set (fixed) to a voltage value while the other direction varies in cycles.

PVs

Epics PVs (Process Variables). Write: sets a value on the DAC. Read: reads from ADC.

Channels IP:BPM-AB:Mover0 and IP:BPM-C:MoverB are for lateral movement.

IP:BPM-AB:Mover0:Read

IP:BPM-AB:Mover0:Write

IP:BPM-AB:Mover1:Read

IP:BPM-AB:Mover1:Write

IP:BPM-AB:Mover2:Read

IP:BPM-AB:Mover2:Write
 IP:BPM-AB:Mover3:Read
 IP:BPM-AB:Mover3:Write
 IP:BPM-C:MoverB:Read
 IP:BPM-C:MoverB:Write
 IP:BPM-C:MoverC:Read
 IP:BPM-C:MoverC:Write
 IP:BPM-C:MoverD:Read
 IP:BPM-C:MoverD:Write
 IP:BPM-C:MoverE:Read
 IP:BPM-C:MoverE:Write
 IP:BPM-AB:Temp
 IP:BPM-C:Temp

B.2 The BPMs

B.2.1 Coordinate system

Each BPM has its own coordinates with respect to a reference system centered electrically as in Fig. B.3.

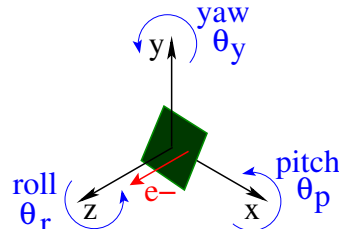


Figure B.3 – BPM coordinate system centered electrically. Beam in red, BPMs in green.

The coordinates of the beam and the BPM angle rotations are given by:

- Beam Position: $x_A, y_A, z_A, x_B, y_B, z_B, x_C, y_C, z_C$
- BPM Angles respect to ref. system: $\theta_{Ap}, \theta_{Ar}, \theta_{Ay}, \theta_{Bp}, \theta_{Br}, \theta_{By}, \theta_{Cp}, \theta_{Cr}, \theta_{Cy}$

All systems relate to a common **mechanical** reference system with no rotations, just translations in Fig. B.4. However, IPB could be chosen to coincide with the common to simplify the description.

There is a set of movers to control BPM position shown in Fig. B.5. This is expressed in Eq. (B.1) where during the installation all initial values (with 0-index) are set. A mover combination can change the transverse positions and the pitch angle per block.

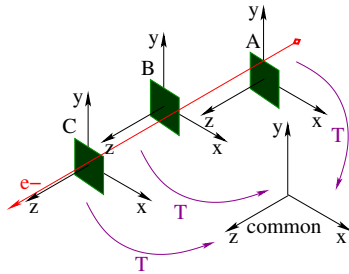
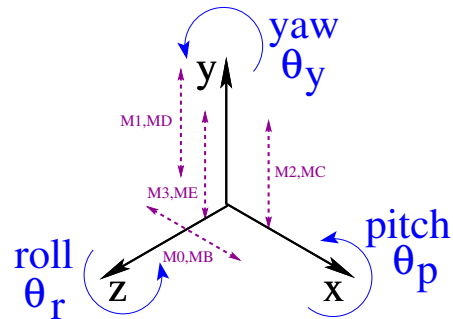


Figure B.4 – Reference system for the 3 BPMs.

Figure B.5 – Set of movers: M_{01234} in Block IPAB and M_{BCDE} in Block IPC.

$$x = x_0 + f_x(M_{0,B}) \quad (B.1)$$

$$y = y_0 + f_y(M_{123,CDE})$$

$$z = z_0$$

$$\theta_p = \theta_{p0} + f_p(M_{123,CDE})$$

$$\theta_r = \theta_{r0}$$

$$\theta_y = \theta_{y0}$$

Figure B.6 shows the location of the movers along the longitudinal direction. This information is used to calculate the alignment correction limits of the system.

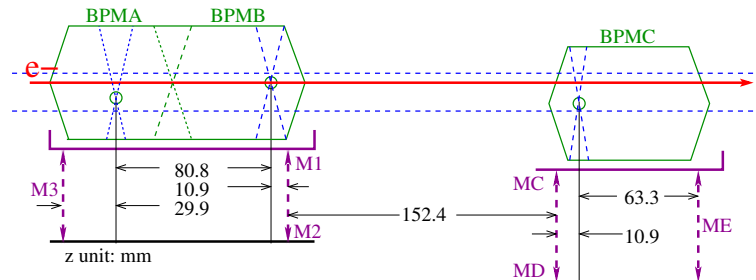


Figure B.6 – Longitudinal position of the movers.

B.2.2 Alignment adjustment

Normalizing the movers range to -1 to 1 units, as in Eq. (B.2), it is possible to calculate the effect of movers displacement on the cavity position shown in Table B.1.

$$M_{0123} = \frac{3 - V_{0123}[\text{V}]}{4} \quad M_{BCDE} = \frac{V_{BCDE}[\text{V}] - 5}{5} \quad (\text{B.2})$$

Block IPAB movers are able to correct a maximum of ± 1 mrad or $\pm 125 \mu\text{m}$, while Block IPC is able to correct ± 2 mrad or $\pm 150 \mu\text{m}$. Correction of IPA and IPB position is not independent, therefore, special effort is put into minimize the offset in the block IPAB.

By making $y = 0$ and $y_0 = 0$ it is also possible to find a set of movers that keeps the vertical position and changes the angle per BPM. This gives the possibility to scan sensitivity to pitch angle.

	Adjustment		
	IPB	IPA	IPC
$x[\mu\text{m}]$	$x_{0B} + 125M_0$	$x_{0A} + 125M_0$	$x_{0C} + 150M_B$
$y[\mu\text{m}]$	$y_{0B} + 11.2M_{1,2} + 113.8M_3$	$y_{0A} + 94.8M_{1,2} + 30.2M_3$	$y_{0C} + 128.0M_{CD} + 22.0M_E$
$z[\text{mm}]$	z_{0B}	$z_{0B} - 80.8$	$z_{0B} + 174.2$
$\theta_p[\text{mrad}]$	$\theta_{p0B} + 1.03(M_3 - M_{1,2})$	$\theta_{p0A} + 1.03(M_3 - M_{1,2})$	$\theta_{p0C} + 2.02(M_{DC} - M_E)$
$\theta_r[\text{mrad}]$	θ_{r0B}	θ_{r0A}	θ_{r0C}
$\theta_y[\text{mrad}]$	θ_{y0B}	θ_{y0A}	θ_{y0C}

Table B.1 – $M_{0123,BCDE} \in [-1, 1]$, $\Delta M_{0123,BCDE} \geq 1.25 \times 10^{-2}$

B.3 Alignment

B.3.1 Vacuum chamber

The goal is the alignment of the vacuum chamber with respect to external references by less than $200 \mu\text{m}$. Below this range, the piezo-electric movers in each cavity block are used to align the cavity with respect to the beam.

The beam positioning system should not interfere with the IPBSM measurements. Therefore, mechanical dimensions and weight should be restricted to those supported by the vertical optical table. This will allow to have a common reference point between the two structures.

B.3.2 Effect of alignment on dynamic range

Dynamic range is reduced by misalignment because of the constant I' and Q' signals from position and angle. This should be minimize aiming to use the minimum dynamic range possible.

However, IPA and IPB are located in a common movers system and therefore BPM position and angle can not be corrected independently. Both BPMs centers can be aligned with the beam by making an angle, but, due the cavity sensitivity to angle of $3.2 \mu\text{m}/\text{mrad}$, the Q' will subtract the dynamic range available for position scans. This adds to the Q' static signal per BPM and therefore it could become critical.

The initial BPM installation [49] had alignment issues attributed to loose tolerances between the inner cavity surface and the external reference points [58]. During 2014, new cavities were

fabricated and installed in the ATF2 line. This set of BPMs has been in use since November 2014.

- Position scans with $I' = 0$. This is fairly simple because it only tries to find the center of the BPM without considering the Q' signal. The issue is that beam angle through the IPBPMs changes and these leads to different alignment results. A typical change of 0.1 mrad in the beam trajectory by a QD0 displacement of 100 μm could change the alignment results by 25 μm from IPA to IPC. Additional $\pm 10 \mu\text{m}$ changes in $I' = 0$ have been seen between samples. Table B.2 shows the horizontal and vertical alignment of the new BPMs taken in separated shifts.
- First, make $I' = 0$ and then use a movers and QF7 combination to make $Q' = 0$. This method is valid for Q' entirely from angle. At the moment it has not been tested with the new BPMs. Table B.3 shows the vertical position results for the previous BPMs.

Plane	IPA	IPB	IPC	Comment
X [μm]	-5	+18	-41	QD0 mover(X)=-70 μm , 10BX1BY optics
Y [μm]	-18	+24	-102	QD0 mover(Y)=160 μm , Low beta optics

Table B.2 – Alignment measurement using $I' = 0$

Vertical	IPA	IPB	IPC
Y [μm]	-7	+79	-
θ_p [mrad]	0.024	1.0	-

Table B.3 – Alignment measurement using $I' = 0$ and $Q' = 0$ for previous BPMs.

B.3.3 Effect of cavity alignment on calibration

After the installation the cavities are fixed in the piezo-movers system. Figure B.7a shows a static angle β between the movers direction and the BPM axis, while the beam makes an angle α with respect to the movers.

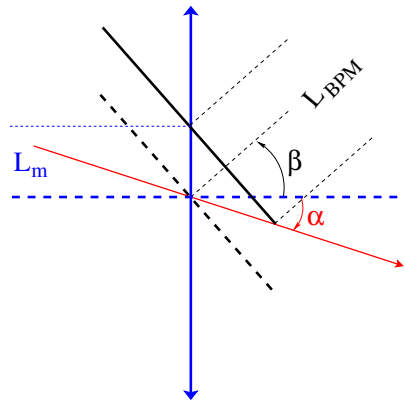
When doing a position scan to get the BPM calibration the BPM is displaced by L_m , however, the displacement seen by the BPM is L_{BPM} . Equation (B.3) shows the effect of the angles in the measured distance and Fig. B.7b shows the combinations of α and β affecting the calibration by less than 10^{-3} and 10^{-4} .

Considering α , the beam divergence is 0.35 mrad in the nominal optics which is very small and do not affect calibration. The angle change by QF7 has been simulated to have an excursion of 3 mrad at IPB per 1 mm of vertical displacement of QF7, this also remains in below the 10^{-4} effect.

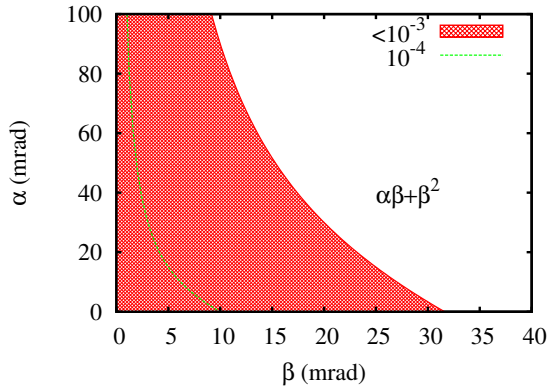
$$\begin{aligned} L_{BPM} &= L_m (\cos \beta + \sin \beta \tan(\alpha + \beta)) \\ &\approx L_m (1 + \alpha \beta + \beta^2) \end{aligned} \quad (\text{B.3})$$

If the movers are used to induce an additional angle γ to the BPMs as in Fig. B.8, then the net effect is and addition of $\beta + \gamma$ shown in Eq. (B.4).

$$L_{BPM} \approx L_m [1 + \alpha(\beta + \gamma) + (\beta + \gamma)^2] \quad (\text{B.4})$$



(a) Displacement from the center. Movers displace by L_m . Cavity sees L_{BPM}



(b) α and β should be inside the dashed area to keep the calibration value within 10^{-3} precision.

The total correction possible for the BPMs is $|\gamma| \leq 1$ mrad. It is also a very small angle. The more restrictive angle is $|\beta| < 5$ mrad.

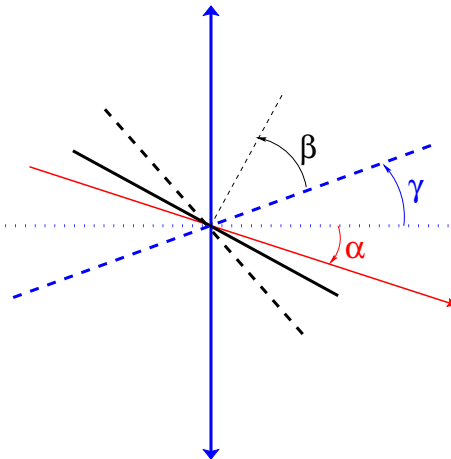


Figure B.8 – γ angle rotation over the BPM. The only effect on distance measured is to add γ to β .

B.3.4 Mechanical BPM alignment

The estimation of mechanical positions resolution is shown in Table B.4.

Axis (Symbol)	Mechanical Precision (μm)
Vertical (Δy)	1
Horizontal (Δx)	5
Longitudinal (Δz)	5

Table B.4 – Position mechanical precision

Bibliography

- [1] The CMS Collaboration. A new boson with a mass of 125 gev observed with the cms experiment at the large hadron collider, *Science*, 338(6114):1569–1575, 2012, DOI: 10.1126/science.1230816, eprint: <http://www.sciencemag.org/content/338/6114/1569.full.pdf> (see p. 17).
- [2] The ATLAS Collaboration. A particle consistent with the higgs boson observed with the atlas detector at the large hadron collider, *Science*, 338(6114):1576–1582, 2012, DOI: 10.1126/science.1232005, eprint: <http://www.sciencemag.org/content/338/6114/1576.full.pdf> (see p. 17).
- [3] R W Assmann, M Lamont, and S Myers. A Brief History of the LEP Collider, *Nucl. phys. b, proc. suppl.*, 109(CERN-SL-2002-009-OP):17–31. 15 p, April 2002 (see p. 18).
- [4] J.P. Delahaye, G. Guignard, T Raubenheimer, and I. Wilson. Scaling laws for e+/e- linear colliders, *Nuclear instrumentation and methods in physics research section a: accelerators, spectrometers, detectors and associated equipment*, 421:369–405, 3, February 1999 (see p. 23).
- [5] *CAS-CERN Accelerator School: 4th General accelerator physics course. Julich, FR Germany*, Proceedings of CAS 91-04, 1990 (see p. 27).
- [6] Hector Garcia Morales, Rogelio Tomas Garcia, and Yuri Kubyshin. Comparative study of Final Focus Systems for CLIC and other luminosity ehancement studies for future linear colliders, Presented 16 Jan 2015, PhD thesis, Barcelona, Polytechnic U., 2014 (see pp. 25, 28, 33).
- [7] Michiko G Minty and Frank Zimmermann. *Measurement and control of charged particle beams*, of *Particle acceleration and detection*, Springer, Berlin, 2003 (see p. 28).
- [8] K. L. Brown. A Conceptual Design of Final Focus Systems for Linear Colliders, *Slac*, 1987 (see p. 25).
- [9] M Aicheler, P Burrows, M Draper, T Garvey, P Lebrun, K Peach, N Phinney, H Schmickler, D Schulte, and N Toge. A Multi-TeV Linear Collider Based on CLIC Technology: CLIC Conceptual Design Report, technical report (CERN-2012-007. SLAC-R-985. KEK-Report-2012-1. PSI-12-01. JAI-2012-001), Geneva: CERN, 2012 (see pp. 34, 52, 53).
- [10] K. L. Brown. Basic Optics of the SLC Final Focus System, *Slac*, 1988 (see p. 27).
- [11] Raimondi P. and Seryi A. A Novel Final Focus Design for Future Linear Colliders. *Slac*, 2000 (see pp. 27, 64).
- [12] Hector Garcia Morales and Rogelio Tomas Garcia. Final-focus systems for multi-tev linear colliders, *Phys. rev. st accel. beams*, 17:101001, 10, October 2014, DOI: 10.1103/PhysRevSTAB.17.101001 (see p. 38).

- [13] G. Xu. General conditions for self-cancellation of geometric aberrations in a lattice structure, *Phys. rev. st accel. beams*, 8:104002, 10, October 2005, DOI: 10.1103/PhysRevSTAB.8.104002 (see pp. 38, 56).
- [14] MAD-X, <http://mad.web.cern.ch/mad/> Link consulted 2015.04.22 (see p. 39).
- [15] *A Recipe for Linear Collider Final Focus System Design*. Proceedings of PAC2003, 2003 (see p. 39).
- [16] R. Tomás. Nonlinear optimization of beam lines, *Phys. rev. st accel. beams*, 9:081001, 8, August 2006, DOI: 10.1103/PhysRevSTAB.9.081001 (see pp. 39, 52).
- [17] R Tomás. MAPCLASS: a code to optimize high order aberrations, technical report (AB-Note-2006-017. CERN-AB-Note-2006-017), CERN, January 2007 (see pp. 39, 52).
- [18] D Martinez, A Rosam, R Tomas, and R De Maria. MAPCLASS2: a code to aid the optimisation of lattice design, *Cern note*, November 2012 (see pp. 39, 52).
- [19] Mapclass2, <https://github.com/pylhc/MapClass2> Link consulted 2014.01.13 (see pp. 39, 52).
- [20] M. Sands. EMITTANCE GROWTH FROM RADIATION FLUCTUATIONS, *Slac pubs and reports*, 1985 (see pp. 43, 44, 97).
- [21] Placet, <https://savannah.cern.ch/projects/placet/> Link consulted 2013.04.17 (see pp. 43, 45, 54, 97).
- [22] M. Sands. The Physics of Electron Storage Rings: An Introduction, *Slac pubs and reports*, 1970 (see p. 43).
- [23] Javier Barranco Garcia, Eduardo Marin Lacoma, and Rogelio Tomas Garcia. Luminosity studies in a traveling waist regime in the compact linear collider, *Phys. rev. st accel. beams*, 16:041001, 4, April 2013, DOI: 10.1103/PhysRevSTAB.16.041001 (see p. 45).
- [24] Katsunobu Oide. Synchrotron-radiation limit on the focusing of electron beams, *Phys. rev. lett.*, 61:1713–1715, 15, October 1988, DOI: 10.1103/PhysRevLett.61.1713 (see pp. 51, 52, 55, 97).
- [25] Chris Adolphsen, Maura Barone, Barry Barish, Karsten Buesser, Philip Burrows, John Carwardine, Jeffrey Clark, Hélène Mainaud Durand, Gerry Dugan, Eckhard Elsen, Atsushi Enomoto, Brian Foster, Shigeki Fukuda, Wei Gai, Martin Gastal, Rongli Geng, Camille Ginsburg, Susanna Guiducci, Mike Harrison, Hitoshi Hayano, Keith Kershaw, Kiyoshi Kubo, Victor Kuchler, Benno List, Wanming Liu, Shinichiro Michizono, Christopher Nantista, John Osborne, Mark Palmer, James McEwan Paterson, Thomas Peterson, Nan Phinney, Paolo Pierini, Marc Ross, David Rubin, Andrei Seryi, John Sheppard, Nikolay Solyak, Steinar Stapnes, Toshiaki Tauchi, Nobu Toge, Nicholas Walker, Akira Yamamoto, and Kaoru Yokoya. The International Linear Collider Technical Design Report - Volume 3.I: Accelerator R&D in the Technical Design Phase, technical report (arXiv:1306.6353. ANL-HEP-TR-13-20. BNL-100603-2013-IR. IRFU-13-59. CERN-ATS-2013-037. Cockcroft-13-10. CLNS-13-2085. DESY-13-062. FERMILAB-TM-2554. IHEP-AC-ILC-2013-001. ILC-REPORT-2013-040. INFN-13-04-LNF. JAI-2013-001. JINR-E9-2013-35. JLAB-R-2013-01. KEK-Report-2013-1. KNU-CHEP-ILC-2013-1. LLNL-TR-635539. SLAC-R-1004. ILC-HiGrade-Report-2013-003), Comments: See also <http://www.linearcollider.org/ILC/TDR> . The full list of signatories is inside the Report, Geneva: KEK, June 2013 (see pp. 52, 53).
- [26] Maxima, <http://maxima.sourceforge.net/> Link consulted 2013.02.19 (see p. 53).
- [27] Mathematica, <http://www.wolframalpha.com/> Link consulted 2013.02.19 (see p. 53).

- [28] R. Tomás. Overview of the compact linear collider, *Phys. rev. st accel. beams*, 13:014801, 1, January 2010, DOI: [10.1103/PhysRevSTAB.13.014801](https://doi.org/10.1103/PhysRevSTAB.13.014801) (see p. 53).
- [29] Daniel Schulte. Beam-Beam Simulations with GUINEA-PIG, March 1999 (see p. 57).
- [30] K. Kubo et al. Extremely low vertical emittance beam in accelerator test facility at KEK, *Phys.rev.lett.*, 88:194801, 2002, DOI: [10.1103/PhysRevLett.88.194801](https://doi.org/10.1103/PhysRevLett.88.194801) (see p. 61).
- [31] Y. Honda, K. Kubo, S. Anderson, S. Araki, K. Bane, A. Brachmann, J. Frisch, M. Fukuda, K. Hasegawa, H. Hayano, L. Hendrickson, Y. Higashi, T. Higo, K. Hirano, T. Hirose, K. Iida, T. Imai, Y. Inoue, P. Karataev, M. Kuriki, R. Kuroda, S. Kuroda, X. Luo, D. McCormick, M. Matsuda, T. Muto, K. Nakajima, Takashi Naito, J. Nelson, M. Nomura, A. Ohashi, T. Omori, T. Okugi, M. Ross, H. Sakai, I. Sakai, N. Sasao, S. Smith, Toshikazu Suzuki, M. Takano, T. Taniguchi, N. Terunuma, J. Turner, N. Toge, J. Urakawa, V. Vogel, M. Woodley, A. Wolski, I. Yamazaki, Yoshio Yamazaki, G. Yocky, A. Young, and F. Zimmermann. Achievement of ultralow emittance beam in the accelerator test facility damping ring, *Phys. rev. lett.*, 92:054802, 5, February 2004, DOI: [10.1103/PhysRevLett.92.054802](https://doi.org/10.1103/PhysRevLett.92.054802) (see p. 61).
- [32] M. Berndt, V. Bressler, K. Brown, F. Bulos, K. Bunnel, et al. Final focus test beam: Project design report, 1991 (see p. 61).
- [33] S. Araki et al. Proposal of the Next Incarnation of Accelerator Test Facility at KEK for the International Linear Collider, 2005 (see p. 61).
- [34] ATF2 Collaboration. ATF2 Proposal, SLAC, SLAC-R-771, 2005 (see pp. 61, 62, 67).
- [35] B.I. Grishanov et al. ATF2 Proposal. Vol. 2, technical report, ATF2 Group, 2006, pages 1–43 (see p. 61).
- [36] Maria del Carmen Alabau Pons. Optics studies and performance optimization for a future linear collider: final focus system for the e-e- option (ilc) and damping ring extraction line (atf), PHD Thesis, Departamento de Fisica Atomica, Molecular I Nuclear, Universitat de Valencia, 2010 (see p. 62).
- [37] Yves Renier. Implementation and validation of the linear collider final focus prototype : ATF2 at KEK (Japan), PhD thesis, Universite Paris XI Orsay, 2010 (see pp. 62, 64, 66).
- [38] M D Woodley and P E Emma. Measurement and Correction of Cross-Plane Coupling in Transport Lines, (physics/0008194. SLAC-PUB-8581):3 p, August 2000 (see p. 64).
- [39] T. Okugi, S. Araki, P. Bambade, K. Kubo, S. Kurado, M. Masuzawa, E. Marin, T. Naito, T. Tauchi, N. Terunuma, R. Tomas, J. Urakawa, G. White, and M. Woodley. Linear and second order optics corrections for the kek accelerator test facility final focus beam line, *Phys. rev. st accel. beams*, 17:023501, 2, February 2014, DOI: [10.1103/PhysRevSTAB.17.023501](https://doi.org/10.1103/PhysRevSTAB.17.023501) (see p. 65).
- [40] PATECKI, M. and others. Ultra-low beta study, CLIC Workshop 2015, 1 2015 (see p. 65).
- [41] Tsumoru Shintake. Proposal of a nanometer beam size monitor for e+e- linear colliders, *Nuclear Instruments and Methods in Physics Research Section A: Accelerators, Spectrometers, Detectors and Associated Equipment*, 311(3):453–464, 1992, DOI: [http://dx.doi.org/10.1016/0168-9002\(92\)90641-G](http://dx.doi.org/10.1016/0168-9002(92)90641-G) (see p. 66).
- [42] T. Shintake et al. Experiments of nanometer spot size monitor at FFTB using laser interferometry, Contributed paper at 1995 Particle Accelerator Conference and International Conference on High-Energy Accelerators, May 1 - 5, 1995, Dallas, Texas, U.S.A. (see p. 67).
- [43] J. Yan. Precise measurement of nanometer scale electron beam size using laser interference by shintake monitor, Ph.D. Thesis, Komamiya Laboratory, Graduate School of Science, The University of Tokyo, 2014 (see p. 67).

- [44] H. Hayano. Wire scanners for small emittance beam measurement in ATF, 2000, arXiv: [physics/0008084](#) (see p. 67).
- [45] PATECKI, M. and others. ATF2 December run ground motion study, CLIC Workshop 2015, 1 2015 (see p. 67).
- [46] *TOWARDS INTERNATIONAL LINEAR COLLIDER: EXPERIMENTS AT ATF2*, Proceedings of IPAC2014, 2014 (see p. 68).
- [47] K. Kubo. ATF2 progress report, CLIC Workshop 2015, January 2015 (see p. 68).
- [48] P. Bambade, R. Erickson, Wayne A. Koska, W. Kozanecki, N. Phinney, et al. Observation of Beam-beam Deflections at the Interaction Point of the SLAC Linear Collider, *Phys.rev.lett.*, 62:2949, 1989, DOI: [10.1103/PhysRevLett.62.2949](#) (see p. 68).
- [49] *IN VACUUM HIGH ACCURACY MECHANICAL POSITIONING SYSTEM OF NANO RESOLUTION BEAM POSITION MONITOR AT THE INTERACTION POINT OF ATF2*, Proceedings of IPAC2013, 2013 (see pp. 71, 110).
- [50] T. Nakamura. Development of beam-position monitors with high position resolution, Master Thesis, Department of Physics, Graduate School of Science, The University of Tokyo, 2008 (see pp. 72, 74, 75).
- [51] Y. I. Kim, R. Ainsworth, A. Aryshev, S. T. Boogert, G. Boorman, J. Frisch, A. Heo, Y. Honda, W. H. Hwang, J. Y. Huang, E-S. Kim, S. H. Kim, A. Lyapin, T. Naito, J. May, D. McCormick, R. E. Mellor, S. Molloy, J. Nelson, S. J. Park, Y. J. Park, M. Ross, S. Shin, C. Swinson, T. Smith, N. Terunuma, T. Tauchi, J. Urakawa, and G. R. White. Cavity beam position monitor system for the accelerator test facility 2, *Phys. rev. st accel. beams*, 15:042801, 4, April 2012, DOI: [10.1103/PhysRevSTAB.15.042801](#) (see p. 72).
- [52] T. Shintake and and. Development Of Nanometer Resolution Rf-Bpms:341–345, 1998 (see p. 74).
- [53] N. Blaskovic. Position to angle sensitivity, ATF IP BPM Meeting, January 2015 (see p. 79).
- [54] Yoichi Inoue, Hitoshi Hayano, Yosuke Honda, Toshikazu Takatomi, Toshiaki Tauchi, Junji Urakawa, Sachio Komamiya, Tomoya Nakamura, Tomoyuki Sanuki, Eun-San Kim, Seung-Hwan Shin, and Vladimir Vogel. Development of a high-resolution cavity-beam position monitor, *Phys. rev. st accel. beams*, 11:062801, 6, June 2008, DOI: [10.1103/PhysRevSTAB.11.062801](#) (see p. 90).
- [55] T. Nakamura. Development of beam-position monitors with high position resolution, Master's thesis, Tokyo, Japan: Departement of Physics, Graduate School of Science, The University of Tokyo, 2008 (see p. 91).
- [56] P. Burrows and FONT. Bunch-bunch feedback and IP beam stabilization, 18th ATF2 Project Meeting, February 2015 (see p. 93).
- [57] Ca lab (labview + epics), http://www-csr.bessy.de/control/SoftDist/CA_Lab. Link consulted 2014.11.06. (see p. 106).
- [58] *The High Position Resolution Cavity BPMs Developments and Measurements for ILC Final Focus System*, Proceedings of IPAC2014, 2014 (see p. 110).